Doctoral Dissertation

Quick and Mild Isolation of Intact Lysosomes using Magnetic-Plasmonic Hybrid Nanoparticles

The Son Le

Supervisor: Shinya Maenosono

Graduate School of Advanced Science and Technology
Japan Advanced Institute of Science and Technology
Materials Science

September 2022

Abstract

Since their discovery by Christian de Duve in the 1950s, the role of lysosomes in cellular function has been explored extensively, which led to the change of the view of lysosomes from a static digestive system to the dynamic regulator of cellular metabolism. As indicated in various studies, lysosomal dysfunctions are found to be linked with the group of metabolic disorders known as lysosomal storage diseases. Therefore, understanding lysosomal biology in both normal and pathogenic conditions is crucial to figuring out the mechanistic insights of lysosomal activity, to facilitate diagnostic methods or establish a new therapeutic strategy.

The rapid and efficient isolation of lysosomes is a prerequisite to identify lysosomal protein composition, using proteomic analysis to reveal their involvement in cellular functions or disease progression. So far, several strategies have been developed to isolate lysosomes, including density-gradient centrifugation, immunoaffinity purification, and magnetic nanoparticle-based fractionation. Among these approaches, a nanoparticle-based method that delivers magnetic nanoparticles to the lumen of lysosomes, through an endocytic pathway, followed by a separation process, using a magnetic column, has been proven to be able to isolate lysosomes with the highest yield and purity, while efficiently preserving their integrity. The traditional magnetic probes, such as superparamagnetic iron oxide nanoparticles (SPIONs), require surface modification by fluorescent dyes to enable the investigation of their intracellular trafficking, which has some disadvantages, including the possible alternation of their bio-interaction, and the instability of fluorescence properties in the lysosomal environment.

In this thesis, we have focused on developing a multifunctional magnetic probe with intrinsic imaging capabilities for tracking the intracellular transport of nanoparticles to lysosomes through endocytic pathways before performing magnetic separation. Notably, the kinetic transport is an important parameter that strongly affect the yield and purity of isolated fraction. In addition, we established the protocol to isolation of lysosomes as intact as possible.

Firstly, the magnetic-plasmonic AgFeCoAg nanoparticles (MPNPs) were prepared using polyol method. The obtained MPNPs was then undergone the encapsulation in phospholipid micelles, followed by the conjugation of amino dextran (aDxt) for targeting lysosomes. The hydrodynamic size of particles after encapsulation and conjugation process are 33.9 ± 2.6 nm and 52.4 ± 7.8 nm, respectively. The zeta potential was positive charge after conjugating aDxt. We observed that the dispersion of aDxt-MPNPs in culture medium, DMEM (+10% FBS), would suppress the cytotoxicity of nanoparticles, cell viability was above 70% even after 24 h incubation with nanoparticle concentration, CNPS = 100 μg/mL. Furthermore, the aDxt-MPNPs was also highly stable in culture medium which was very important to maintain the particle uptake. The number of aDxt-MPNPs internalized was almost double when extending the loading time from 1 h to 8 h.

Next, the intracellular trafficking of aDxt-MPNPs to a cell model (COS-1 cells) was investigated using the pulse-chase experiment and colocalization analysis. The colocalization between nanoparticle and organelles was determined by Manders' coefficient (R_t). As the result, the time-lapse colocalization of aDxt-MPNPs and early endosomes (EE), late endosomes (LE) and lysosomes (L) were constructed, which indicated that the aDxt-MPNPs arrived at lysosomes after a chasing period of 7 h. Furthermore, a simple mathematic model based on stretch exponential functions has been established to derive time constant that represented the speed with which nanoparticles were transported to EE, LE and L. Finally, TEM and EDS analysis of aDxt-MPNPs-treated COS-1 cells after 1 h loading and 7 h chase was performed to confirm the result of colocalization analysis.

Finally, after understanding the transport kinetics of aDxt-MPNPs to lysosomes in the cell model. Cells were completely homogenized using syringe with 23G needle after 15 passages, which was confirmed by the bright-field microscope. Subsequently, lysosomes were isolated using a magnetic column. The integrity was qualitatively screened by confocal laser scanning microscopy (CLSM), while the Western blot results confirmed the high purity of the isolated fraction. Additionally, it is concluded that to isolate lysosomes as intact as possible, the lysosomes should be isolated within 30 min after homogenization at 4^{o}C. Furthermore, our established protocol was demonstrated to be superior to the density gradient centrifugation method (DGC) in term of number of starting materials, isolation yield, purity, and time. Lysosomes were also isolated from HEK293 cells to confirm the versatility of the established methods.

Keywords: *magnetic isolation, lysosomes, intracellular trafficking, bioimaging, nanoparticles*

Table of Contents

Chapter 1: Introduction

1.1. Overview of lysosomes

1.1.1. Structure of lysosomes

Lysosomes are membrane-bound organelles that contain more than 60 hydrolytic enzymes and various lysosomal membrane proteins, which is firstly found by Christian de Duve in the 1960s. [1, 2] Regarding the activity of breaking down the specific biological substances such as proteins, lipids, and glycogens, the lysosomal degrative enzymes could be roughly classified into different groups such as proteases, nucleases, lipases, glycosidases, sulfatases, and phosphatases. The cargos degraded by lysosomes come from the various routes of delivery. For instance, the endocytic pathway targets small intracellular molecules from the endoplasmic reticulum and endocytosed membrane proteins. The autophagic pathway is involved to engulf waste materials in the cytoplasm including macromolecules and dysfunctional organelles. The phagocytic pathway is responsible for sensing and taking large foreign particles such as microorganisms and apoptotic cells. Due to the essential role in the degradation and recycling of waste materials, lysosomes have been considered as a static digestive system for a long time. However, the emerging studies have revealed that lysosomes are also the dynamic regulator of cellular metabolism (Figure 1.1),[3] which has a significant contribution to various cellular processes including nutrient sensing, membrane repair, immune signaling, organelle crosstalk, metabolic adaptation, and aging.[4]

Mature lysosomes have an acidic environment in their lumen (pH ~ 4.5 – 5), which is a prerequisite to activating the hydrolases for catabolic activities. The proton gradient is

steadily maintained by the vacuolar H^+-ATPase located on the boundary membrane.[5, 6]

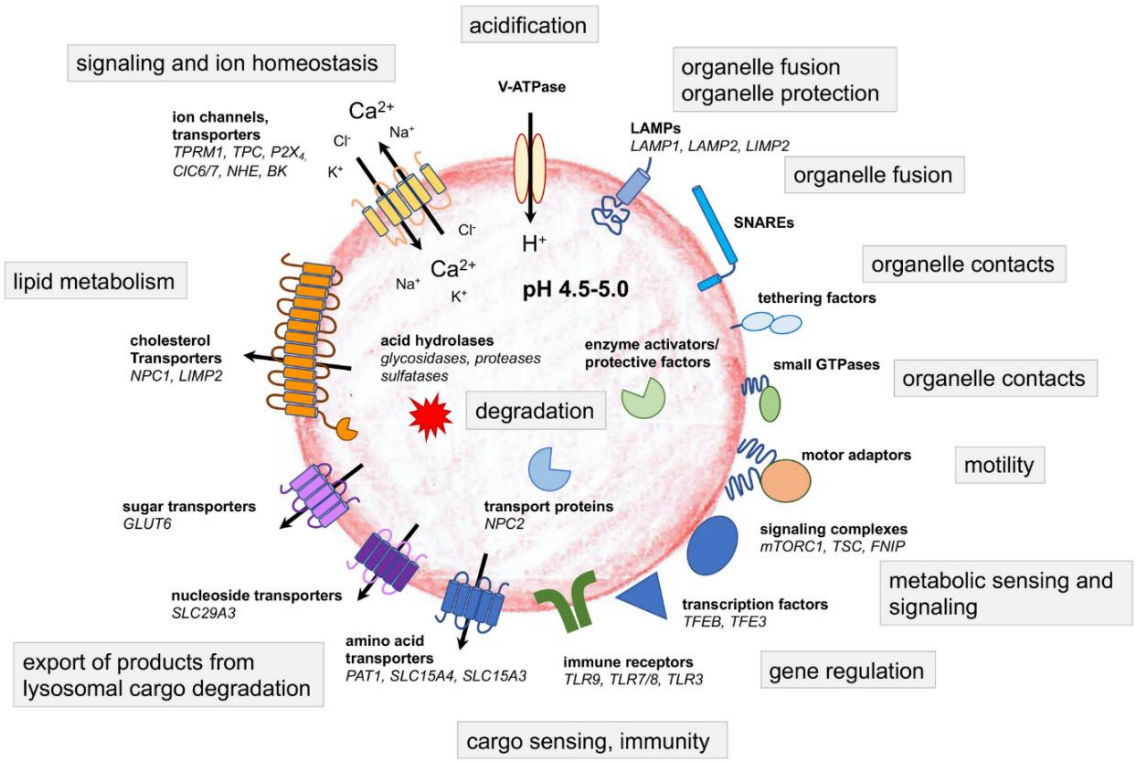

Figure 1.1: The structure and function of lysosomes are strongly correlated with their structural proteins. This figure highlights some lysosomal proteins and their central role in lysosomal function, biogenesis, and metabolism. Reprinted from ref. [7] under the term of the Creative Commons Attribution 4.0 International license. Copyright 2022.

Asides from the proton pump, the lysosomal membrane also has various ion channels and transporters to regulate the concentration gradient of Ca^{2+}, K^+, Na^+, and Cl^- across the membrane for controlling ion homeostasis.[8] Other key components of lysosomes are their structural proteins, especially those localized in lysosomal membranes. To segregate the lysosomal enzymes from other parts of cells, the lumens of lysosomes are encircled by Lysosomal Associated Membrane Protein 1 and 2 (LAMP1 and LAMP2). LAMP

proteins are also involved in the fusion of lysosomes with other organelles such as plasma membrane, late endosomes, and autophagosomes as well as the transport of ions, soluble proteins, and metabolites in and out lysosomes.[9] Along with LAMP proteins, the trafficking and fusion of lysosomes with other cellular compartments are mediated by tethering factors, soluble N-ethylmaleimide-sensitive factor attachment protein receptors (SNAREs) proteins, and membrane-associated Rab GTPases. Specifically, Ectopic P-granules autophagy protein 5 homolog (EGP5), a metazoan protein localized on late endosomes and lysosomes, is known as a tethering factor to enforce the fusion of lysosomes with autophagosomes or late endosomes.[10] On the other hand, SNAREs proteins play the role of molecular motors driving the fusion process. The SNARE deficiency causes the interruption of intracellular trafficking which results in various diseases, for example, in the absence of STX17 (a SNARE protein), the fusion between autophagosomes and late endosomes and/or lysosomes is inhibited.[11] Importantly, the action of SNAREs and EGP5 is regulated by Rab GTPases which is known as the coordinator of vesical traffic.[12] Particularly, the Rab protein family functions as central organizers to direct the intracellular vesicles trafficking to their target destination by recruiting effector molecules such as tethering factors, kinases, motors, and sorting adaptors through the conversion of two Rab GTPases conformation states including GTP- and GDP bound form.[12] In endolysosomal and autolysosomal pathways, Rab7 is implicated in the fusion of the late endosome, autophagosomes, and multivesicular body with lysosomes.[13]

1.1.2. Lysosome biogenesis

It was long presumed that the lysosomal biogenesis was constitutive. However, the recent discovery has indicated that cells continually monitor lysosomal function and regulate their activity in response to internal and external stimuli through the lysosome-nucleus signaling pathways. Particularly, the transcription factor EB (TFEB) was found to be a master gene for lysosomal biogenesis by promoting expression of various lysosomal proteins. Upon activation, TFEB translocate from cytoplasm to nuclei where they bind to Coordinated Lysosomal Expression and Regulation (CLEAR) via a 10-base pair (bp) palindromic motif, GTCACGTGAC.[14] The overexpression of TFEB in nuclei upregulates the transcription of lysosomal genes in CLEAR network, which leads to the increased number of lysosomes and elevated levels of lysosomal enzymes.[15] In addition, the autophagy activity is also increased as the consequence of TFEB overexpression. Interestingly, the activity of TFEB is directly regulated by mammalian target of rapamycin (mTOR) that is a key component to control cell proliferation, growth signals, and energy & nutrient sensing (Figure 1.2).

mTOR is a highly conserved serine/threonine kinase which exist in cells as two distinct complexes name mTOR complexes 1 (mTORC1) and complexes 2 (mTORC2). Two complexes have different contributions in cellular functions, in which mTORC1 regulates nutrient, energy, growth factors and stress response while mTORC2 regulates cytoskeletal structure, cellular metabolism and cellular insulin sensitivity.[16] A number of reports has revealed a tightly controlled interaction between mTORC1 activation and lysosomal activity.[17-19] Under amino acid deficiency, the v-ATPase-Ragulator complex does not activate Rag GTPases on the lysosomal surface, thus mTORC1 cannot be recruited to the

lysosome. Under the rich amino acid condition, mTORC1 is translocated from cytoplasm to lysosomal surfaces by Rag GTPases complexes in which Rag-A/B is GTP-loaded and Rag-C/D is GDP-loaded. After lysosomal attachment, mTORC1 is activated by interacting with lysosomal localized GTPases Rheb, a well-known mTORC1 activator (Figure 1.3). However, it should be emphasized that lysosomes do not simply act as platforms for mTORC1 regulatory pathway, there exist the closed interconnection between the activities of mTORC1 and lysosomes. In fact, the level of amino acids inside lysosomal lumen also directly modulates mTORC1 activity via V-APTases (Figure 1.3).[20]

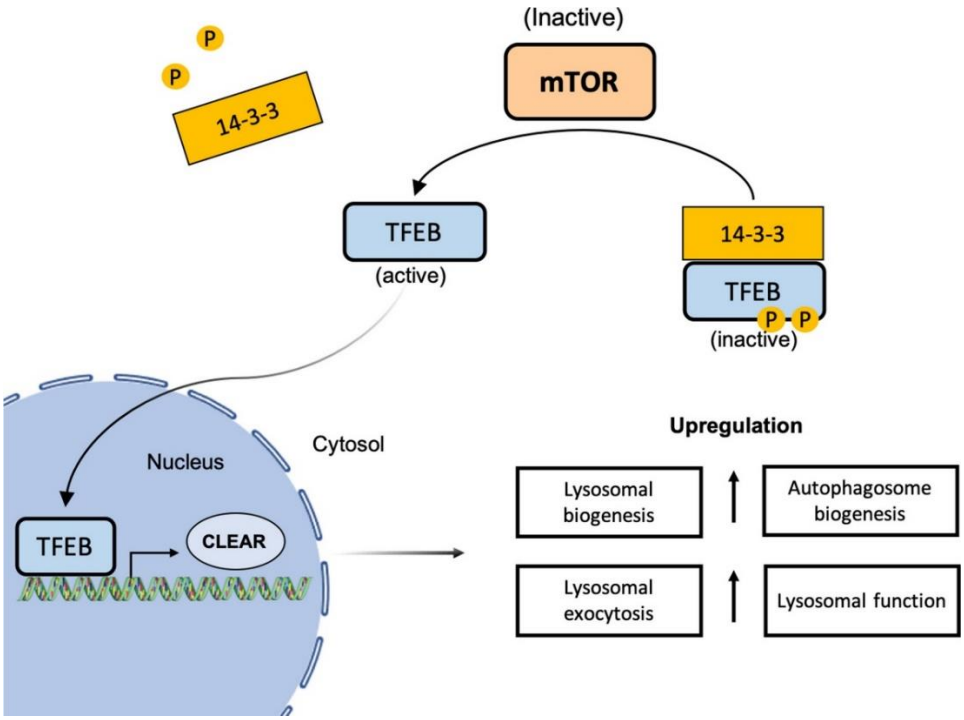

Figure 1.2: Schematic illustration of TFEB activation. At normal condition, TFEB is phosphorylated by mTORC1, which binds to 14-3-3 protein and retains in the cytoplasm. Upon stimuli, mTORC1 inhibition and the phosphatase calcineurin (not shown) are activated to induce dephosphorylation of TFEB, which results the translocation of TFEB to the nucleus and upregulation of CLEAR network genes. Reprinted from reference [21]. Copyright 2022, Wiley and Sons.

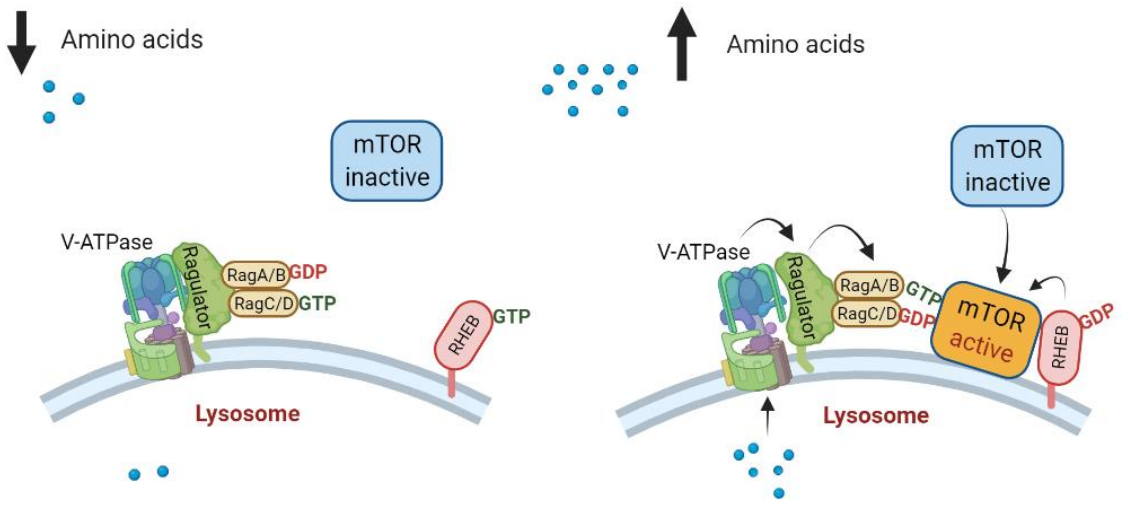

Figure 1.3: The schematic illustration of mTOR recruitment on lysosomal surface by Rag GTPases upon the amino acid conditions. (Created with biorender.com).

1.1.3. Lysosomal storage diseases

Lysosomal storage diseases (LSDs) are a set of metabolic diseases characterized by the deficiency of lysosomal enzymes, which leads to the built-up of undigested materials in lysosomes. The timeline of the evolving discoveries related LSDs is shown in Figure 1.4. The phenotype of LSDs was first described in 19th century, long before the discovery of lysosomes in 1955 by Christian de Duve.[22] After lysosomes are defined, a number of studies conducted between 1963 and 1970s found that the enzymatic deficiencies are responsible for the storage of undigested materials in lysosomes. [23, 24] For next two decades, the expansion of the knowledge on lysosomal biology and functions led to the identification of the molecular bases of LSDs and the mechanism involved in enzyme transportation to lysosome via mannose-6-phosphate pathway, which resulted the first attempt to replace defective enzyme in lysosomes in 1990. Until 2000s, the introduction

of novel technologies such as gene-modification and mass spectroscopy had the significant advancements on the study of LSDs, which provided the important tools to characterize the pathophysiology, identify lysosomal proteins and develop therapeutic strategies.

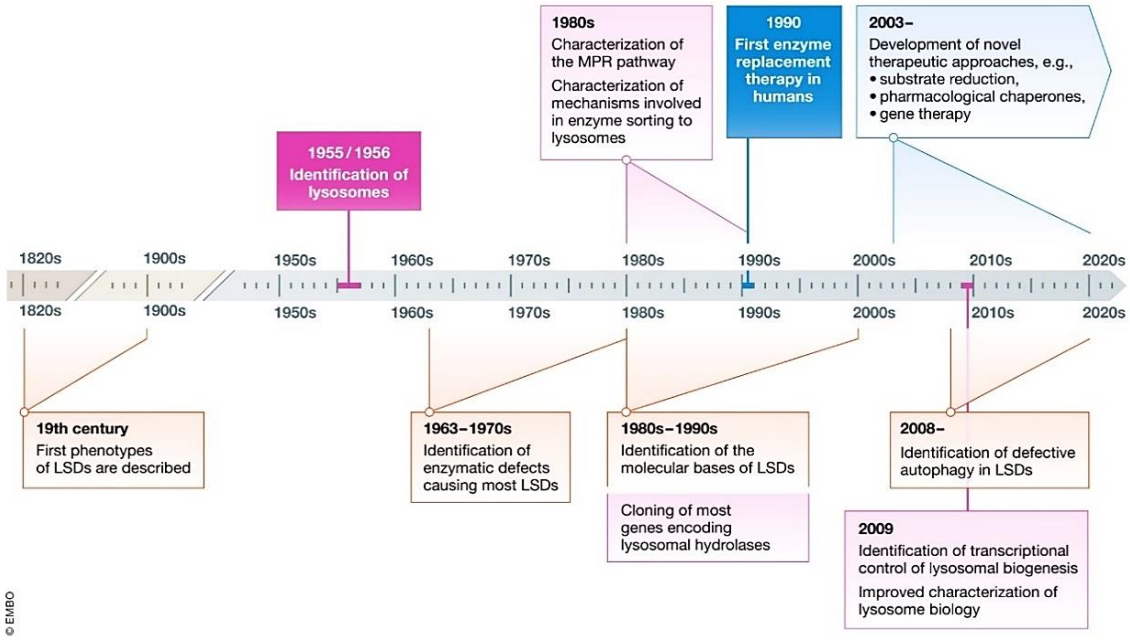

Figure 1.4: The timeline of major findings in LSDs. Reprinted under the term of the Creative Commons Attribution 4.0 International license. [26], copyright 2022, EMBO press.

For the long time, the LSDs are often regarded as the direct outcome of the accumulation of undigested materials in lysosomal lumen. However, the recent advancement in the knowledge of lysosomal functions and biogenesis has been speculated that the storage disorder is just an initiator for a number of secondary events and the buildup of undegraded substrates is capable of initiating complicated pathogenetic pathways that ultimately result in LSD symptoms.[25] Given the central role of lysosomes in

macromolecules catabolism and metabolic hubs, a number of events has been identified as the contributor to the pathophysiology of LSDs (Figure 1.5), which includes the impaired intracellular trafficking of vesicle and autophagic flux, perturbation of calcium hemostasis, mitochondrial dysfunction and increased oxidative stress.

To present, the identification that LSDs consists of 70 monogenic disorders which are linked to the mutation of genes encoding lysosomal proteins. Most of the mutations that cause LSDs have been elucidated, and many of them result in the deficiency of a specific lysosomal hydrolase, which causes the buildup of the non-degraded materials inside the lysosomes trigger the pathogenetic cascade. For instance, in Gaucher disease, the deficiency of β-Glucocerebrosidase (GCase) leads to the accumulation of the glycolipids lysosomes, which often results in the dysfunction of the liver and spleen.[26] From another perspective, the pathogenesis of the LSDs can also be characterized by the biochemical nature of the accumulated substrates. Thus, the storage of glycosaminoglycans in lysosomes underlines the severe skeletal abnormalities in the patient with Mucopolysaccharidosis type IV.[27] In the other example, the buildup of non-degraded glycogen in muscle cells could be explained for metabolic myopathy in patients with Pompe disease, since the glycogen is known as the fuel sources for muscles cells. However, it should be emphasized that there also remains LSDs with unknown mechanism of the accumulation of biomolecules and their connection with the observed pathology. In summary, due to the heterogeneity, complexity and the involvement of other organelles in the pathogenesis, LSDs could be roughly classified as (1) the types of accumulated substrates, (2) distinct mutated-genes responsible for metabolism defects, (3) the types of membrane protein disorders and (4) lysosome-related organelle disorders.[28] Clinically, LSDs have a board range of phenotypes regarding the age of onset,

the severity of nervous/systemic involvements. The progress of disease is relentless over time, which severely impact on the prognosis and life quality of patients.

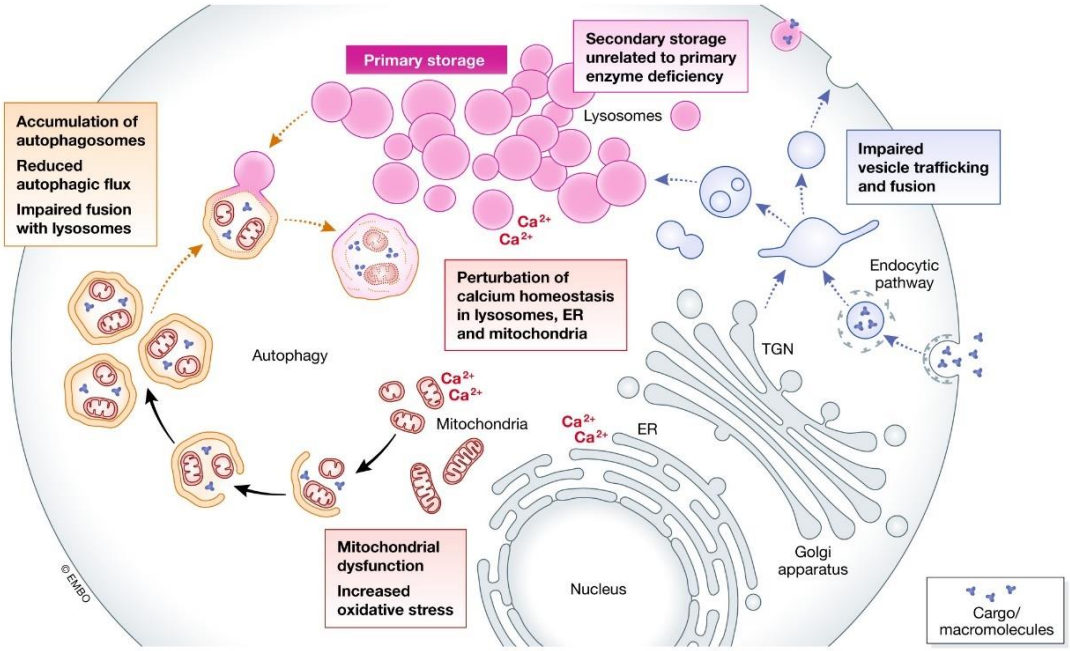

Figure 1.5: Summary of organelles, intracellular trafficking and metabolic pathways involved in LSDs. Reprinted from ref. [29] under the term of the Creative Commons Attribution 4.0 International license. Copyright 2022, EMBO press.

So far, the established therapeutic approaches for LSDs are still very limited, which are only available for a handful of LSDs with exclusive symptomatic such as Gaucher disease, Fabry diseases and Mucopolysaccharidosis type I.[30-32] However, the cost of treatment remain expensive. Additionally, the most treatment usually initiated at late stage when the organs are already malfunction. Therefore, the treatment is mainly to stabilize organ function and slow disease progression. To overcome those limitations, the mechanistic understanding of lysosomal functions and their connection with LSDs as well as finding LSDs markers are crucial to predict prognosis and develop new therapeutic interventions

1.2. Proteosome analysis of lysosomes

Proteomics is one branch of omics sciences studying proteins in various aspects such as structures, expression levels in different cellular contexts, functions, and their intra/extracellular interaction. The proteomic analysis of the lysosomes has been exploited as an important tool for the understanding of lysosomal function and their role in LSD pathophysiology. Over last 20 years, a number of studies has employed mass spectroscopy (MS) to characterize lysosomal proteome to identify novel lysosomal proteins, reveal lysosomal functions in cellular processes, identify the alternation of protein composition of lysosomes in pathogenic context and identify biomarkers for LSD diseases.

1.2.1. Identification of lysosome-related proteins

Identification of novel lysosomal protein is basically one of the priorities of the proteomics study. Generally, the lysosomal proteins could be categorized in 3 groups: (1) luminal hydrolases, (2) membrane proteins and (3) lysosomal membrane-associated proteins. According to an investigation conducted by Winter et al. in 2021, among 905 lysosomal proteins are assigned on gene ontology (GO) and UniProt database, there are 341 lysosomal proteins connected to the specific biological functions of lysosomes. To specify, more than 100 proteins are lysosomal membrane proteins that maintain the stability of lysosome and regulate the transport of small molecules and crosstalk with other cellular compartments. Some typical proteins in this group are LAMP protein family and v-ATPase for stabilizing lysosomal structure and homeostasis, ESCRT for lysosomal repair,[33] HOPS, CORVET and AP complexes for facilitating molecular transport to lysosome,[34] SNAREs for lysosomal fusion. In addition, about 70 luminal hydrolysates

are identified which responsible for various lysosomal catabolism processes. About 120 proteins are classified as lysosomal membrane-associated proteins (Figure 1.6).[35] The most well-known example of lysosomal membrane-associated proteins is mTORC1 whose play important role in nutrient sensing and cellular growth. To date, it should be emphasized that despite considerable progress, the list of novel lysosomal proteins has continuously grown, and the further studies are still required to identify the exact functions of many lysosomal proteins.

The current picture of the diversity of lysosomal proteins indicates that the functions of lysosomes are often governed by a set of proteins rather than a few selected candidates. Therefore, the characterization of lysosomal protein on a large-scale by MS-based proteomics would play the main role to further investigate the role of lysosomes in cellular function and pathological conditions.

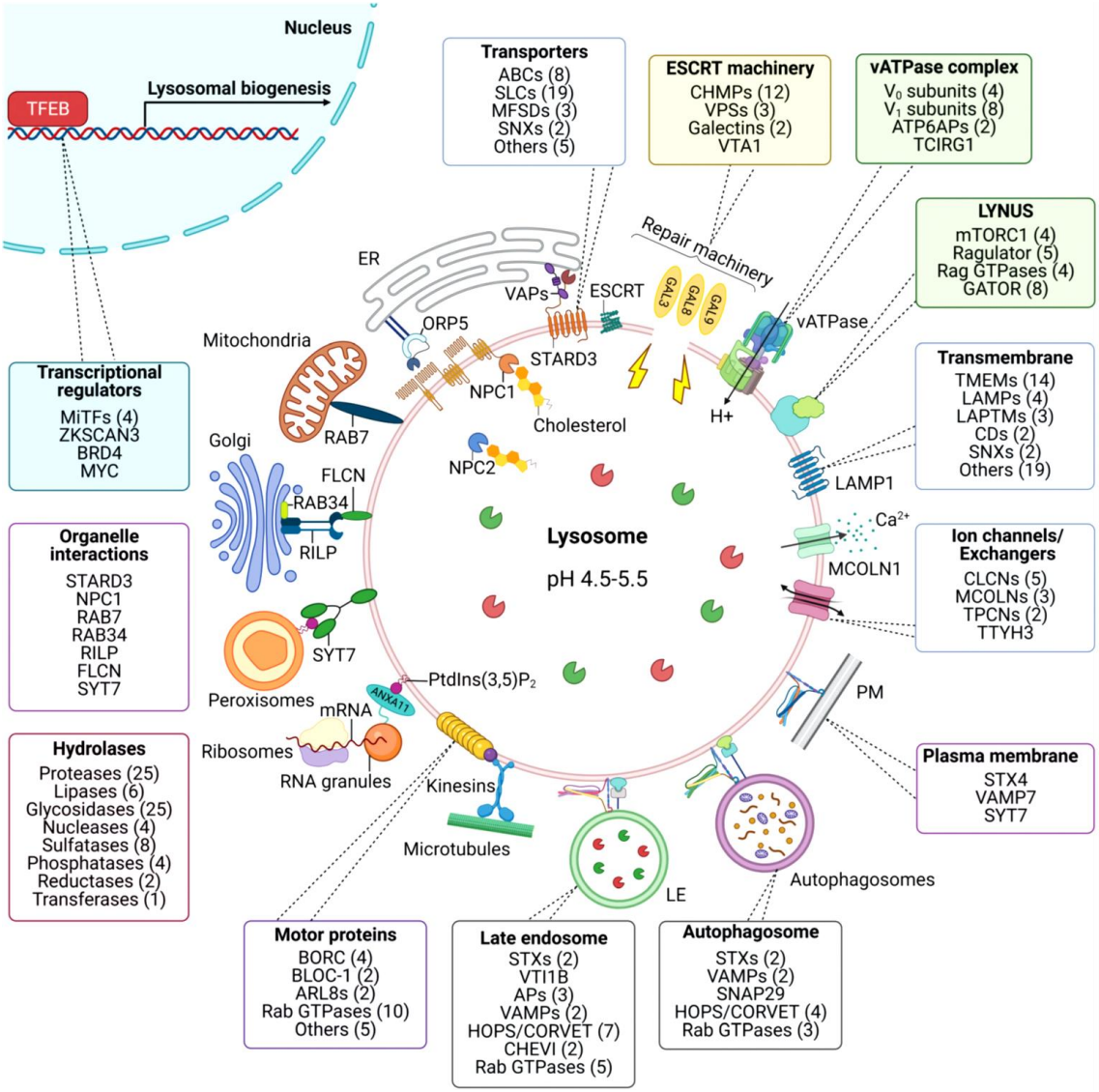

Figure 1.6: Current progress in the identification of functional proteins in lysosomes. ESCRT: endosomal sorting complex required for transport; HOPS: homotypic fusion and protein sorting; CORVET: class C core vacuole/endosome tethering; CHEVI: class C homologs in endosome–vesicle interaction; LYNUS: lysosomal nutrient sensing machinery; PM: plasma membrane; LE: late endosomes. Reproduced from Ref. [35] with permission from the Royal Society of Chemistry. Copyright 2022.

1.2.2. Investigation of lysosomal activity by proteome dynamics

Along with identification of novel lysosome-associated proteins, a number of studies employs proteomic analysis to reveal the alternation of protein composition under different stimuli for deriving the connection between the lysosomal activities and the specific proteins. Of note, in order to obtain the proteomic dataset for those purpose, the isolation of intact lysosomes is required, which will be discussed in detail in the later part of this thesis. Some typical projects in this research topic are the investigation of activity of lysosomes in controlling cellular metabolome. For instance, Sabatini's group and Michael Zhu's group developed immunoprecipitation method to enrich intact lysosomes and quantitatively analyzed the lysosomal metabolites under nutrient replete and starvation conditions to reveal the roles of V-ATPase and mTORC1 in regulation of the efflux of essential amino acids.[36, 37] Under simulated impairment of lysosomal function like mTORC1 inhibition, lysosomes acts as a storage compartment of these amino acids by decreasing their transport across the lysosomal membrane.

Lysosomal proteome dynamics could also be employed to exploit the cellular process involved lysosomes. For example, chaperone-mediated autophagy (CMA) facilitated by LAMP2 protein is a transport process of lysosomal substrate, whose malfunction often causes various diseases. The target selectivity for this transport pathway is regulated by the prevalence of a pentapeptide motif (KFERQ-like motif).[38] For investigation of the substrate specificity of CMA pathway, Merve et al. analyzed the lysosomal proteome of isolated lysosomes from SUM159 breast cancer cells to determine the dynamic change of temporal lysosomal proteome during glucose starvation in response to non-macroautophagy-activated conditions. The quantitative proteomic data provided a novel

correlation between lysosomal target selectivity by autophagic pathway and duration of stress condition. Specifically, amount of proteins with KFERQ-like motifs recruited to the lysosome increased significantly as the stress condition was prolonged.[39]

The mechanism of lysosomal protein transport has also been extensively studied using lysosomal proteomics. In eukaryotic cells, mannose 6-phosphate (M6P) pathway is responsible for sorting and transporting various hydrolase proteins produced from Golgi to lysosomes is also investigated. To examinate protein trafficking in M6P-pathway, Markmann et al. analyzed the lysosomal proteins contents from wild-type and M6P-deficient mouse fibroblasts using Stable Isotope Labeling by Amino acids in Cell culture (SILAC)-based quantitative mass spectrometry. The SILAC data indicated that the transportation of only 10 among 52 known hydrolase enzymes solely relied on the of M6P-pathway and incapable of using M6P-independent pathways. The expression of those proteins was declined from 20- to 40- fold. In addition, it was revealed that low-density lipoprotein (LDL) receptor, LRP1, contributes to the trafficking of non-phosphorylated lysosomal enzymes to lysosomes as an alternative targeting pathway.[40]

To sum up, the above examples show the important roles of proteomic analysis, especially the monitor of dynamic alternation of lysosomal protein expression in different contexts towards the elucidation of lysosomal activity.

1.2.3. Proteomics analysis of lysosomes in LSDs

Similar to the concept of investigating lysosomal functions, the pathogenic mechanism and progression of LSDs could be elucidated via determination of altered levels of lysosome-associated proteins using proteomic analysis. For example, to reveal the dysfunction of lysosomes caused by CLN6 deficiency, a neurodegenerative disease

happens in childhood belonged to neuronal ceroid lipofuscinoses collection as known as Batten diseases, Andreas et al. characterized the quantitative differences in protein compositions of lysosomes isolated from the liver of CLN6-defficiency and wild-type murine models.[41] Of note, although the CLN6 diseases has been identified long time ago, their connection with the lysosomal dysfunction remains unknown. The proteomics data indicated that the expression of three protases including cathepsin F, cathepsin D and Tripeptidyl peptidase I (Ppt 1) was significantly decreased in the lysosomes of CLN6-deficient mouse liver. Meanwhile levels of other hydrolases were unchanged. These results suggested the involvement of CLN6 in the transport of some selected enzymes to lysosomes. In addition, in other study, proteomic analyses indicated that the downregulation of CtsF, CtsD and Ppt1 was also observed in liver lysosomes of CLN8 deficient mice in comparison with that of the wild-type mice.[42] These observations implied the possible cooperation between CLN6 and CLN8, which later lead to an identification that CLN6 and CLN8 forms a complex called EGRESS (ER-to-Golgi relaying of enzymes of the lysosomal system) for trafficking newly synthesized lysosomal proteins from ER to Golgi.[43] In short, these findings had significant contribution to uncover the underlying mechanism of Batten diseases caused by CLN6 and CLN8 deficiency. Other type of Batten disease caused by mutation of CLN3 gene is also addressed by proteomics approach. Schmidtke et al. isolated lysosomes from cerebellar cells of CLN3-KO and wild-type mice using magnetic separation. By employing SILAC-based MS analysis, authors found that there was significant decrease in the levels of 28 soluble lysosomal hydrolases related to CLN3 deficiency, which accounted for the reduced degradation capability of various macromolecules and sphingolipids. In this study, the abnormal composition and distribution of membrane

lipids were also observed, which might the reason of the impairment of the transferrin transport along exocytic route.[44]

Other LSDs are also investigated using proteomics. For instance, Tharkeshwar et al. studied NPC1 using proteome analysis of NPC1-KO and wild-type HeLa cells. Along with the confirmation of the cholesterol and glycosphingolipids accumulation in lysosomes, a well-known characteristic of NPC1 disease, authors were able to identify the accumulation of other lipid species including ceramide, hexosylceramide and sphingomyelin and the alternation in levels of several proteins associated with lysosomal catabolism.[45] To investigate Chediak–Higashi syndrome characterized by the deficiency of Lysosomal Trafficking Regulator (LYST) proteins, Zhang et al. analyzed the alternation of protein composition in lysosomes isolated from Beige mice and normal mice. The proteomic data indicated the abnormal increase of ER proteins located in lysosomal membranes of Beige mice due to absence of LYST, which implied the role of LYST in protein transport during recycling/maturation of the lysosomal membrane.[46]

LSD diagnosis and monitoring have benefited greatly from advances in high-throughput metabolite analysis technology. Generally, diagnostic and therapeutic strategies in rare hereditary metabolic disordered are based on biomarker-driven approaches. Proteins are commonly used biomarkers. It should be noted that the development of diagnostics and treatment methods of many LSDs are still hampered by the lack of the availability of these disease indicators. The modern analytical techniques such as mass spectroscopy and nuclear magnetic resonance has significant contributions in finding biological markers of LSDs, in which mass spectroscopy is regarded as the most extensively used platform for diagnosing genetic metabolic disorders, owing to its ability to detect a wide range of

biomolecules with very high sensitivity.[47] In recent years, the identification of lysosomal proteosome under pathogenic conditions has been exploited extensively, which could shed insights into the activity of lysosomes in pathogenic states to identify the biomarkers or molecular bases of LSDs.[48-50] For example, to identify protein markers of Niemann Pick Disease Type C (NPC), a lethal neurogenerative disorder characterized by the lysosomal cholesterol accumulation, Cologna et al. performed quantitative proteomics to determine a set of proteins that had altered levels related to pathological processes of NPC1 in murine models compared to controls.[48] Since biomarkers could be either specific or non-specific to NPC1, their altered expressions were further investigated to identify their contribution to the specific biological pathways of neurodegeneration in NPC1 patients. The non-specific biomarkers that were determined by proteomic data were KEGG proteins involved in glucose metabolism, detoxification enzymes glutathione-s transferase A4 and P1 associated with oxidative stress, and Alzheimer disease-related proteins. Importantly, the elevated protein expression of fatty acid binding protein family members including FABP3, FABP5 and FABP7 in mouse models was also determined. By translating the results from mice models to patients, it was confirmed that altered level of FABP3 could be the specific biomarker reflecting the progression of neuronal loss/damage. This biomarker could potentially assist the development of therapeutic treatment for NPC1 diseases.

1.3. Enrichment of intact lysosomes

In large-scale proteomics studies, the reproducibility of protein quantifications/identifications of whole cells by MS analysis is often challenging as the

lysosomal proteins are typically low abundance while highly dynamic. A series of studies conducted by Borner et al. indicated that lysosomes in Hela cells and mouse primary neurons only contribute >1% of cell protein mass. [51, 52] This result is consistent with the fact that the number of lysosomes in a given cells only ranging from 90 to 190.[53] Therefore, accompanying with lysosomal proteosome, the enrichment step is a prerequisite to reduce the sample complexity, which would increase the low-abundant lysosomal proteins for subsequent analyses. To date, the are number of techniques have been established to enrich intact lysosomes, which could be classified as density-gradient centrifugation, affinity chromatography and SPIONs-based magnetic isolation. Although the basis of those approaches is different, all require the disruption of cell membrane by any means such as dounce homogenizer, syringes, and bead mills, then perform isolation of lysosomes from cell lysate. To assess the purity of isolated fraction, the marker proteins for lysosome and other organelles could be monitored using Western blot.

1.3.1. Lysosome isolation by density-gradient centrifugation

The most traditional technique for lysosome isolation is density gradient centrifugation that is also the method used by Christian de Duve to firstly discover lysosome in 1950s.[2] The principle of this technique relies on the difference in the density of organelles, which can apply for fractionation of various organelles, not limiting to only lysosomes. Regardless of the isolation yield and purity, centrifugation-based technique could be easily adapted with any cells or tissues to extract lysosomes. Basically, this technique has 2 major steps. Firstly, cells or tissues are collected and homogenized. Following this, a low-speed centrifugation is performed to separate the organelles from unbroken cells, nucleus, and debris and the obtained post-nuclear supernatants are then subjected to

gradient centrifugation to further fractionation (Figure 1.7). Isopycnic centrifugation is commonly used to isolate lysosomes, which is based on the time-independent sediment of lysosomes as they reach their isopycnic point during centrifugation in the density gradient. The most well-known gradient matrix for density-gradient centrifugation is sucrose. Although lysosomes are significantly enriched, the isolated fraction are still contaminated by other organelles like mitochondria and endosomes. To overcome this limitation, over the years, other types of discontinuous and continuous gradient mediums have been developed such as Percoll,[54] Nycodenz,[55] Histodenz[56] and Metrizamide[57] to enhance the resolving power of centrifugation-based technique. Nevertheless, despite of many efforts, the contamination from other organelles remains unavoidable since many of them have nearly identical sizes and densities with lysosomes.

To get rid of the overlap of densities of lysosomes with other compartments, other strategies are proposed to alter the lysosomal density. Since the lysosomes are the endpoint of the endocytic pathways, the colloidal gold nanoparticles were delivered to their lumen, followed by density-gradient centrifugation. As a results, the highly pure fraction of lysosomes could be isolated. However, many lysosomal structures were broken during high-speed centrifugation,[58] which could obviously have adverse effects on the result of the subsequent downstream analysis.

Asides from the poor resolving power, other disadvantage of density-gradient centrifugation is the requirement of the high amount of starting materials due to the typically low isolation yield, which could be the limitation for some certain applications like studying lysosome functions in different stimuli conditions. Additionally, the lengthy centrifugation step required arises the concern about the loss of labile molecules during

isolation process. Therefore, developing alternative approach for lysosome isolation is necessary to facilitate the enrichment of intact lysosomes with high purity.

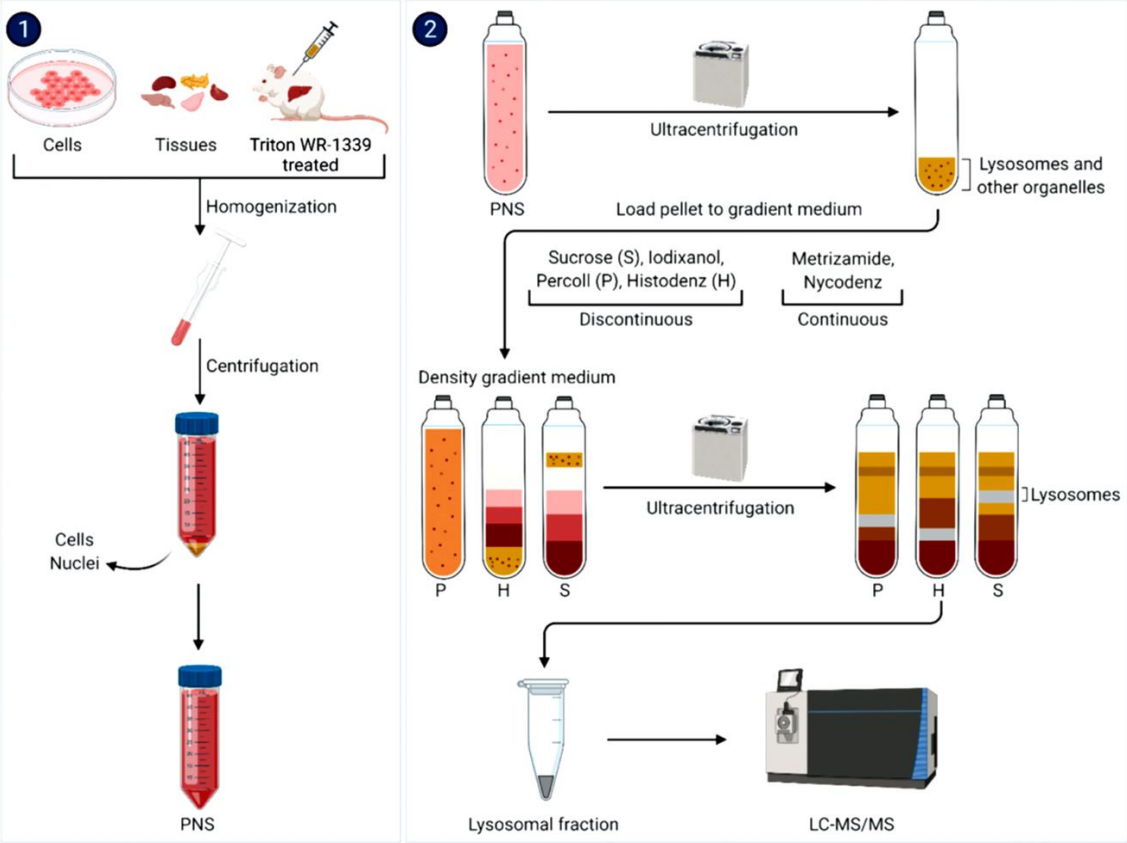

Figure 1.7: The illustration of the procedure of lysosome isolation using density gradient centrifugation. Reproduced from Ref. [35] with permission from the Royal Society of Chemistry. Copyright 2022.

1.3.2. Lysosome isolation by immunoprecipitation

Recently, to isolate lysosomes with highly purity, the immunoprecipitation approach utilizing the specific and selectivity interaction of antibodies to bind the antigens presenting on lysosomal surface has been introduced. Because of the limited number of lysosomal membrane proteins with cytosolic-facing epitopes, this technique required transfection of lentiviral vectors with tagged molecules or twin-step tags to modify

overexpressed lysosomal transmembrane proteins before performing affinity purification (Figure 1.8). For instance, lysosome-associated membrane proteins LAMP1 were fused with mRFP-2x FLAG or 3x FLAG. Following this, the lysosomes were isolated by anti-FLAG affinity gel or magnetic Dynabeads conjugated with anti-FLAG, respectively. [20, 59] With the same principle, lysosomal transmembrane protein 192 (TMEM192) were tagged with three tandem HA epitopes, then used anti-HA magnetic beads to capture lysosomes.[36] Furthermore, other work demonstrated that the immunoprecipitation could also isolate lysosomes specifically by using magnetic beads conjugated with antibody against the cytosolic A and B subunits of the V1 domain of the v-ATPase (Figure 1.8).[60] In these approaches, to maintain the proper capture efficiency, a sustainable amount of antibody is required. The cost and isolation yield are trade-off. As an alternative for antigen-antibody interaction, other study fuses the cytoplasmic tails of lysosomal membrane proteins to the Strep II tag, following by the capture of lysosomes by streptavidin beads. The advantages of this method is cost-effectiveness and the streptavidin is known to be more stable than antibodies.[61]

Overall, the isolation of lysosome using affinity purification is fast and specific. The isolated lysosomal fraction has a high purity in comparison with the traditional centrifugation-based approach. However, the cell modifications are required to insert tagged molecules on lysosomal membranes to be captured by antibody or streptavidin conjugated beads. In addition, it is impossible to release lysosomes on the captured beads after recovery. According to a recent study conducted Winter et al., the modification of the lysosomal membrane for affinity purification could affect the protein composition and the subsequent proteomics analysis. Specifically, the isolation of lysosomes using

immunoprecipitation was found to result in loss of some lysosomal membrane proteins, luminal hydrolases, and lysosomal-associated proteins.[62]

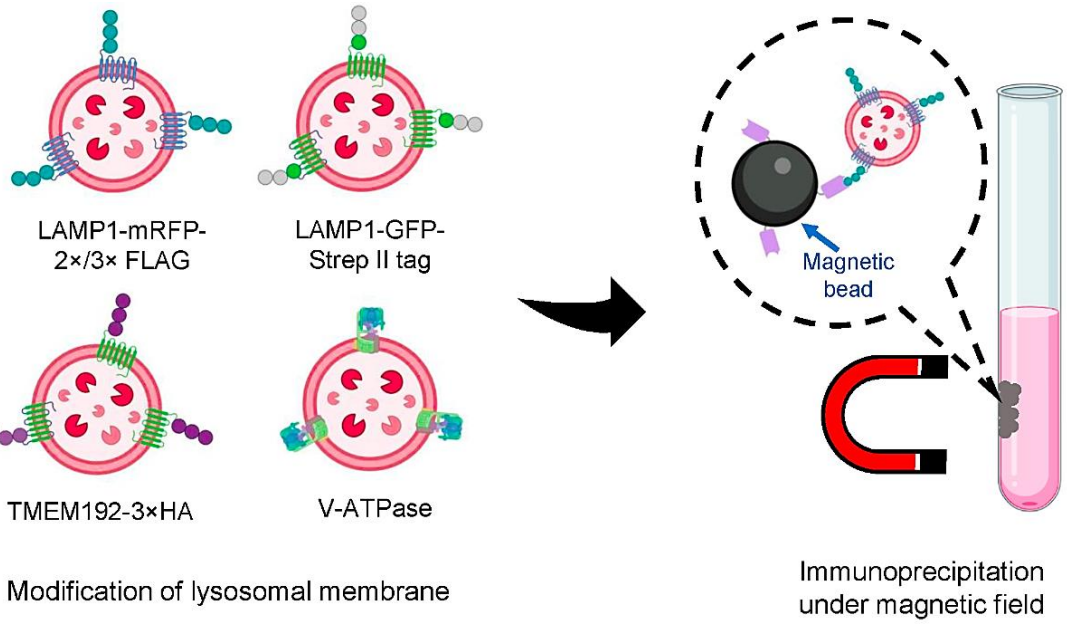

Figure 1.8: Illustration of the enrichment of lysosomes by immunoprecipitation, lysosomal membrane proteins could be tagged with FLAG, HA, and Strep molecules. Following cell homogenization, intact lysosomes are affinity enriched by immobilized antibodies or streptavidin targeting FLAG, HA, Strep. In addition, different subunits of the v-ATPase could be targeted directly to enrich lysosomes by their immobilized antibody. (Created with biorender.com)

1.3.3. Lysosome isolation by superparamagnetic iron oxides nanoparticles

In order to isolate lysosomes using an external magnetic field without relying on antigen-antibody interaction for capturing lysosomes as shown in immunoprecipitation technique, the intravascular magnetization of lysosomes is a feasible option since lysosomes are known as the endpoint of endocytic pathway. The first novel approach proposed in 1998 by Winchester et al. used superparamagnetic iron oxide nanoparticles coated with dextran

(FeDex) to isolate lysosomes from fibroblasts. Specifically, FeDex particles are incubated with cultured fibroblasts for a pulse uptake, following a chase period in fresh culture medium to load FeDex to lysosomes through endocytic pathway. After chasing step, cells were homogenized, and the cell lysate was subjected to Miltenyi MiniMACS column attached to a magnet (Figure 1.9). Under this condition, the magnetized lysosomes are immobilized inside column while all non-magnetic materials passed through. Finally, the column was then removed from the magnet, the lysosomes were twice eluted using non-ionic detergent-containing buffer solutions. The first elution was to remove soluble luminal proteins, while the second elution was to obtain lysosomal membrane protein fraction .[63] This pioneering work of Winchester group inspired the development of different versions of this technique later on. In 2005, Ioannou et al. adapted this approach for *in vivo* use to separate lysosomes from livers of mice model carrying Niemann–Pick type C 1 disease. The FeDex nanoparticles were administrated to mice, following by the incubation in different time range. Mice was then sacrificed for harvesting livers. Subsequently, the magnetic isolation processes were performed as described in Winchester work. A modification that was made in this work was the absence of detergent in eluted buffer. Although the isolation yield was low, but the structure of lysosomes was intact.[64]

To present, this approach is often used to obtain intact and functional lysosomes from cultured cells for studying lysosomal functions using mass spectroscopy. The versatility of SPIONs together with the quick and gentle nature of magnetic isolation are advantages of this technique. To target lysosomes, the surface of SPIONs could be coated by different molecules. Asides from dextran, the most well-known one, the use of other molecules such as 2,3-dimercaptosuccinic acid and amino lipids are recently demonstrated. It should

be noted that the surface property would have significant impact on biocompatibility and uptake efficiency of particles by cells. Furthermore, colloidal stability of magnetic nanoparticles in biological medium is also a parameter should be considered, the aggregation would have negative affect to cellular uptake. Additionally, after being delivered to lysosomes, nanoparticles should be remained in fluid-phase in lysosomal lumens, otherwise, lysosomal membranes could be damaged if nanoparticles were solidified.[65]

Of note, compared with conventional centrifugation- or immunoaffinity-based methods, this technique can isolate lysosomes in a short time after the cell homogenization, and neither antibody modification of the magnetic beads nor lysosomal transmembrane modification is required. Additionally, a recent study also indicated that the isolation of lysosomes using magnetic nanoparticle results the highest purity and yield per starting materials while efficiently preserve intactness of lysosomes.[62] To expand the application range of this technique to various cell lines, determining the appropriate timing for separation is crucial to obtain lysosomal fractions with high yield and purity, since the kinetics of intracellular transport are governed by many factors such as cell types, loading conditions, and incubation time.

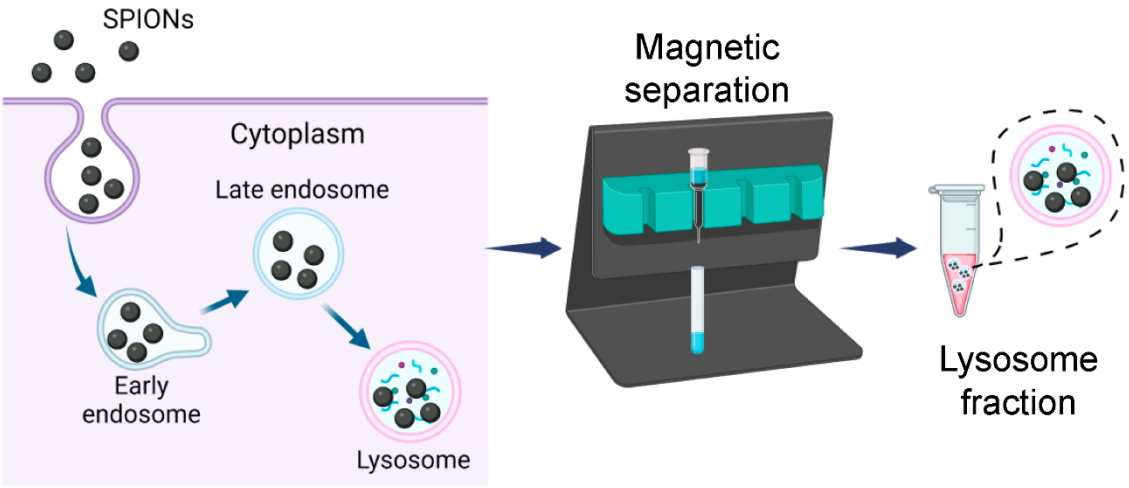

Figure 1.9: Schematic illustration of the enrichment of lysosomes using SPIONs. SPIONs are endocytosed and delivered to lysosomes via the endocytic pathway. The Miltenyi MiniMACS column attached to a strong magnet allows isolating magnetized lysosomes from non-magnetic materials. The column was then detached from the magnet, following by the elution of lysosome fraction. (Created with biorender.com)

1.4. Research objectives

Recently, the proteome analysis of lysosomes has been demonstrated as a powerful tool to not only explore the labile metabolites of lysosomes but also reveal the origin of lysosomal storage disorder to develop new therapeutic interventions. To achieve these purposes, the rapid isolation of an intact lysosomal fraction with high purity is crucial.[66] As discussed in introduction section, intravascular magnetization has received the great interest to isolate lysosome using magnetic separation, which currently possess the leading performance in term of yield, purity and integrity of isolated fraction.

In many studies, to ensure that a sufficient amount of SPIONs accumulated in lysosomes for magnetic isolation, lengthy incubation (>24 h) is often required,[44, 67] and the long-term accumulation of nanoparticles in lysosomes may affect lysosomal activity.[68, 69] Furthermore, most lysosomal disease cells are known to have an abnormal endocytic

pathway and exhibit defective cellular uptakes, which may cause retardation in trafficking.[70, 71] Therefore, understanding the intracellular trafficking of SPIONs before performing magnetic separation is crucial to quickly obtain highly purified isolation fractions.

Imaging methods such as electron and fluorescent microscopy are indispensable for determining the spatial distribution of SPIONs in cells. However, aside from laborious sample preparation, electron microscopy is time-consuming, and the field of view is narrow, which means it is not well suited as a confirmation technique for trial-and-error experimentation. Fluorescent microscopy with facile sample preparation can promptly screen a large number of cells under different conditions. Although fluorescent microscopy is a facile and convenient technique, in addition to the photobleaching problem, it was recently found that dye-labeling of nanoparticles, including SPIONs, could have dye-leaking and/or could influence their uptake and intracellular trafficking.[72-74] Therefore, to further refine a SPION-based isolation technique, it is necessary to design new types of magnetic probes with intrinsic imaging capability to precisely visualize the intracellular transport process of probes and quickly obtain highly-purified lysosomal fractions.

Regarding above-mentioned problems, this thesis highlights following topics and their details:

Preparation of multifunctional magnetic plasmonic AgFeCoAg nanoparticles with intrinsic imaging capability for tracking the intracellular transport and magnetic property for separation of lysosome using magnetic column. Modification of the surface of MPNPs

for targeting lysosomes via endocytic pathway.

Investigation of the kinetics of the intracellular trafficking of MPNPs in COS-1 cell model using pulse-chase experiments and colocalization analysis, in which the MPNPs are detected by plasmonic scattering signals.

Magnetic isolation of lysosomes using magnetic column. Investigation of effect of temperature and elapsed time from homogenization to completed enrichment of lysosomes on protein composition of isolated lysosome fraction.

The chapter 1 presents the general introduction of lysosomes and their importance in cellular process. In addition, the role of lysosomes in lysosomal storage disorders is also introduced. The proteome analysis of lysosomes has received the great attention to reveal the lysosomal function and their association to diseases, which could be useful to develop new therapeutic approaches. To obtain the reliable dataset of proteomic analysis, the isolation of lysosome is crucial. The current established isolation techniques are highlighted. Among those technique, magnetic isolation of intravascular magnetized lysosomes is a promising technique to obtain the fraction of intact lysosomes with high yield and purity. To further refine this technique, we proposed a robust nanoparticle-based magnetic separation method for intact lysosomes using multifunctional magnetic plasmonic nanoparticles.

In chapter 2, we present the preparation of AgFeCoAg NPs by polyol method. The TEM size of obtained nanoparticles was 14.8 nm. the MPNPs were encapsulated in phospholipid micelles followed by conjugation with amino dextran . The hydrodynamic size of aDxt-conjugated MPNPs was approximately 50 nm at pH levels 4–10, which is suitable for efficient cellular uptake through various pathways. In culture medium, aDxt-

MPNPs showed a high colloidal stability with reduced toxicity.

In chapter 3, we demonstrated the feasibility of using MPNPs for plasmonic imaging by confocal laser scanning microscopy. The degree of colocalization of the aDxt-MPNPs and each organelle was evaluated using the threshold Manders' colocalization coefficient (R_t). Based on time evolution of the colocalization of MPNPs with each organelle, their kinetic transport in COS-1 cell model is revealed.

In chapter 4, after determining the intracellular fate of the aDxt-MPNPs, lysosomes were quickly isolated using a MACS separator (Miltenyi Biotec). The purity and intactness/integrity of the lysosome fraction were confirmed by Western blot and confocal laser scanning microscopy, respectively. Finally, we demonstrated that the elapsed time from homogenization to complete isolation of lysosomes (t_{delay}) and temperature could potentially influence the protein composition of isolated lysosome fractions by sodium dodecyl sulfate-polyacrylamide gel electrophoresis (SDS-PAGE) and amino acid analysis using high-performance liquid chromatography (HPLC). In addition, our protocol showed the better performance in term of yield, purity and isolation time compared with density-gradient centrifugation technique. finally, we demonstrated the possibility of adapting our protocol to other cells line.

In chapter 5, the general summary and the future outlook of this dissertation work are disseminated.

References

1. de Duve, C., The Lysosome Concept. *Ciba Foundation Symposium - Anterior Pituitary Secretion (Book I of Colloquia on Endocrinology)* **1963**, 1-35.

2. De Duve, C.; Pressman, B. C.; Gianetto, R.; Wattiaux, R.; Appelmans, F., Tissue fractionation studies. 6. Intracellular distribution patterns of enzymes in rat-liver tissue. *Biochem J* **1955,** *60* (4), 604-17.

3. Luzio, J. P.; Pryor, P. R.; Bright, N. A., Lysosomes: fusion and function. *Nat Rev Mol Cell Biol* **2007,** *8* (8), 622-32.

4. Savini, M.; Zhao, Q.; Wang, M. C., Lysosomes: Signaling Hubs for Metabolic Sensing and Longevity. *Trends Cell Biol* **2019,** *29* (11), 876-887.

5. Graves, A. R.; Curran, P. K.; Smith, C. L.; Mindell, J. A., The Cl-/H+ antiporter ClC-7 is the primary chloride permeation pathway in lysosomes. *Nature* **2008,** *453* (7196), 788-92.

6. Mindell, J. A., Lysosomal acidification mechanisms. *Annu Rev Physiol* **2012,** *74*, 69-86.

7. Meyer-Schwesinger, C., Lysosome function in glomerular health and disease. *Cell Tissue Res* **2021,** *385* (2), 371-392.

8. Xiong, J.; Zhu, M. X., Regulation of lysosomal ion homeostasis by channels and transporters. *Sci China Life Sci* **2016,** *59* (8), 777-91.

9. Huynh, K. K.; Eskelinen, E. L.; Scott, C. C.; Malevanets, A.; Saftig, P.; Grinstein, S., LAMP proteins are required for fusion of lysosomes with phagosomes. *EMBO J* **2007,** *26* (2), 313-24.

10. Nam, S. E.; Cheung, Y. W. S.; Nguyen, T. N.; Gong, M.; Chan, S.; Lazarou, M.; Yip, C. K., Insights on autophagosome-lysosome tethering from structural and biochemical characterization of human autophagy factor EPG5. *Commun Biol* **2021,** *4* (1), 291.

11. Minton, K., How lysosomes SNARE autophagosomes. *Nature Reviews*

Molecular Cell Biology **2013,** *14* (2), 65-65.

12. Stenmark, H., Rab GTPases as coordinators of vesicle traffic. *Nat Rev Mol Cell Biol* **2009,** *10* (8), 513-25.

13. Xing, R.; Zhou, H.; Jian, Y.; Li, L.; Wang, M.; Liu, N.; Yin, Q.; Liang, Z.; Guo, W.; Yang, C., The Rab7 effector WDR91 promotes autophagy-lysosome degradation in neurons by regulating lysosome fusion. *J Cell Biol* **2021,** *220* (8).

14. Sardiello, M.; Palmieri, M.; di Ronza, A.; Medina, D. L.; Valenza, M.; Gennarino, V. A.; Di Malta, C.; Donaudy, F.; Embrione, V.; Polishchuk, R. S.; Banfi, S.; Parenti, G.; Cattaneo, E.; Ballabio, A., A gene network regulating lysosomal biogenesis and function. *Science* **2009,** *325* (5939), 473-7.

15. Settembre, C.; Fraldi, A.; Medina, D. L.; Ballabio, A., Signals from the lysosome: a control centre for cellular clearance and energy metabolism. *Nat Rev Mol Cell Biol* **2013,** *14* (5), 283-96.

16. Zoncu, R.; Efeyan, A.; Sabatini, D. M., mTOR: from growth signal integration to cancer, diabetes and ageing. *Nat Rev Mol Cell Biol* **2011,** *12* (1), 21-35.

17. Puertollano, R., mTOR and lysosome regulation. *F1000Prime Rep* **2014,** *6*, 52.

18. Asrani, K.; Murali, S.; Lam, B.; Na, C. H.; Phatak, P.; Sood, A.; Kaur, H.; Khan, Z.; Noe, M.; Anchoori, R. K.; Talbot, C. C., Jr.; Smith, B.; Skaro, M.; Lotan, T. L., mTORC1 feedback to AKT modulates lysosomal biogenesis through MiT/TFE regulation. *J Clin Invest* **2019,** *129* (12), 5584-5599.

19. Peng, W.; Jewell, J. L., Amino Acid Sensing: Architecture of mTORC1 on the Lysosome Surface. *Curr Biol* **2020,** *30* (2), R89-R91.

20. Zoncu, R.; Bar-Peled, L.; Efeyan, A.; Wang, S.; Sancak, Y.; Sabatini, D. M., mTORC1 senses lysosomal amino acids through an inside-out mechanism that requires the vacuolar H(+)-ATPase. *Science* **2011,** *334* (6056), 678-83.

21. da Costa, A.; Metais, T.; Mouthon, F.; Kerkovich, D.; Charveriat, M.,

Evaluating and modulating TFEB in the control of autophagy: toward new treatments in CNS disorders. *Fundam Clin Pharmacol* **2021,** *35* (3), 539-551.

22. Mehta, A.; Beck, M.; Linhart, A.; Sunder-Plassmann, G.; Widmer, U., History of lysosomal storage diseases: an overview. In *Fabry Disease: Perspectives from 5 Years of FOS*, Mehta, A.; Beck, M.; Sunder-Plassmann, G., Eds. Oxford, 2006.

23. Hers, H. G., alpha-Glucosidase deficiency in generalized glycogenstorage disease (Pompe's disease). *Biochem J* **1963,** *86*, 11-6.

24. Van Hoof, F., Mucopolysaccharidoses and mucolipidoses. *J Clin Pathol Suppl (R Coll Pathol)* **1974,** *8*, 64-93.

25. Clarke, L. A., Pathogenesis of skeletal and connective tissue involvement in the mucopolysaccharidoses: glycosaminoglycan storage is merely the instigator. *Rheumatology (Oxford)* **2011,** *50 Suppl 5*, v13-8.

26. Stirnemann, J.; Belmatoug, N.; Camou, F.; Serratrice, C.; Froissart, R.; Caillaud, C.; Levade, T.; Astudillo, L.; Serratrice, J.; Brassier, A.; Rose, C.; Billette de Villemeur, T.; Berger, M. G., A Review of Gaucher Disease Pathophysiology, Clinical Presentation and Treatments. *Int J Mol Sci* **2017,** *18* (2).

27. Paganini, C.; Costantini, R.; Superti-Furga, A.; Rossi, A., Bone and connective tissue disorders caused by defects in glycosaminoglycan biosynthesis: a panoramic view. *FEBS J* **2019,** *286* (15), 3008-3032.

28. La Cognata, V.; Guarnaccia, M.; Polizzi, A.; Ruggieri, M.; Cavallaro, S., Highlights on Genomics Applications for Lysosomal Storage Diseases. *Cells* **2020,** *9* (8).

29. Parenti, G.; Medina, D. L.; Ballabio, A., The rapidly evolving view of lysosomal storage diseases. *EMBO Mol Med* **2021,** *13* (2), e12836.

30. Platt, F. M.; d'Azzo, A.; Davidson, B. L.; Neufeld, E. F.; Tifft, C. J., Lysosomal storage diseases. *Nat Rev Dis Primers* **2018,** *4* (1), 27.

31. Jeyakumar, M.; Dwek, R. A.; Butters, T. D.; Platt, F. M., Storage solutions: treating lysosomal disorders of the brain. *Nat Rev Neurosci* **2005,** *6* (9), 713-25.

32. Beck, M., Treatment strategies for lysosomal storage disorders. *Dev Med Child Neurol* **2018,** *60* (1), 13-18.

33. Radulovic, M.; Schink, K. O.; Wenzel, E. M.; Nahse, V.; Bongiovanni, A.; Lafont, F.; Stenmark, H., ESCRT-mediated lysosome repair precedes lysophagy and promotes cell survival. *EMBO J* **2018,** *37* (21).

34. Ballabio, A.; Bonifacino, J. S., Lysosomes as dynamic regulators of cell and organismal homeostasis. *Nat Rev Mol Cell Biol* **2020,** *21* (2), 101-118.

35. Muthukottiappan, P.; Winter, D., A proteomic view on lysosomes. *Mol Omics* **2021,** *17* (6), 842-859.

36. Abu-Remaileh, M.; Wyant, G. A.; Kim, C.; Laqtom, N. N.; Abbasi, M.; Chan, S. H.; Freinkman, E.; Sabatini, D. M., Lysosomal metabolomics reveals V-ATPase- and mTOR-dependent regulation of amino acid efflux from lysosomes. *Science* **2017,** *358* (6364), 807-813.

37. Xiong, J.; He, J. Q.; Xie, W. P.; Hinojosa, E.; Ambati, C. S. R.; Putluri, N.; Kim, H. E.; Zhu, M. X.; Du, G. W., Rapid affinity purification of intracellular organelles using a twin strep tag. *J Cell Sci* **2019,** *132* (24).

38. Arias, E.; Cuervo, A. M., Chaperone-mediated autophagy in protein quality control. *Curr Opin Cell Biol* **2011,** *23* (2), 184-9.

39. Kacal, M.; Zhang, B.; Hao, Y.; Norberg, E.; Vakifahmetoglu-Norberg, H., Quantitative proteomic analysis of temporal lysosomal proteome and the impact of the KFERQ-like motif and LAMP2A in lysosomal targeting. *Autophagy* **2021,** *17* (11), 3865-3874.

40. Markmann, S.; Thelen, M.; Cornils, K.; Schweizer, M.; Brocke-Ahmadinejad, N.; Willnow, T.; Heeren, J.; Gieselmann, V.; Braulke, T.; Kollmann, K., Lrp1/LDL Receptor Play Critical Roles in Mannose 6-Phosphate-Independent Lysosomal Enzyme Targeting. *Traffic* **2015,** *16* (7), 743-59.

41. Tuermer, A.; Mausbach, S.; Kaade, E.; Damme, M.; Sylvester, M.;

Gieselmann, V.; Thelen, M., CLN6 deficiency causes selective changes in the lysosomal protein composition. *Proteomics* **2021,** *21* (19), e2100043.

42. di Ronza, A.; Bajaj, L.; Sharma, J.; Sanagasetti, D.; Lotfi, P.; Adamski, C. J.; Collette, J.; Palmieri, M.; Amawi, A.; Popp, L.; Chang, K. T.; Meschini, M. C.; Leung, H. E.; Segatori, L.; Simonati, A.; Sifers, R. N.; Santorelli, F. M.; Sardiello, M., CLN8 is an endoplasmic reticulum cargo receptor that regulates lysosome biogenesis. *Nat Cell Biol* **2018,** *20* (12), 1370-1377.

43. Bajaj, L.; Sharma, J.; di Ronza, A.; Zhang, P.; Eblimit, A.; Pal, R.; Roman, D.; Collette, J. R.; Booth, C.; Chang, K. T.; Sifers, R. N.; Jung, S. Y.; Weimer, J. M.; Chen, R.; Schekman, R. W.; Sardiello, M., A CLN6-CLN8 complex recruits lysosomal enzymes at the ER for Golgi transfer. *J Clin Invest* **2020,** *130* (8), 4118-4132.

44. Schmidtke, C.; Tiede, S.; Thelen, M.; Kakela, R.; Jabs, S.; Makrypidi, G.; Sylvester, M.; Schweizer, M.; Braren, I.; Brocke-Ahmadinejad, N.; Cotman, S. L.; Schulz, A.; Gieselmann, V.; Braulke, T., Lysosomal proteome analysis reveals that CLN3-defective cells have multiple enzyme deficiencies associated with changes in intracellular trafficking. *J Biol Chem* **2019,** *294* (24), 9592-9604.

45. Tharkeshwar, A. K.; Trekker, J.; Vermeire, W.; Pauwels, J.; Sannerud, R.; Priestman, D. A.; te Vruchte, D.; Vints, K.; Baatsen, P.; Decuypere, J. P.; Lu, H. Q.; Martin, S.; Vangheluwe, P.; Swinnen, J. V.; Lagae, L.; Impens, F.; Platt, F. M.; Gevaert, K.; Annaert, W., A novel approach to analyze lysosomal dysfunctions through subcellular proteomics and lipidomics: the case of NPC1 deficiency. *Sci Rep-Uk* **2017,** *7*.

46. Zhang, H.; Fan, X.; Bagshaw, R. D.; Zhang, L.; Mahuran, D. J.; Callahan, J. W., Lysosomal membranes from beige mice contain higher than normal levels of endoplasmic reticulum proteins. *J Proteome Res* **2007,** *6* (1), 240-9.

47. Costanzo, M.; Zacchia, M.; Bruno, G.; Crisci, D.; Caterino, M.; Ruoppolo, M., Integration of Proteomics and Metabolomics in Exploring Genetic and

Rare Metabolic Diseases. *Kidney Dis (Basel)* **2017,** *3* (2), 66-77.

48. Cologna, S. M.; Jiang, X. S.; Backlund, P. S.; Cluzeau, C. V.; Dail, M. K.; Yanjanin, N. M.; Siebel, S.; Toth, C. L.; Jun, H. S.; Wassif, C. A.; Yergey, A. L.; Porter, F. D., Quantitative proteomic analysis of Niemann-Pick disease, type C1 cerebellum identifies protein biomarkers and provides pathological insight. *PLoS One* **2012,** *7* (10), e47845.

49. Matafora, V.; Cuccurullo, M.; Beneduci, A.; Petrazzuolo, O.; Simeone, A.; Anastasio, P.; Mignani, R.; Feriozzi, S.; Pisani, A.; Comotti, C.; Bachi, A.; Capasso, G., Early markers of Fabry disease revealed by proteomics. *Mol Biosyst* **2015,** *11* (6), 1543-51.

50. Sleat, D. E.; Donnelly, R. J.; Lackland, H.; Liu, C. G.; Sohar, I.; Pullarkat, R. K.; Lobel, P., Association of mutations in a lysosomal protein with classical late-infantile neuronal ceroid lipofuscinosis. *Science* **1997,** *277* (5333), 1802-5.

51. Itzhak, D. N.; Tyanova, S.; Cox, J.; Borner, G. H., Global, quantitative and dynamic mapping of protein subcellular localization. *Elife* **2016,** *5*.

52. Itzhak, D. N.; Davies, C.; Tyanova, S.; Mishra, A.; Williamson, J.; Antrobus, R.; Cox, J.; Weekes, M. P.; Borner, G. H. H., A Mass Spectrometry-Based Approach for Mapping Protein Subcellular Localization Reveals the Spatial Proteome of Mouse Primary Neurons. *Cell Rep* **2017,** *20* (11), 2706-2718.

53. Valm, A. M.; Cohen, S.; Legant, W. R.; Melunis, J.; Hershberg, U.; Wait, E.; Cohen, A. R.; Davidson, M. W.; Betzig, E.; Lippincott-Schwartz, J., Applying systems-level spectral imaging and analysis to reveal the organelle interactome. *Nature* **2017,** *546* (7656), 162-167.

54. Graham, J. M., Isolation of lysosomes from tissues and cells by differential and density gradient centrifugation. *Curr Protoc Cell Biol* **2001,** *Chapter 3*, Unit 3 6.

55. Pryor, P. R., Isolating Lysosomes from Rat Liver. *Cold Spring Harb Protoc* **2016,** *2016* (4), pdb prot084814.

56. Parent, N.; Winstall, E.; Beauchemin, M.; Paquet, C.; Poirier, G. G.; Bertrand, R., Proteomic analysis of enriched lysosomes at early phase of camptothecin-induced apoptosis in human U-937 cells. *J Proteomics* **2009,** *72* (6), 960-73.

57. Wattiaux, R.; Wattiaux-De Coninck, S.; Ronveaux-dupal, M. F.; Dubois, F., Isolation of rat liver lysosomes by isopycnic centrifugation in a metrizamide gradient. *J Cell Biol* **1978,** *78* (2), 349-68.

58. Beaumelle, B. D.; Gibson, A.; Hopkins, C. R., Isolation and preliminary characterization of the major membrane boundaries of the endocytic pathway in lymphocytes. *J Cell Biol* **1990,** *111* (5 Pt 1), 1811-23.

59. Ponsford, A. H.; Ryan, T. A.; Raimondi, A.; Cocucci, E.; Wycislo, S. A.; Frohlich, F.; Swan, L. E.; Stagi, M., Live imaging of intra-lysosome pH in cell lines and primary neuronal culture using a novel genetically encoded biosensor. *Autophagy* **2021,** *17* (6), 1500-1518.

60. Nylandsted, J.; Becker, A. C.; Bunkenborg, J.; Andersen, J. S.; Dengjel, J.; Jaattela, M., ErbB2-associated changes in the lysosomal proteome. *Proteomics* **2011,** *11* (14), 2830-8.

61. Kimple, M. E.; Brill, A. L.; Pasker, R. L., Overview of affinity tags for protein purification. *Curr Protoc Protein Sci* **2013,** *73*, 9 9 1-9 9 23.

62. Singh, J.; Kaade, E.; Muntel, J.; Bruderer, R.; Reiter, L.; Thelen, M.; Winter, D., Systematic Comparison of Strategies for the Enrichment of Lysosomes by Data Independent Acquisition. *J Proteome Res* **2020,** *19* (1), 371-381.

63. Diettrich, O.; Mills, K.; Johnson, A. W.; Hasilik, A.; Winchester, B. G., Application of magnetic chromatography to the isolation of lysosomes from fibroblasts of patients with lysosomal storage disorders. *FEBS Lett* **1998,** *441* (3), 369-72.

64. Chen, F. W.; Gordon, R. E.; Ioannou, Y. A., NPC1 late endosomes contain elevated levels of non-esterified ('free') fatty acids and an abnormally glycosylated form of the NPC2 protein. *Biochem J* **2005,** *390* (Pt 2), 549-61.

65. Berry, C. C.; Wells, S.; Charles, S.; Curtis, A. S., Dextran and albumin derivatised iron oxide nanoparticles: influence on fibroblasts in vitro. *Biomaterials* **2003,** *24* (25), 4551-7.

66. Schroder, B. A.; Wrocklage, C.; Hasilik, A.; Saftig, P., The proteome of lysosomes. *Proteomics* **2010,** *10* (22), 4053-76.

67. Akter, F.; Ponnaiyan, S.; Kögler-Mohrbacher, B.; Bleibaum, F.; Damme, M.; Renard, B. Y.; Winter, D., Multi cell line analysis of lysosomal proteomes reveals unique features and novel lysosomal proteins. **2020**, 2020.12.21.423747.

68. Uzhytchak, M.; Smolková, B.; Lunova, M.; Jirsa, M.; Frtús, A.; Kubinová, Š.; Dejneka, A.; Lunov, O., Iron Oxide Nanoparticle-Induced Autophagic Flux Is Regulated by Interplay between p53-mTOR Axis and Bcl-2 Signaling in Hepatic Cells. **2020,** *9* (4), 1015.

69. Ma, X.; Wu, Y.; Jin, S.; Tian, Y.; Zhang, X.; Zhao, Y.; Yu, L.; Liang, X.-J., Gold Nanoparticles Induce Autophagosome Accumulation through Size-Dependent Nanoparticle Uptake and Lysosome Impairment. *ACS Nano* **2011,** *5* (11), 8629-8639.

70. Choudhury, A.; Marks, D. L.; Pagano, R. E., Use of Rab GTPases to study lipid trafficking in normal and sphingolipid storage disease fibroblasts. *Methods Enzymol* **2005,** *403*, 166-82.

71. Lloyd-Evans, E.; Morgan, A. J.; He, X. X.; Smith, D. A.; Elliot-Smith, E.; Sillence, D. J.; Churchill, G. C.; Schuchman, E. H.; Galione, A.; Platt, F. M., Niemann-Pick disease type C1 is a sphingosine storage disease that causes deregulation of lysosomal calcium. *Nat Med* **2008,** *14* (11), 1247-1255.

72. Alamo, P.; Pallares, V.; Cespedes, M. V.; Falgas, A.; Sanchez, J. M.; Serna, N.; Sanchez-Garcia, L.; Volta-Duran, E.; Morris, G. A.; Sanchez-Chardi, A.; Casanova, I.; Mangues, R.; Vazquez, E.; Villaverde, A.; Unzueta, U., Fluorescent Dye Labeling Changes the Biodistribution of Tumor-Targeted Nanoparticles. *Pharmaceutics* **2020,** *12* (11).

73. Snipstad, S.; Hak, S.; Baghirov, H.; Sulheim, E.; Morch, Y.; Lelu, S.; von Haartman, E.; Back, M.; Nilsson, K. P. R.; Klymchenko, A. S.; de Lange Davies, C.; Aslund, A. K. O., Labeling nanoparticles: Dye leakage and altered cellular uptake. *Cytometry A* **2017,** *91* (8), 760-766.

74. Mahmoud, K. A.; Mena, J. A.; Male, K. B.; Hrapovic, S.; Kamen, A.; Luong, J. H., Effect of surface charge on the cellular uptake and cytotoxicity of fluorescent labeled cellulose nanocrystals. *ACS Appl Mater Interfaces* **2010,** *2* (10), 2924-32.

Chapter 2: Preparation of magnetic plasmonic nanoparticles for targeting lysosomes through the endocytic pathway

2.1. Introduction

Nanobiotechnology is a newly emerging research area, which employs nanostructures with unique physicochemical properties to create the novel tools for diagnosis, therapy, and study of biological phenomena.[1-3] With the advancement in nanotechnology, various types of nanoparticles have been successfully prepared using inorganic and organic substances such as quantum dot, magnetic nanoparticles, plasmonic nanoparticles, micelles and polymeric nanoparticles. Among them, magnetic nanoparticles and plasmonic nanoparticles are intensively exploited which have resulted many potential applications in life science.[4-7] The key advantage of magnetic nanoparticles is the ability to magnetically manipulate individual particles in non-contact mode using external magnetic field without perturbation of biological systems to design different applications of interest such as hyperthermia, magnetic separation and magnetic resonance imaging. On the other hand, the plasmonic nanoparticles such as gold and silver have the unique optical property originated from their large molar extinction coefficients, high Rayleigh scattering efficiency and the sensitivity of LSPR in response to the changes of dielectric environment, which are often employed in photothermal therapy, photoacoustic imaging, optical imaging, and biosensors. Importantly, noble metals do not suffer photobleaching as fluorescent dye and optical blinking as quantum dot, while their cytotoxicity is considerably lower than that of semiconductor quantum dot.[8, 9]

Recently, the integration of multifunctional components into a single nanoplatform has

received the great attention because the applicability of such multimodal nanostructures could be significantly broaden compared to the individual materials. As mentioned above, the plasmonic nanoparticles and magnetic nanoparticles has currently drawn the considerable attention in various biological applications. Consequently, the fabrication of nanoparticles with dual magnetic and plasmonic properties become emergent, this bifunctionality could offer new applications in labeling, imaging, and separation of biological targets. Thanks to the versability of nanotechnology, different approaches have been proposed to incorporate magnetic and plasmonic components into a single nanostructures like core-shell,[10, 11] yolk-shell[12, 13] and heterodimer[14, 15].

In this work, to prepare multifunctional hetero-nanostructures exhibiting magnetic and plasmonic properties, one pot synthesis using hot injection and polyol process was employed. It should be emphasized that the polyol process is a well-known soft chemical method, which is extensively used for preparation of different kind of monodisperse metallic nanoparticles.[16] The advantages of this technique are ease of use, cost-effectiveness, and scalability. Of note, compared to the individual magnetic nanoparticles, magnetic susceptibility of the hybrid structure tends to be reduced due to their combination with non-magnetic materials. Therefore, to achieve a hetero-nanostructure with the excellent magnetic and optical properties, we choose the FeCo and Ag as the magnetic and plasmonic components, respectively. Because FeCo is the strongest magnetic materials, while Ag shows the highest scattering cross-section among plasmonic nanoparticles. In particular, this nanostructure consists of an Ag core, followed by a layer of FeCo, and the outermost submonolayer of Ag.[17] The formation mechanism was studied and reported in our previous research.[18] The important characteristics of this structural design are the suppression of FeCo oxidation by electron transfer from Ag core to FeCo

shell and the enhancement of conjugation capability due to the presence of Ag shell.[17, 19]

Since the obtained MPNPs were hydrophobic, the surface modification is required before introducing to biological system. In this particular study, the MPNPs are delivered to lysosomal lumen through endocytic pathway to label lysosomes for magnetic separation. To achieve this purpose, the control of colloidal stability, nonspecific absorption and the biointerfaces of magnetic nanoparticles is crucial, which not only affects the uptake efficiency but also the intracellular fate of nanoparticles. To make MPNPs water dispersion, the encapsulation of MPNPs in phospholipid micelles are performed. Following this, aDxt is conjugated on the surface of MPNPs because dextran has been well-known as a fluid phase cargo internalized via pinocytosis rather than receptor-mediated endocytosis and eventually delivered to lysosomes. The hydrodynamic size of aDxt-conjugated MPNPs was ~50 nm at pH in the range of 4~10, which is suitable for efficient cellular uptake through various pathways. Furthermore, the colloidal stability, cytotoxicity and cellular uptake of MPNPs in culture medium were also investigated in this chapter.

2.2. Experiments

2.2.1. Chemicals

Table 2.1 Chemicals used in preparation of aDxt-MPNPs

Chemicals	**Formula/Abbreviation**	**Sources**
Argon gas, > 99.9999 vol.%	Ar gas	
Cobalt (II) acetylacetonate, 97%	Co precursor	Sigma-Aldrich
Iron (III) acetylacetonate, 99.99%	Fe precursor	Sigma-Aldrich
Silver nitrate, 99.9999 %	Ag precursor	Sigma-Aldrich
1,2-hexadecanediol, 90%	HDD	Sigma-Aldrich
Oleylamine	OLA	Sigma-Aldrich
Oleic acid, 90%	OA	Sigma-Aldrich
Tetraethylene glycol, 99%	$C_8H_{18}O_5$	Sigma-Aldrich
Acetone, 99.5%	C_3H_6O	Kanto Chemical
Hexane, 96%	C_6H_{14}	Kanto Chemical
Chloroform, 99%	$CHCl_3$	Kanto Chemical
Toluene, 99%	C_7H_8	Wako Pure Chemical
1,2-dioleoyl-sn-glycerol-3-phosphoethanolamine-N-[methoxy(polyethylene glycol)-350]	PEG350-DOPE	Avanti
1,2-dioleoyl-sn-glycerol-3-phosphoethanolamine-N-(glutaryl)	18:1 Glutaryl PE	Avanti
*2-morpholinoethanesulfonic acid, monohydrate	MES	Dojindo
N-hydroxysuccinimide	NHS	Thermo Fisher Scientific
Ethyl-3-(3-dimethyl aminopropyl) carbodiimide	EDC	Dojindo
Amino dextran, MW. 10000	aDxt	Thermo Fisher Scientific
*Dulbecco's phosphate buffer	PBS	Nissui Pharmaceutical

** See recipe*

❖ **Recipes:**

1. MES buffer (0.1 M, pH ~ 6)

Dissolve 3.90 g MES in 180 mL deionized water. Monitor the pH of the solution using a pH meter, then take 10 N sodium hydroxide aqueous solution using a micropipette to adjust the pH of the solution to around 6. Then add water up to 200 mL. Sterilize the solution by filtration through 0.2 μm filter before use. Store in the dark colored bottle.

2. PBS Buffer

Dissolve 9.6 g of PBS in 1 L of deionized water. The solution should be sterilized by an autoclave before use. Store the solution at 4°C.

2.2.2. Preparation of MPNPs by a combination of a polyol and a one-pot synthesis

- Weigh 0.1 mmol of silver nitrate and 1.0 mmol of 1,2-hexadecanediol.
- Place an oval magnetic stirring bar in the three-neck round bottom flask and transfer the weighed silver nitrate followed by 1,2-hexadecanediol into the flask. Then sequentially, add 10 mL of tetraethylene glycol, 10 mmol (3.29 mL) of oleylamine, and 8 mmol (2.55 mL) of oleic acid using a pipette.

Note: After removing oleyamine and oleic acid bottles from the refrigerator, place them into a water bath at 35°C until completely melted, then take the required volume using a pipette.

- Prepare two 13.5 mL glass vials.
- Weigh 0.2 mmol of cobalt (II) acetylacetonate and 0.2 mmol of iron (III) acetylacetonate. Transfer them to a glass vial labeled as Co and Fe precursors. Then sequentially, add 2 mL of oleylamine and 1 mL of toluene.

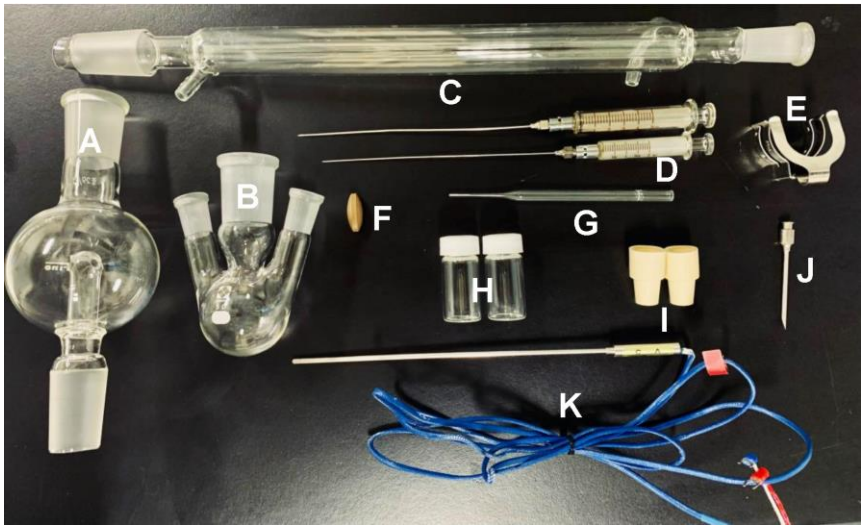

Figure 2.1: The glassware for preparation of MPNPs. (A) Trap sphere, (B) three-neck round bottom flask, (C) Liebig type reflux condenser, (D) glass syringes with needles, I clamp, (F) oval magnetic stir bar, (G) Pasteur pipette, (H) glass vials, (I) septum rubbers, (J) needle, and (K) thermocouple.

- Prepare the glassware for synthesis of MPNPs as shown in Figure 2.1
- Weigh 0.1 mmol of silver nitrate and transfer it to the remaining glass vial labeled as Ag precursor. Then sequentially, add 1 ml of oleylamine and 1 mL of toluene.
- Seal the caps of the two vials with a paraffin membrane (Amcor, Parafilm M, catalog number: PM996) and place them in a sonicator (AS One, Ultrasonic Cleaner ASU-6, oscillation frequency: 40 kHz) with High Power Mode for complete dissolving of all reagents.

Note: To dissolve the reagents quickly, the vials could be warmed around 40℃ during this process. There is no time limit for this step, but they should be ready before the injection steps.

- Prepare two septums as shown in Figure 2.2.

Note: Use the 12G-needle to make a hole to insert the Pasteur pipette into the rubber septum. Adding some ethanol to the hole makes the insertion easier. Ethanol will evaporate after insertion.

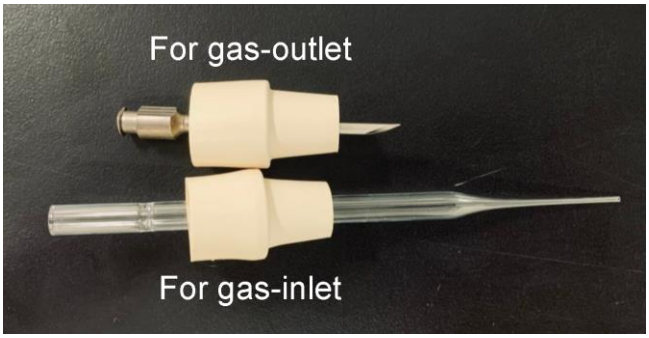

Figure 2.2: The septum rubbers prepared for Ar bubbling. Later on, the needle is removed from the septum (top) to insert a thermocouple.

- Place the three-neck round bottom flask containing the reaction raw materials (prepared in step 2) on the mantle heater.
- Connect the trap sphere to the center neck of the flask, hold them with a clamp. Then, plug in the condenser tube and connect the other end of the condenser to a trapper containing liquid paraffin (Figure 2.3).

Note: The reflux condenser uses air without running water.

- Seal two remaining open necks using septums shown in Figure 2.2

Note: The tip of the Pasteur pipette for Ar bubbling should be dipped into reaction solution but not touch the magnetic stirring bar.

- Turn on the magnetic stirrer at a speed of around 150 rpm and pump in Ar gas through the Pasteur pipette with the flow rate of 0.35 L/min. The gas flows out through the 12G-needle. Leave it for 5 min for the replacement of the atmosphere in the flask with Ar gas.
- Remove the needle and insert a thermocouple.
- Turn on the temperature controller and set the temperature to 100°C.

Note: Due to the high viscosity of the solution at RT, the stirring speed cannot be set

immediately at 500 rpm. Therefore, while the temperature increases, increase the stirring speed slowly. At 50°C, the stirring speed could be fully set at 500 rpm. The heating rate of this step is about 12−13°C/min.

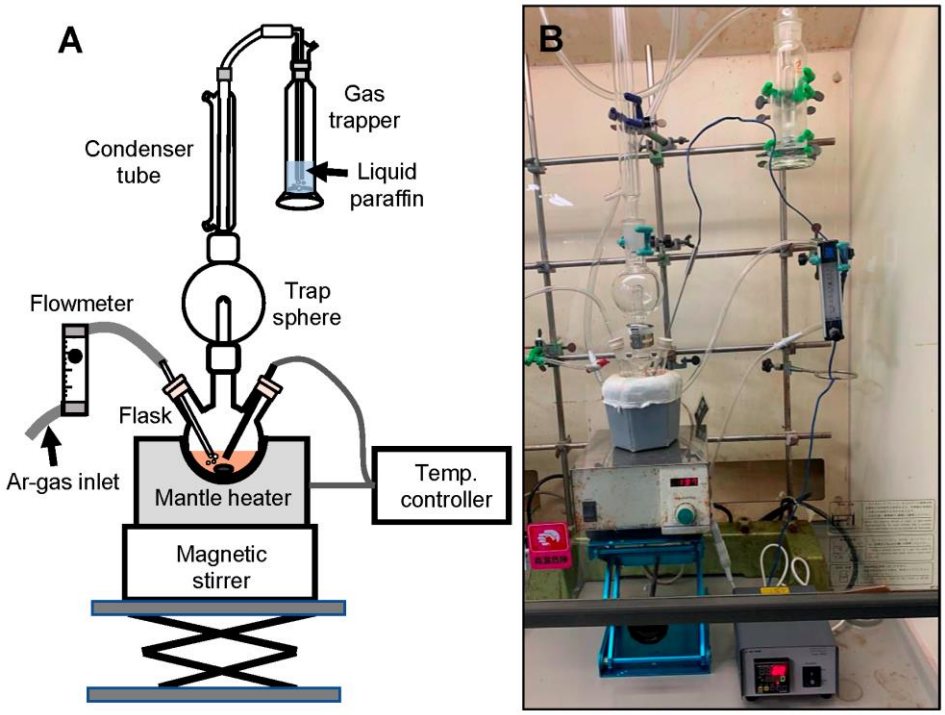

Figure 2.3: (A) The illustration and (B) photograph of the experimental setup for preparing MPNPs.

- From the moment the temperature reaches 100°C, maintain it for 10 min. During this step, the silver seeds are formed.

Note: Overheating may be observed, in which the temperature is elevated above 100°C. Slightly lowering the heating mantel to reduce its contact with the flask will reduce the temperature.

- After 10 min, increase the temperature to 250°C by setting the temperature controller at 300°C. Note: The purpose of this setting is to linearly rise the temperature up to 250°C (Figure 2.4).

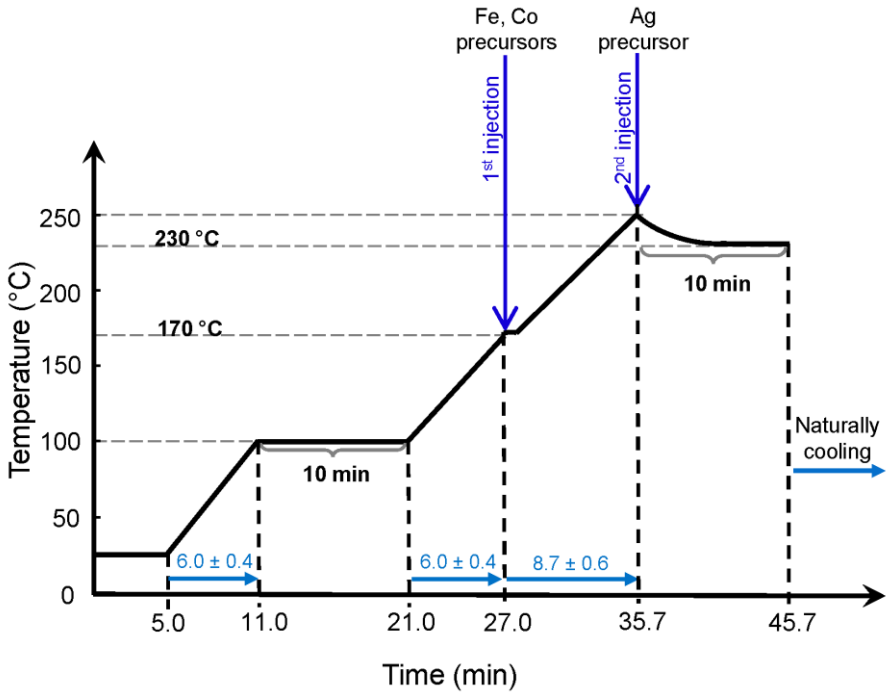

Figure 2.4: Temperature profile of the preparation process of MPNPs.

- During temperature increase, once it reaches 170°C, inject the pre-prepared mixture of iron and cobalt precursors using a glass syringe and 20 G-needle.

Note: The needle is inserted via the septum containing the thermocouple. Inject the solution drop by drop at a fast pace for a duration of 1 min. The temperature should be kept around 170°C by slightly lowering the heating mantle to reduce contact with the flask. The heating rate from 100°C to 170°C is about 12°C/min.

- Once the temperature reaches 250°C, inject the pre-prepared Ag precursor using a glass syringe and another 20G-needle. Then immediately reset the temperature of the controller to 230°C. Maintain the reaction for 10 min.

Note: This is the most important step. The injection of Ag precursor is normally done in about 20 s. It should not be less than 10 s or longer than 30 s. After the injection, slightly lower the heating mantle to reduce contact with the flask to avoid overheating. We

confirmed that reaction time can be prolonged to 15 min but the quality of the MPNPs was not influenced. The heating rate from 170°C to 250°C is about 9°C/min.

- Set the temperature controller to 0°C to stop heating and remove the mantle heater. Wait for the reaction system to cool off naturally while continuing stirring and Ar bubbling. At this time, some of the synthesized particles will be attached to the magnetic stirring bar but they will be redispersed again during the cooling process.
- Once the temperature of reaction solution is less than 70°C, stop Ar gas flow and turn off the magnetic stirrer.
- Carefully disassemble the setup and use a pipette to transfer the reaction solution from the three-neck flask to two 50-mL centrifuge tubes evenly.
- Add acetone to fill the tube to 45 mL. Then, perform centrifugation using a Kubota 5910 at 4,640 × g for 5 min at RT.
- Discard all supernatant and add 400 µL of hexane to each tube for redispersion of MPNPs.
- Use a micropipette to transfer 200 µL of redispersed MPNP solution to two other 50 mL tubes. Subsequently, fill with acetone up to 45 mL in total and perform centrifugation using Kubota 5910 at 4,640 × g for 5 min at RT.
- Discard supernatant and redisperse obtained MPNPs in 3 mL of chloroform. Determine the concentration of MPNP dispersion using the absorption spectrum measured by ultraviolet-visible absorption spectrophotometer.

Note: The concentration of MPNPs was determined using a calibration curve of y = 0.024x, where y: the absorption peak value of localized surface plasmon resonance from the MPNPs, x: the concentration of MPNPs (µg/mL).

- Store obtained MPNPs in chloroform at 4°C in a glass vial with closed-top cap. Seal it with Parafilm.

2.2.3. Encapsulation of MPNPs in PEGylated phospholipids

- Prepare a 50-mL two-neck round bottom flask (Figure 2.5A).
- Pour 3 mL of MPNPs dispersed in chloroform with a concentration of 1 mg/mL into the flask. Subsequently, add 1350 µL of 18:1 glutaryl PE (5.5 mM) in chloroform and 900 µL of PEG350-DOPE (5.5 mM) in chloroform to the dispersion.
- Seal using septum rubbers, place the septum containing Pasteur pipette in the center neck and the septum containing needle to the angled neck.

Note: The tip of the Pasteur pipette should not dip in the dispersion.

- Pump in Ar gas at a rate of 0.5 L/min to completely evaporate chloroform (Figure 2.5B).

Note: In this step, the inert gas could be either Ar or N_2.

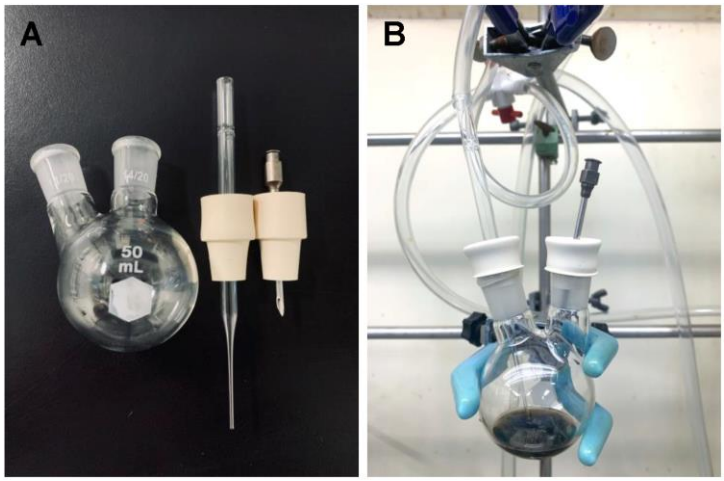

Figure 2.5: (A) The glassware and (B) the experimental setup for encapsulation of MPNPs in PEGylated phospholipids.

- Add 1.5 mL deionized water to redisperse the obtained precipitation. Collect the dispersion into two 1.5 mL centrifuge tubes.
- Centrifuge at 1,400 × g using Hitachi CF15RXII high-speed micro centrifuge for 5

min at RT to eliminate big aggregated particles.

- Carefully transfer the supernatant from the centrifugated tubes into two new 1.5 mL tubes. Then centrifuge at 86,600 × g using CS100FNX ultracentrifuge for 10 min at 4°C to remove empty micelles.

Note: In this step, if the MPNPs were not completely collected, increase the centrifugation speed up to 100,000 × g.

- Discard the supernatant and redisperse the obtained particles in 1 mL of deionized water.
- Determine the concentration of phospholipid encapsulated MPNPs from the absorption spectrum.

2.2.4. Conjugation of aDxt using EDC coupling reaction

- Add 20 mL of MES buffer (pH ~ 6) to a 100 mL one-neck round bottom flask containing a magnetic stirrer.
- Set the magnetic stirrer to 600 rpm.
- Add 1 mL of phospholipid encapsulated MPNPs dispersion (1 mg/mL) into the flask. Then, sequentially add 125 µL of EDC (200 mM) in deionized water and 250 µL of NHS (200 mM) in MES buffer. Leave it for 30 min at RT.

Note: After taking them out from refrigerator equilibrate the EDC and NHS to RT before use.

- Transfer the obtained reaction mixture into 20 × 1.5 mL tubes.
- Centrifuge at 86,600 × g using CS100FNX for 10 min at 4°C and carefully remove the supernatant.
- Use a micropipette to collect and redisperse obtained particles in 1 mL of PBS.

- Prepare a 100 mL one-neck round-bottom flask containing 19 mL of PBS.
- Add 50 mg of aDxt into the PBS solution in the flask (prepared in step 7) and wait for it to completely dissolve under magnetic stirring.
- Add the PBS dispersion of MPNPs (prepared in step 6) into the PBS solution of aDxt (prepared in step 8). Then, maintain the reaction for 90 min at RT.
- Transfer the obtained mixture to 20 × 1.5 mL tubes. Then, perform centrifugation at 60,000 × g using CS100FNX for 10 min at 4°C. Collect and redisperse the obtained particles in 1 mL PBS.
- Determine the concentration of aDxt-conjugated MPNPs (aDxt-MPNPs) in the dispersion from the absorption spectrum.

2.2.5. Cytotoxicity test

- Prepare 5,000 cells in 100 µL of DMEM (+10% FBS) in a 96-well black/clear bottom plate and cultured overnight.
- Check cell status using bright-field microscope (Keyence, model: BZ-X810) in advance.
- The next day, remove the culture medium and wash cells with PBS.
- Incubate cells in 100 µL of DMEM (+10%FBS) containing aDxt-MPNPs at concentrations (C_{NPs}) of 100 and 50 µg/mL for incubation times (t_{load}) of 1, 8, and 24 h at 37°C.

Note: To investigate the effect of serum on toxicity of aDxt-MPNPs, cells were incubated in 100 µL of DMEM (+0% FBS) containing aDxt-MPNPs at C_{NPs} = 100, 50, and 25 µg/mL for t_{load} = 1 h.

- After incubation process, wash cell with PBS one time and add 100 µL of PBS.

Subsequently, add 10 µL of working solution to each well.

Note: the working solution was prepared by adding 2 µL of Calcein-AM in DMSO solution into 98 µL of PBS.

- Incubate cell cultures for 20 min in the incubator.
- Measure fluorescent (Thermo Scientific Varioskan LUX) produced by the enzymatic hydrolysis process in living cells. The viability of the loaded cells compared with that of untreated control cells was calculated using the protocol provided by manufacturer:

$$\text{Viability (\%)} = [(A_s - A_b)/(A_c - A_b)] \times 100$$

A_s: Fluorescence intensity of sample (cell + test substance + CCK-F)

A_c: Fluorescence intensity of control (cell + CCK-F, no test substance)

A_b: Fluorescence intensity of blank (medium + CCK-F, no cell)

2.2.6. Determination of cellular metal uptake using inductively coupled plasma mass spectrometry (ICP-MS)

To evaluate time-dependent metal uptake by COS-1 cells, the amounts of Ag and Co were determined by ICP-MS after incubation with aDxt-MPNPs for t_{load} = 1 and 8 h.

- Prepare total of 4×10^6 cells for each condition and incubate overnight.
- The next day, remove the culture medium and wash cells with PBS.
- For cell starvation, add 5 mL of pre-warmed DMEM without FBS, and incubate for 30 min at 37°C under 5% CO_2.
- Immediately after starvation, replace DMEM without FBS with 5 mL of MPNPs (C_{NPs} = 100 µg/mL) dispersion in DMEM (+10% FBS), and incubate for t_{load} = 1 h & 8 h at 37°C under 5% CO_2.
- After loading for t_{load} = 1 and 8 h, discard the excess aDxt-MPNPs and wash cell with

PBS once. Subsequently, detach cells from the culture dishes using Trypsin.

- Finally, collect cells by centrifugation at 190 × g for 4 min for ICP-MS analysis (ELAN DRC II, PerkinElmer). During the ICP-MS analysis, ammonia gas was used in the event of molecular ion interference problems.

2.3. Results and discussions

2.3.1. Preparation of MPNPs using hot injection and polyol method

Preparation of magnetic plasmonic nanoparticles. Figure 2.6 shows the synthetic procedure of magnetic plasmonic nanoparticles Ag/FeCo/Ag were prepared by combination of hot injection and polyol methods. At first, the reaction mixture containing Ag precursors, HDD, OLA and OA was heated to 100ºC for 10 min to from Ag nanoparticles. It is noted that the formation of Ag cores first is important because it acts as the catalyst to reduce Fe^{3+} and Co^{2+}. After that, the solution was heated to 170ºC before adding Fe and Co precursors. From the previous study, it was found that although the Fe, Co precursors were added at 170ºC, FeCo layer were not immediately formed.[18] The reason is that until the size of Ag core reached around 10 nm, then it could effectively show the catalytic activity. Therefore, during the second injection of Ag precursor at 250ºC, Ag cores was further growth to reach the critical size, followed by the formation of FeCo shell. Finally, due to the energetically favorable surface segregation, the Ag atoms were incorporated with FeCo shell to form a submonolayer Ag outer shell.[18]

Figure 2.7A shows a TEM image of as-synthesized MPNPs with the mean diameter of 14.7 ± 2.4 nm (n = 592). The size distribution of MPNPs was shown in Figure 2.7B. The UV-vis spectrum of MPNPs exhibited the LSPR peak derived from Ag core at 408 nm

(Figure 2.7C). The absorbance was used to estimate the concentration of MPNPs using the calibration curve with equation: y = 0.024x, where y is the maximum absorbance of LSPR peak and x is the concentration of MPNPs (μg/mL).[19] Figure 2.7D shows the magnetization curve of MPNPs measured by SQUID at 300K, which indicated the saturation magnetization of MPNPs was 40 emu/g.

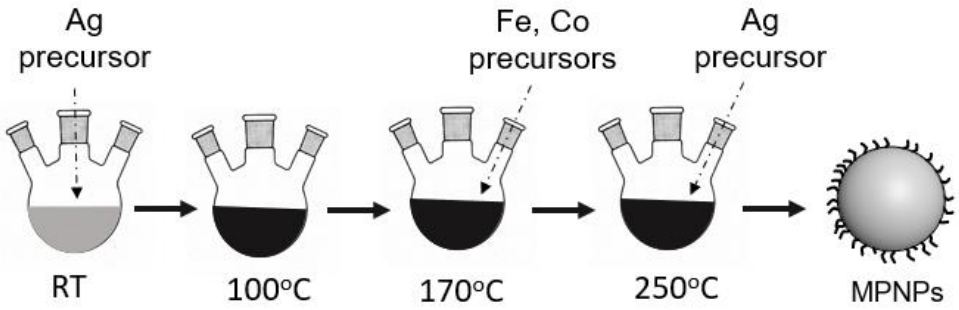

Figure 2.6: Schematic illustration of the synthesis of MPNPs.

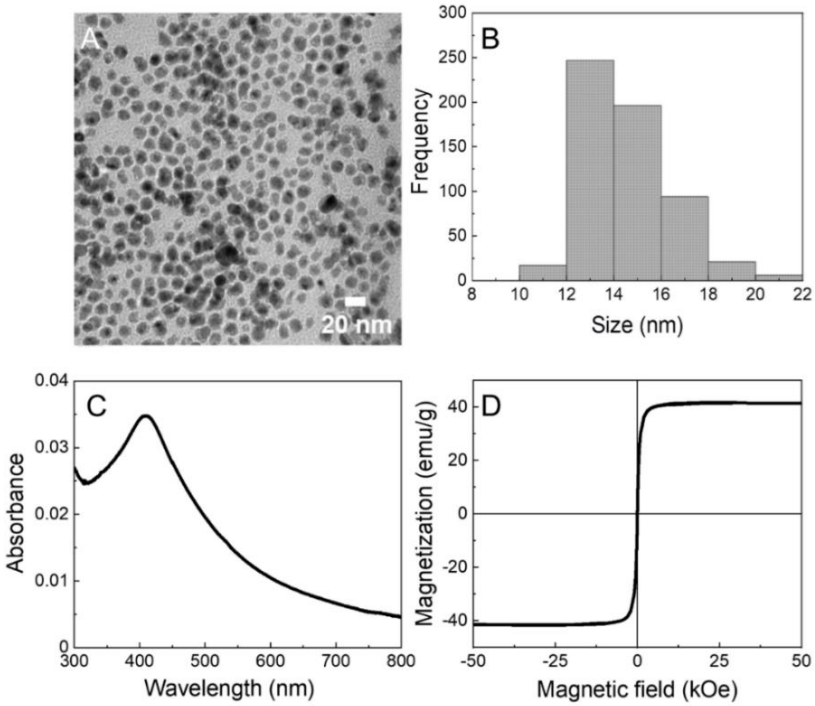

Figure 2.7: (A) TEM image, (B) size distribution, (C) UV-vis spectrum and (D) magnetization curve at 300K of as-prepared MPNPs.

2.3.2. Surface modification of MPNPs for targeting lysosomes

A schematic illustration of the preparation of aDxt-MPNPs is shown in Figure 2.8A. The as-synthesized MPNPs were covered with hydrophobic ligands with the hydrodynamic size (D_h) in hexane of 18.7 ± 1.9 nm (Figure 2.8B); thus, surface modification was required to deliver MPNPs to the lumen of lysosomes through endocytic pathways. The MPNPs were encapsulated in phospholipid micelles to make them water dispersible following the method of Dubertret et al.[20] with some modifications. Specifically, MPNPs were encapsulated in phospholipid micelles composed of N-glutaryl DOPE and PEG350-DOPE with the molar ratio of 3:2. Figure 2.8B shows the distribution of D_h of MPNPs in water after encapsulation with the mean D_h of 33.9 ± 1.8 nm. The increases in D_h indicated that MPNPs were successfully encapsulated in phospholipid micelles. Because no significant increase in D_h was observed, the majority of micelles were thought to contain only one MPNP. The zeta potential of MPNPs after the lipid encapsulation was determined to be −22.1 ± 2.6 mV (Figure 2.8C), which was primarily stemming from carboxylic group of N-glutaryl DOPE because the zeta potential of PEG chain is approximately 0 mV.[21] However, the PEG chain still contributes significantly to the colloidal stability of phospholipid-coated MPNPs by decreasing the attraction force between particles through steric hindrance and increasing the hydrophilic property via the formation of hydrogen bonds between solvent molecules and the ether units of PEG chains. In this study, aDxt molecules were covalently conjugated on the surface of the phospholipid-encapsulated MPNPs through the EDC coupling reaction between carboxylic groups in N-glutaryl DOPE and amino groups in aDxt. As shown in Figure 2.8C, the zeta potential clearly shifted from negative to positive after the aDxt conjugation

indicating that the surface of the phospholipid-encapsulated MPNPs was successfully covered with aDxt to form aDxt-MPNPs.

The D_h of aDxt-MPNPs in water (pH = 7) was measured to be 52.4 ± 7.8 nm (Figure 2.8B). The D_h of aDxt-MPNPs in the pH range of 4 to 10 exhibited no significant change (Figure 2.9) suggesting that the pH change would not affect the colloidal stability of aDxt-MPNPs.

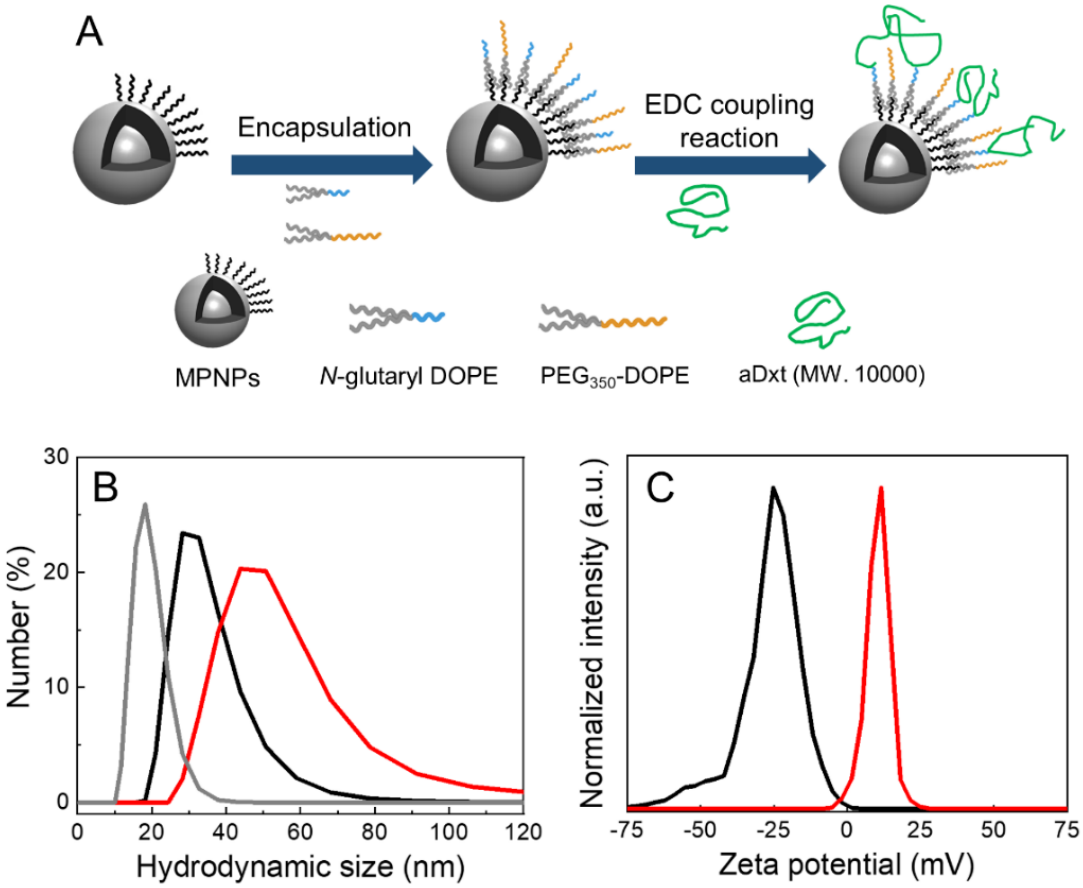

Figure 2.8: (A) The schematic illustration of aDxt-MPNPs preparation. (B) Hydrodynamic size distributions of MPNPs in hexane (gray), phospholipid-encapsulated MPNPs (black) and aDxt-MPNPs (red) in water. (C) Zeta potential of phospholipid-encapsulated MPNPs (black) and aDxt-MPNPs (red) in water.

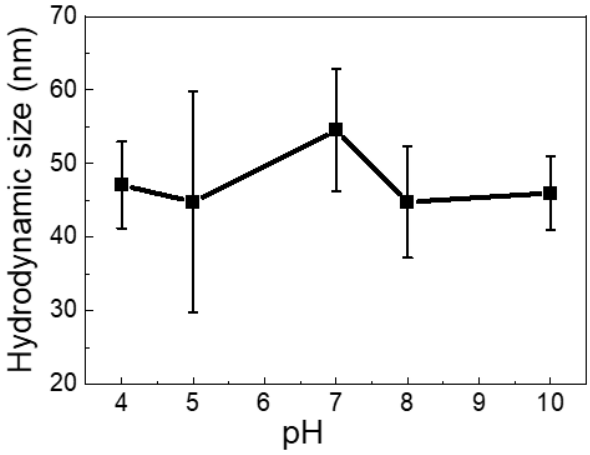

Figure 2.9: Hydrodynamic size of aDxt-MPNPs in different pH solution from 4 to 10.

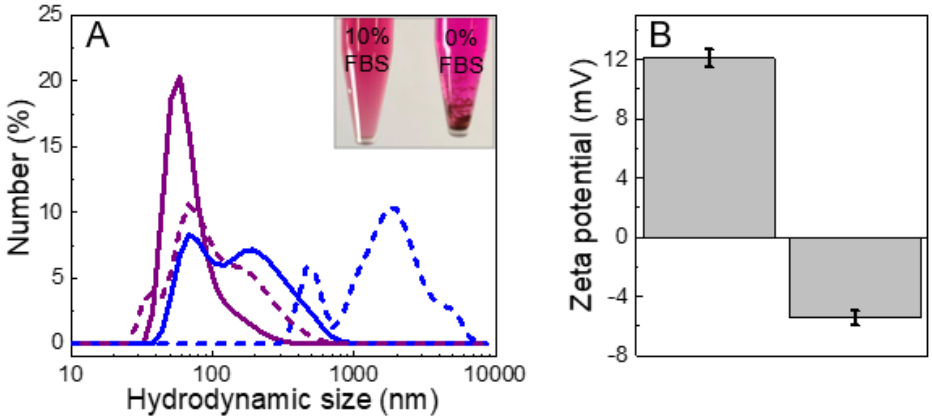

Figure 2.10: (A) Semilogarithmic plot of the hydrodynamic size distributions of aDxt-MPNPs in DMEM (+0% FBS) after 0 h (blue) and 24 h (dash blue), and in DMEM (+10% FBS) after 0 h (violet) and 24 h (dash violet); The inset shows the sedimentation of aDxt-MPNPs in DMEM (+0% FBS) after 24 h, while no such phenomena was observed in DMEM (+10% FBS). (B) zeta potential of aDxt-MPNPs in water and in DMEM (+ 10% FBS).

Figure 2.10A shows the D_h of aDxt-MPNPs in DMEM with (10%) or without (0%) FBS. The colloidal stability of aDxt-MPNPs in culture medium is important, because the aggregation of nanoparticles may generally hinder the cellular uptakes.[22] The D_h of aDxt-

MPNPs in DMEM (+10% FBS) was increased to 74.5 ± 8.2 nm, while the zeta potential was changed from +12 mV to −4.5 mV (Figure 2.10B). Those results suggested the adsorption of serum proteins on the surface of aDxt-MPNPs. After 24 h, the D_h increased to 123 ± 40 nm, presumably due to the lower surface charge. It has been reported that the dextran-coated SPIONs with size up to 200 nm were efficiently endocytosed by various types of cells.[23] On the contrary, the surface charge of aDxt-MPNPs was completely screened (~0 mV) by ions in the case of aDxt-MPNPs dispersed in DMEM (+0% FBS) leading to the immediate aggregation of aDxt-MPNPs resulting in the D_h of 185 ± 55 nm (Figure 2.10A). After 1 day, the Dh of aDxt-MPNPs reached to 1876 ± 755 nm, which causes the complete sedimentation of aDxt-MPNPs. Meanwhile, no such phenomena were observed in the case of aDxt-MPNPs dispersed in DMEM (+10% FBS) as shown in the inset of Figure 2.10A.

2.3.3. The cytotoxicity and cellular uptake of aDxt-MPNPs

The cytotoxicity of aDxt-MPNPs on COS-1 cell was assessed using the Cell Counting Kit-F. The incubation time of COS-1 cells in the presence of aDxt-MPNPs was called as t_{load} hereafter. Figure 2.11A shows the cell viability after incubation with aDxt-MPNPs with the concentration of C_{NPs} = 100 and 50 μg/mL in DMEM (+10% FBS). After t_{load} = 1 h, the cell viability was 80% in the case of C_{NPs} = 100 μg/mL, while no significant cytotoxicity was observed when C_{NPs} = 50 μg/mL. After t_{load} = 8h, the cell viability in both cases was ~ 75%. When the C_{NPs} was increased to 200 μg/mL, the cell viability was significantly reduced to 42% (Figure 2.11B). At C_{NPs} = 100 and 50 μg/mL, no significant cytotoxicity was observed even when the t_{load} was prolonged to 24 h. The cell viability was still ~ 75% for both cases.

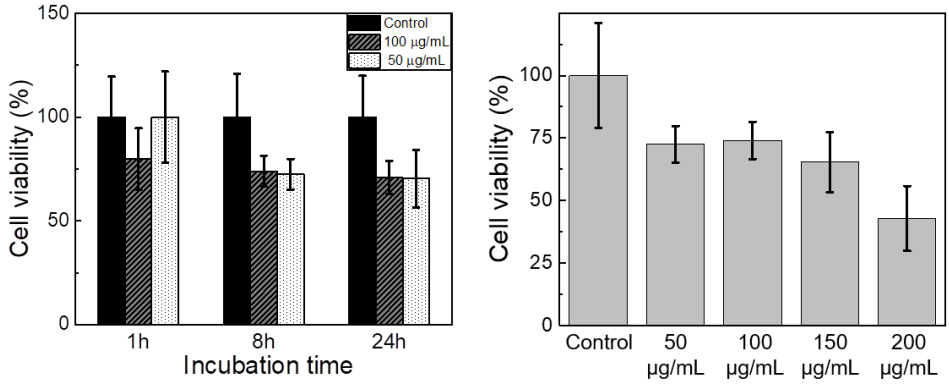

Figure 2.11: (A) Cell viability after incubation with aDxt-MPNPs at CNPs = 100 and 50 µg/mL for t_{load} = 1, 8 and 24 h in DMEM (+10% FBS). (B) The cell viability after incubation in DMEM (+10% FBS) containing different concentrations of aDxt-MPNPs with the t_{load} = 8 h.

Note that the aDxt-MPNPs showed a high cytotoxicity in the absence of FBS. The cell viability was reduced to ~ 30% when cells were incubated in DMEM (+0% FBS) with C_{NPs} = 100 µg/mL for t_{load} = 1 h, followed by the incubation in the fresh culture medium for 7 h (Figure 2.12). For this case, the cell viability was found to significantly increase with decreasing C_{NPs}. It is well-known that the electrostatic interaction between positively charged nanoparticles and negatively-charged cell membrane glycoproteins would be the reason for the high cytotoxicity. [24, 25] Therefore, the aDxt-MPNPs were dispersed in DMEM (+10% FBS) for 10 min before adding them to a cell dish to allow the formation of the protein corona.

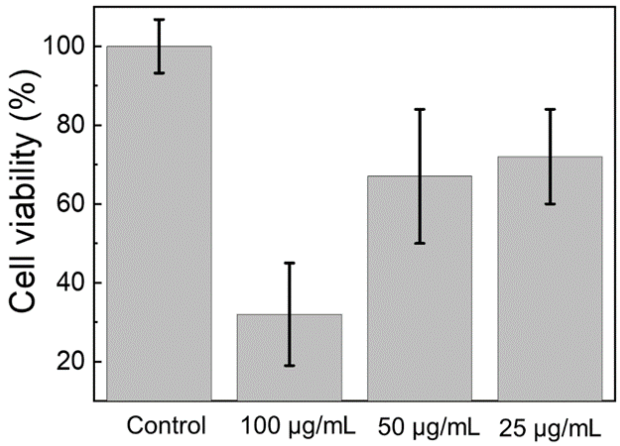

Figure 2.12: The cell viability after incubation in DMEM (+0% FBS) containing different concentrations of aDxt-MPNPs with the t_{load} = 1 h.

Generally, t_{load} strongly influences the isolation yield of lysosomes using magnetic nanoparticle-based fractionation method. Therefore, the dependence of cellular uptake on tload was investigated using inductively coupled plasma mass spectrometry (ICP-MS). As a result, the amounts of Co and Ag in cells were found to increase almost two-fold, when t_{load} was prolonged from 1 to 8 h (Figure 2.13A). The average size of Ag core in MPNPs is approximately 10 nm, while the thickness of outer Ag shell is negligible. [26, 27] Based on that information, the numbers of aDxt-MPNPs per cell after t_{load} = 1 and 8 h were calculated to be 3.4×10^5 and 6.1×10^5, respectively (Figure 2.13B). It is obvious that the longer t_{load} results in the higher particles uptake, which later affect to magnetic isolation yield.

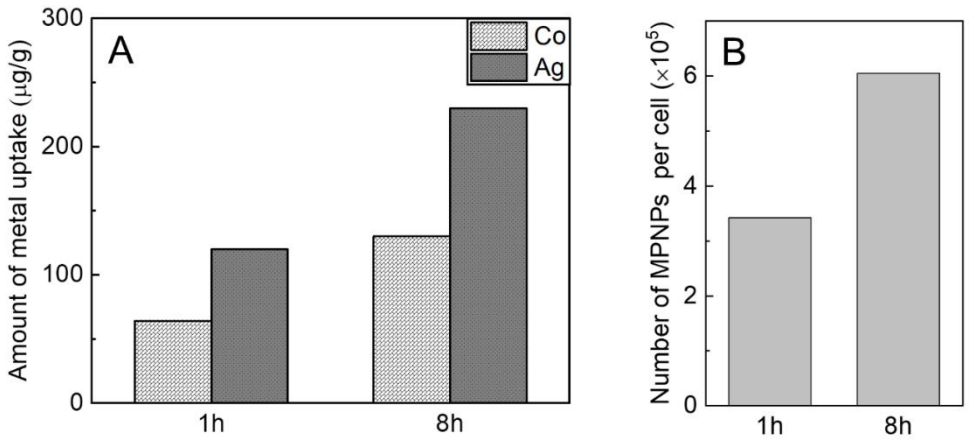

Figure 2.13: The cellular metal uptake was determined using ICP-MS. (A) The amount of Co and Ag accumulated in 4×10^6 COS-1 cells after 1 and 8 h, and (B) the estimated number of particles uptake per cell.

2.4. Conclusion

In this study, aDxt-MPNPs were prepared for targeting lysosome through the endo-lysosomal pathway. Specifically, the hydrophobic MPNPs were coated using lipid layers because of their inherent biocompatibility and ability to self-assemble into organized structures. The advantage of this technique is that the surface of MPNPs were not directly modified; therefore, aggregation could be avoided during encapsulation. It should be mentioned that the purpose of using phospholipid containing PEG-chain in this study is to enhance colloidal stability during EDC coupling reaction. A short PEG chain molecule was selected to avoid a drastic increase in D_h and the effect of its steric hinderance on the conjugation of aDxt. By employing this strategy, we could obtain highly stable hydrophilic MPNPs.

To deliver MPNPs to lysosomes, MPNPs were conjugated with dextran which has been extensively used for coating nanoparticles to target them to lysosomes.[28] In this study, aDxt was used to covalently cover the surfaces of the phospholipid-encapsulated MPNPs,

which resulted in the positively-charged aDxt-MPNPs. Compared to negatively-charged nanoparticles, the positively-charged nanoparticles generally show a higher level of cellular uptake,[29-31] while they exhibit higher cytotoxicity.[31, 32] Those tendencies were also observed in our case. To suppress the cytotoxicity of aDxt-MPNPs, the aDxt-MPNPs were dispersed in DMEM (+10% FBS) to form the protein corona on the surface of aDxt-MPNPs which can reduce the electrostatic interaction between aDxt-MPNPs and cell membrane, and thus enhance the cell viability. It is well known that the formation of protein corona may suppress the cellular uptake of nanoparticles due to the deactivation of the recognition of nanoparticles by cell receptors. However, it is also well known that dextran acts as a fluid phase cargo that is internalized via pinocytosis and/or phagocytosis rather than receptor-mediated endocytosis.[33-35] Hence, the cellular uptake of aDxt-MPNPs was still very high (i.e. the number of aDxt-MPNPs per cell was of the order of 10^5 according to the ICP-MS analysis).

The uptake quantity of magnetic nanoparticles directly influences the number of lysosomes isolated by magnetic fractionation method. In this study, the uptake quantity of aDxt-MPNPs could be precisely controlled by adjusting t_{load}. The ICP-MS analysis revealed that the uptake quantity of aDxt-MPNPs was almost two-fold when t_{load} = 8 h compared to that in the case of t_{load} = 1 h. Generally, it could be expected that the lower loading quantity of nanoparticles would reduce cytotoxicity on cells but lead to a low yield of lysosome isolation, while the higher loading quantity of nanoparticles would induce cellular stress but lead to a higher yield. Consequently, there exists a trade-off between cytotoxicity and isolation yield. In our study, the difference of the cell viability between t_{load} = 1 and 8 h was insignificant. For this reason, t_{load} = 8 h was set to get higher loading quantity of aDxt-MPNPs. To enhance the amount of particle uptake, the increase

in C_{NPs} during the loading process is another option, although the cytotoxicity may also increase with C_{NPs}, which will be problematic especially in the case of cells exhibiting a strong dose-dependent cytotoxicity. In our case, the cell viability remained unchanged when COS-1 cells are loaded with aDxt-MPNPs either C_{NPs} = 50 or 100 µg/mL for t_{load} = 8 h, while the cytotoxicity significantly increased when C_{NPs} = 200 µg/mL. It could be expected that the isolation yield of lysosomes strongly depends on the number of aDxt-MPNPs per cell, which could be enhanced by increasing t_{load} and C_{NPs}, compromising with the cytotoxicity. Based on the result of cytotoxicity and cellular uptake, C_{NPs} was fixed at 100 µg/mL for later experiments.

References

1. Lim, E. K.; Kim, T.; Paik, S.; Haam, S.; Huh, Y. M.; Lee, K., Nanomaterials for theranostics: recent advances and future challenges. *Chem Rev* **2015,** *115* (1), 327-94.

2. Patra, J. K.; Das, G.; Fraceto, L. F.; Campos, E. V. R.; Rodriguez-Torres, M. D. P.; Acosta-Torres, L. S.; Diaz-Torres, L. A.; Grillo, R.; Swamy, M. K.; Sharma, S.; Habtemariam, S.; Shin, H. S., Nano based drug delivery systems: recent developments and future prospects. *J Nanobiotechnology* **2018,** *16* (1), 71.

3. Han, X.; Xu, K.; Taratula, O.; Farsad, K., Applications of nanoparticles in biomedical imaging. *Nanoscale* **2019,** *11* (3), 799-819.

4. Wu, K.; Liu, J.; Saha, R.; Peng, C.; Su, D.; Wang, Y. A.; Wang, J. P., Investigation of Commercial Iron Oxide Nanoparticles: Structural and Magnetic Property Characterization. *Acs Omega* **2021,** *6* (9), 6274-6283.

5. Stueber, D. D.; Villanova, J.; Aponte, I.; Xiao, Z.; Colvin, V. L., Magnetic Nanoparticles in Biology and Medicine: Past, Present, and Future Trends. *Pharmaceutics* **2021,** *13* (7).

6. Kim, M.; Lee, J. H.; Nam, J. M., Plasmonic Photothermal Nanoparticles for Biomedical Applications. *Adv Sci (Weinh)* **2019,** *6* (17), 1900471.

7. Sarfraz, N.; Khan, I., Plasmonic Gold Nanoparticles (AuNPs): Properties, Synthesis and their Advanced Energy, Environmental and Biomedical Applications. *Chem Asian J* **2021,** *16* (7), 720-742.

8. van Sark, W. G. J. H. M.; Frederix, P. L. T. M.; Van den Heuvel, D. J.; Gerritsen, H. C.; Bol, A. A.; van Lingen, J. N. J.; de Mello Donegá, C.; Meijerink, A., Photooxidation and Photobleaching of Single CdSe/ZnS Quantum Dots Probed by Room-Temperature Time-Resolved Spectroscopy. *The Journal of Physical Chemistry B*

2001, *105* (35), 8281-8284.

9. Hardman, R., A toxicologic review of quantum dots: toxicity depends on physicochemical and environmental factors. *Environ Health Perspect* **2006,** *114* (2), 165-72.

10. Levin, C. S.; Hofmann, C.; Ali, T. A.; Kelly, A. T.; Morosan, E.; Nordlander, P.; Whitmire, K. H.; Halas, N. J., Magnetic-plasmonic core-shell nanoparticles. *ACS Nano* **2009,** *3* (6), 1379-88.

11. Wei, D. H.; Lin, T. K.; Liang, Y. C.; Chang, H. W., Formation and Application of Core-Shell of FePt-Au Magnetic-Plasmonic Nanoparticles. *Front Chem* **2021,** *9*, 653718.

12. Lin, L. S.; Yang, X.; Zhou, Z.; Yang, Z.; Jacobson, O.; Liu, Y.; Yang, A.; Niu, G.; Song, J.; Yang, H. H.; Chen, X., Yolk-Shell Nanostructure: An Ideal Architecture to Achieve Harmonious Integration of Magnetic-Plasmonic Hybrid Theranostic Platform. *Adv Mater* **2017,** *29* (21).

13. Zhang, Q.; Liu, Y.; Nie, Y.; Ma, Q., Magnetic-plasmonic yolk-shell nanostructure-based plasmon-enhanced electrochemiluminescence sensor. *Sensors and Actuators B: Chemical* **2020,** *319*, 128245.

14. Shams, S. F.; Ghazanfari, M. R.; Schmitz-Antoniak, C., Magnetic-Plasmonic Heterodimer Nanoparticles: Designing Contemporarily Features for Emerging Biomedical Diagnosis and Treatments. *Nanomaterials (Basel)* **2019,** *9* (1).

15. Zeng, J.; Gong, M.; Wang, D.; Li, M.; Xu, W.; Li, Z.; Li, S.; Zhang, D.; Yan, Z.; Yin, Y., Direct Synthesis of Water-Dispersible Magnetic/Plasmonic Heteronanostructures for Multimodality Biomedical Imaging. *Nano Lett* **2019,** *19* (5), 3011-3018.

16. Fievet, F.; Ammar-Merah, S.; Brayner, R.; Chau, F.; Giraud, M.; Mammeri, F.; Peron, J.; Piquemal, J. Y.; Sicard, L.; Viau, G., The polyol process: a

unique method for easy access to metal nanoparticles with tailored sizes, shapes and compositions. *Chem Soc Rev* **2018,** *47* (14), 5187-5233.

17. Takahashi, M.; Mohan, P.; Nakade, A.; Higashimine, K.; Mott, D.; Hamada, T.; Matsumura, K.; Taguchi, T.; Maenosono, S., Ag/FeCo/Ag core/shell/shell magnetic nanoparticles with plasmonic imaging capability. *Langmuir* **2015,** *31* (7), 2228-36.

18. Takahashi, M.; Higashimine, K.; Mohan, P.; Mott, D. M.; Maenosono, S., Formation mechanism of magnetic–plasmonic Ag@FeCo@Ag core–shell–shell nanoparticles: fact is more interesting than fiction. *CrystEngComm* **2015,** *17* (36), 6923-6929.

19. Takahashi, M.; Mohan, P.; Mukai, K.; Takeda, Y.; Matsumoto, T.; Matsumura, K.; Takakura, M.; Arai, H.; Taguchi, T.; Maenosono, S., Magnetic Separation of Autophagosomes from Mammalian Cells Using Magnetic-Plasmonic Hybrid Nanobeads. *Acs Omega* **2017,** *2* (8), 4929-4937.

20. Dubertret, B.; Skourides, P.; Norris, D. J.; Noireaux, V.; Brivanlou, A. H.; Libchaber, A., In vivo imaging of quantum dots encapsulated in phospholipid micelles. *Science* **2002,** *298* (5599), 1759-62.

21. Xu, Q. G.; Ensign, L. M.; Boylan, N. J.; Schon, A.; Gong, X. Q.; Yang, J. C.; Lamb, N. W.; Cai, S. T.; Yu, T.; Freire, E.; Hanes, J., Impact of Surface Polyethylene Glycol (PEG) Density on Biodegradable Nanoparticle Transport in Mucus ex Vivo and Distribution in Vivo. *Acs Nano* **2015,** *9* (9), 9217-9227.

22. Alkilany, A. M.; Mahmoud, N. N.; Hashemi, F.; Hajipour, M. J.; Farvadi, F.; Mahmoudi, M., Misinterpretation in Nanotoxicology: A Personal Perspective. *Chem Res Toxicol* **2016,** *29* (6), 943-8.

23. Uzhytchak, M.; Smolkova, B.; Lunova, M.; Jirsa, M.; Frtus, A.; Kubinova, S.; Dejneka, A.; Lunov, O., Iron Oxide Nanoparticle-Induced Autophagic

Flux Is Regulated by Interplay between p53-mTOR Axis and Bcl-2 Signaling in Hepatic Cells. *Cells* **2020,** *9* (4).

24. Sukhanova, A.; Bozrova, S.; Sokolov, P.; Berestovoy, M.; Karaulov, A.; Nabiev, I., Dependence of Nanoparticle Toxicity on Their Physical and Chemical Properties. *Nanoscale Res Lett* **2018,** *13* (1), 44.

25. Huhn, D.; Kantner, K.; Geidel, C.; Brandholt, S.; De Cock, I.; Soenen, S. J.; Rivera Gil, P.; Montenegro, J. M.; Braeckmans, K.; Mullen, K.; Nienhaus, G. U.; Klapper, M.; Parak, W. J., Polymer-coated nanoparticles interacting with proteins and cells: focusing on the sign of the net charge. *Acs Nano* **2013,** *7* (4), 3253-63.

26. Takahashi, M.; Higashimine, K.; Mohan, P.; Mott, D. M.; Maenosono, S., Formation mechanism of magnetic-plasmonic Ag@FeCo@Ag core-shell-shell nanoparticles: fact is more interesting than fiction. *Crystengcomm* **2015,** *17* (36), 6923-6929.

27. Takahashi, M.; Mohan, P.; Nakade, A.; Higashimine, K.; Mott, D.; Hamada, T.; Matsumura, K.; Taguchi, T.; Maenosono, S., Ag/FeCo/Ag Core/Shell/Shell Magnetic Nanoparticles with Plasmonic Imaging Capability. *Langmuir* **2015,** *31* (7), 2228-2236.

28. Hong, R. Y.; Feng, B.; Chen, L. L.; Liu, G. H.; Li, H. Z.; Zheng, Y.; Wei, D. G., Synthesis, characterization and MRI application of dextran-coated Fe3O4 magnetic nanoparticles. *Biochemical Engineering Journal* **2008,** *42* (3), 290-300.

29. Rancan, F.; Gao, Q.; Graf, C.; Troppens, S.; Hadam, S.; Hackbarth, S.; Kembuan, C.; Blume-Peytavi, U.; Ruhl, E.; Lademann, J.; Vogt, A., Skin penetration and cellular uptake of amorphous silica nanoparticles with variable size, surface functionalization, and colloidal stability. *Acs Nano* **2012,** *6* (8), 6829-42.

30. Panariti, A.; Miserocchi, G.; Rivolta, I., The effect of nanoparticle uptake on cellular behavior: disrupting or enabling functions? *Nanotechnol Sci Appl* **2012,** *5*, 87-

100.

31. Bannunah, A. M.; Vllasaliu, D.; Lord, J.; Stolnik, S., Mechanisms of nanoparticle internalization and transport across an intestinal epithelial cell model: effect of size and surface charge. *Mol Pharm* **2014,** *11* (12), 4363-73.

32. Liu, Y.; Li, W.; Lao, F.; Liu, Y.; Wang, L.; Bai, R.; Zhao, Y.; Chen, C., Intracellular dynamics of cationic and anionic polystyrene nanoparticles without direct interaction with mitotic spindle and chromosomes. *Biomaterials* **2011,** *32* (32), 8291-303.

33. Hacker, U.; Albrecht, R.; Maniak, M., Fluid-phase uptake by macropinocytosis in Dictyostelium. *J Cell Sci* **1997,** *110*, 105-112.

34. Murphy, R. F., Analysis and isolation of endocytic vesicles by flow cytometry and sorting: demonstration of three kinetically distinct compartments involved in fluid-phase endocytosis. *Proc Natl Acad Sci U S A* **1985,** *82* (24), 8523-6.

35. Guggenheim, E. J.; Rappoport, J. Z.; Lynch, I., Mechanisms for cellular uptake of nanosized clinical MRI contrast agents. *Nanotoxicology* **2020,** *14* (4), 504-532.

Chapter 3: Intracellular trafficking study of MPNPs in COS-1

3.1. Introduction

Understanding of the bio-nano interaction is an important research field in bionanotechnology. Given that nanoparticles must pass through various biological barriers before reaching the target sites where they exert their functions.[1] Firstly, nanoparticles are required to overcome extracellular barriers, in which their colloidal stability in biological medium is a major issue. Following this, the nanoparticles must undergo cellular uptakes by their target cells. Of note, the number of particles uptakes which depends on physicochemical properties of nanoparticles and characteristic of cell-lines is a deterministic factor affecting nanoparticle efficacy. Furthermore, even after the efficient internalization, other aspects related to the intracellular distribution, kinetic transport are the major quests to decide the performance of nanoparticles in biological applications.[2, 3] Addressing these challenges are the important research area in bionanotechnology to maximize the performance of nanoparticles in each application. In the context of this thesis, we focus on the visualization of the trafficking of nanoparticles at subcellular levels.

The commonly used methods for visualizing the intracellular trafficking of nanoparticles include fluorescent- and electron-based microscopy techniques, which provide the quantitative image of the location nanoparticles within cells. Electron microscopy is a high throughput imaging platform that could obtain high resolution image of nanoparticles at subcellular level. However, the sample preparation is laborious and multistep process.[4] In addition, the field of view of electron microscopy technique is often

narrow, which is a challenge to obtain the quantitative estimation of nanoparticles in large number of cells. In contrast, the fluorescence microscopy technique could easily screen multiple cells at once, which provide more general picture of nanoparticles at cellular levels. However, asides from the photobleaching problems, nanoparticles are required to be labeled with fluorescent dyes for observation by fluorescent microscopy. The surface modification may influence the nano-bio interactions, which results in the alteration of the cellular uptake and intracellular trafficking of nanoparticles [5, 6] Because these parameters strongly depend on nanoparticles's physicochemical properties including shape, size and surface chemistry. Furthermore, if the lysosomes are the target sites, lysosomal environment could lead to quenching and/or distortion of fluorescence signals of dye, which cause an ensuing effect on the data interpretation.[7] Therefore, developing a nanoparticles with intrinsic imaging capability is of interest to obtain the intracellular trafficking information of nanoparticles before ultilizing them for certain applications.

Unlike small molecules that could pass through cell membrane using either active transport or passive diffusion mechanism, nanoparticles enter cells via three energy-dependent pathways including clathrin-dependent endocytosis, caveolae-dependent endocytosis and micropinocytosis,[8-10] in which they are confined in a membrane-bound vesicles and transported to various intracellular destinations. These vesicles travel throughout the cell in complex trafficking patterns. Once nanoparticles enter cells, it is challenging to depict a complete picture of all intracellular processes that occur. Consequently, establishing a kinetic model for describing the intracellular trafficking is a difficult task.

In this thesis work, magnetic nanoparticles are delivered to lysosomal lumens to label

lysosomes for magnetic separation as they are the destination of the endocytic pathway. Therefore, the accurate understanding of intracellular trafficking of magnetic nanoparticles is a key step to prevent contamination by other organelles (i.e. endosomes). As mentioned in chapter 2, we prepared MPNPs as the dual-functional probe for both imaging and magnetic separation. Owing to plasmonic property, these nanoparticles could be monitored using plasmonic scattering without requiring additional flourescent dye conjugation. By determining the colocalization of MPNPs with the staining organelles over time, the trafficking of nanoparticles inside the cell model could be derived. Additionally, we also proposed a simple mathematic model using stretched exponential function to determine the time constant which implies how fast nanoparticles translocate to certain organelles along the endocytic pathway.

3.2. Experiments

3.2.1. Chemicals

Table 3.1: List of the chemicals, their chemical formula or abbreviation

Chemicals	Formula/Abbreviation	Sources
PBS buffer solution		Prepared in chapter 2
Dulbecco's modified Eagle's medium	DMEM	Nacalai Tesque
CELLect® Fetal bovine serum	FBS	MP Biomedicals
African green monkey kidney fibroblast-like cell	COS-1	
Poly-L-lysine solution, 0.01%	PLL	Sigma-Aldrich
4%-paraformaldehyde phosphate buffer	PFA	Nacalai Tesque
*Digitonin	$C_{56}H_{92}O_{29}$	Wako Pure Chemical
*Ammonium chloride	NH_4Cl	Wako Pure Chemical
*Bovine serum albumin	BSA	Sigma-Aldrich
Alexa Fluor® 647 mouse anti-human CD107A	AF647@CD107A	BD Biosciences
*4',6-diamidino-2-phenylindole	DAPI	Thermo Fisher Scientific
VECTASHIELD® Antifade mounting medium		Vector Laboratories

** See recipes*

All chemicals are stored at 4ºC.

❖ **Recipes:**

1. Digitonin solution

Dissolve 25 mg of digitonin in 500 µL of dimethyl sulfoxide (DMSO). Divide solution into microtubes at 15 µL/tube. Store the solution at -20°C. It is diluted with PBS for

permeabilization

2. Ammonium chloride solution

Dissolve 0.160 g NH_4Cl in 60 mL of PBS buffer. Store the solution at 4°C.

3. DAPI staining solution

From commercial product, prepare the DAPI stock solution with a concentration of 100 μg/mL, store in refrigerator at 4°C. For nucleus staining, dilute the stock solution 2000 times further.

3.2.2. Pulse-chase experiments for studying intracellular trafficking of MPNPs

- Place 10-20 sterilized round cover glasses into a 10-cm culture dish.
- Add 5 mL of 0.01% PLL solution into the 10-cm dish and dip the round cover glasses in PLL solution at RT for 5 min using a tweezer.
- Remove PLL solution, cover with aluminum foil with the foil partially opened, and naturally dry overnight in the clean bench.
- The next day, wash the PLL coated cover glasses using 5 mL of PBS buffer three times.
- Place the 4 cover glasses in each well of 24-well plate using a tweezer, which correspond to different t_{chase} values of 1 h, 2 h, 4 h, and 7 h.

Note: The number of cover glasses increases according to the number of investigated t_{chase}. In the case of COS-1 cells, the maximum t_{chase} was performed at 7 h. However, it should be noted that the length of t_{chase} depends on different cell lines. Therefore, the incubation time of this experiment could be customized easily.

- Seed 20,000 COS-1 cells/well and incubate overnight in DMEM (+10% FBS) at 37 ºC under 5% CO_2.

- Check the health and confluency of cells under a bright-field microscope (Keyence, model: BZ-X810) in advance.
- The next day, remove the culture medium and wash cells with 500 µL of PBS at RT.
- For cell starvation, add 0.5 mL of pre-warmed DMEM without FBS and incubate for 30 min at 37 ºC under 5% CO_2.
- About 10 min before finishing the starvation process, add MPNPs to DMEM (+10% FBS) to prepare a dispersion of MPNPs with the concentration of 100 µg/mL.
- Immediately after starvation, replace DMEM without FBS with 500 µL of MPNPs dispersion in DMEM (+10% FBS) (prepared in step 10) and incubate for t_{load} = 1 h at 37ºC under 5% CO_2.
- After 1 h incubation, remove the dispersion and wash with 500 µL of PBS once. Then, add 500 µL of pre-warmed DMEM (+10% FBS) and incubate for t_{chase}: 0 h, 2 h, 4 h, and 7 h at 37 ºC under 5% CO_2.

Note: The t_{chase} would be varied in different cell lines. Therefore, the incubation period could be customized appropriately.

- After completing the t_{chase}, wash with 500 µL of PBS three times and add 500 µL of 4% PFA to each well for 15 min at RT.

Note: The following steps could be performed outside the clean bench. The sterile conditions are not required.

- Wash with 500 µL of PBS three times, add 500 µL of 50 µg/mL digitonin-PBS for permeabilization to each well and wait for 5 min.
- Wash with 500 µL of PBS three times, add 500 µL of 50 mM NH_4Cl-PBS to each well and wait for 10 min.
- Wash with 500 µL of PBS three times and blocking is performed by adding 500 µL of 3 wt% BSA-PBS to each well and waiting for 30 min.

- For each well, add 500 μL of 3 wt% BSA-PBS containing 2 μL of AF647@CD107A for staining the lysosomes and 0.25 μL of 100 μg/mL DAPI for staining the nuclei. Wait for 1 h at RT or keep it at 4°C for overnight.
- Wash with 500 μL of PBS three times. For each washing step, wait for 5 min after adding PBS.
- Add a drop of antifade mounting medium onto a white slide glass edge grinding and carefully take the cover glass using tweezers and place it onto the glass substrate for observation with the cell-facing surface in contact with the mounting medium. Ensure there are no bubbles and remove extra fluid if necessary.
- Leave it in a dark place for several hours until it is completely dry. Then, observe the samples using a CLSM.

3.2.3. Observation of MPNPs-loaded cells under CLSM

- Select 405, 473, and 635 nm lasers for the excitation of DAPI, aDxt-MPNPs, and AF647, respectively.
- For DAPI dye, select barrier filter (BA) 435-455 nm.
- For plasmonic scattering signal of aDxt-MPNPs, select no barrier filter. Because, unlike the fluorescent dye, the scattering signal from aDxt-MPNPs has the same wavelength as the laser wavelength.
- For AF647 dye, select BA 655-755 nm.
- Capture CLSM images of more than five different randomly-selected regions. Record DAPI signal separately to plasmonic scattering signal and fluorescence of AF647
- Perform colocalization analysis of aDxt-MPNPs and lysosomes by determining the

threshold Manders' colocalization coefficient (R_t) using ImageJ software.

3.2.4. Sample preparation for TEM observation of aDxt-MPNPs incorporated lysosomes

- Seed 550,000 COS-1 cells in 10 cm-dish and incubate overnight in DMEM (+10% FBS) at 37°C under 5% CO_2.
- The next day, remove the culture medium, and wash cells with 5 mL of PBS at RT.
- For cell starvation, add 5 mL of pre-warmed DMEM without FBS, and incubate for 30 min at 37°C under 5% CO_2.
- Approximately 10 min before finishing the starvation process, add MPNPs to DMEM (+10% FBS), to prepare a dispersion of MPNPs with the concentration of 100 μg/mL.
- Immediately after starvation, replace DMEM without FBS with 5 mL of MPNPs dispersion in DMEM (+10% FBS), and incubate for t_{load} = 1 h at 37°C under 5% CO_2.
- After 1 h incubation, remove the dispersion, and wash with 5 mL of PBS once. Then, add 5 mL of pre-warmed DMEM (+10% FBS), and incubate for t_{chase} = 7 h at 37°C under 5% CO_2.
- After completing the t_{chase}, wash with 5 mL of PBS three times. For fixation, add phosphate-buffered 2% glutaraldehyde for 10 min at RT and then 20 min at 4°C. subsequently, postfix cells in 2% osmium tetra-oxide for 3 h in an ice bath, followed by dehydration in ethanol before being embedded in epoxy resin.
- For TEM sampling, cut an ultrathin section by an ultramicrotome technique.
- Stain TEM sample with uranyl acetate for 10 min and lead-staining solution for 5 min before TEM observation (JEM-1200 EX, JEOL).

3.3. Results and discussions

3.3.1. Observation of intracellular trafficking using CLSM

The pulse-chase experiment was performed to investigate the intracellular trafficking of aDxt-MPNPs. Typically, in the pulse-chase experiment, cells are loaded with nanoparticles for a certain t_{load}. After the loading process, the excess nanoparticles which remain unincorporated into cells are removed. The cells are then incubated in fresh culture medium for a given period of time, t_{chase}, to chase the transport of nanoparticles within cells. In this study, COS-1 cells were loaded with aDxt-MPNPs for t_{load} = 1 h and subsequently chased in fresh culture medium varying tchase from 1 to 7 h. The total incubation time was denoted as $t = t_{load} + t_{chase}$. A colocalization analysis technique was employed to study the intracellular trafficking of endocytosed aDxt-MPNPs.

The schematic illustration of the transport of aDxt-MPNPs in a cell via non-specific uptake by fluid-phase endocytosis is shown in Figure 3.1. The aDxt-MPNPs are first transferred to early endosome and eventually reach lysosome through late endosome. To visualize this intracellular transport process, time-lapse monitoring of colocalization of aDxt-MPNPs with VPS26 (an early endosomal marker protein), Rab7 (a late endosomal marker protein) or LAMP1 (a lysosomal marker protein) was carried out. The laser and filter setup used CLSM observation is shown in Figure 3.2. To detect plasmon scattering signal of aDxt-MPNPs, 473 nm-laser wavelength was used to irradiate samples. For image acquisition, the appropriate band-pass filters were applied in channel 1 and 3 for collecting signals from DAPI and Alex flour 647, while the plasmonic scattering from the NPs was directly collected by channel 2. From the emission spectrum of DAPI dye, it

could be expected that the contaminated signals were significantly produced to channel 2, but had a minor effect on the channel 3. Meanwhile, the excitation and emission spectra of AF647 was well-separated from channel 2. Thus, the remaining concern was to eliminate the possible cross-talk signals from DAPI. Regarding this, the laser line with the wavelength of 405 nm for DAPI excitation was turned off during image acquisition of channel 2 and 3.

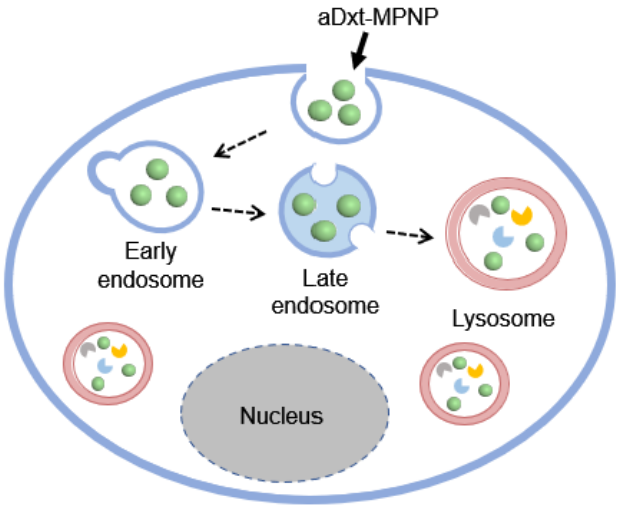

Figure 3.1: Illustration of intracellular trafficking of aDxt-MPNPs in COS-1 cells.

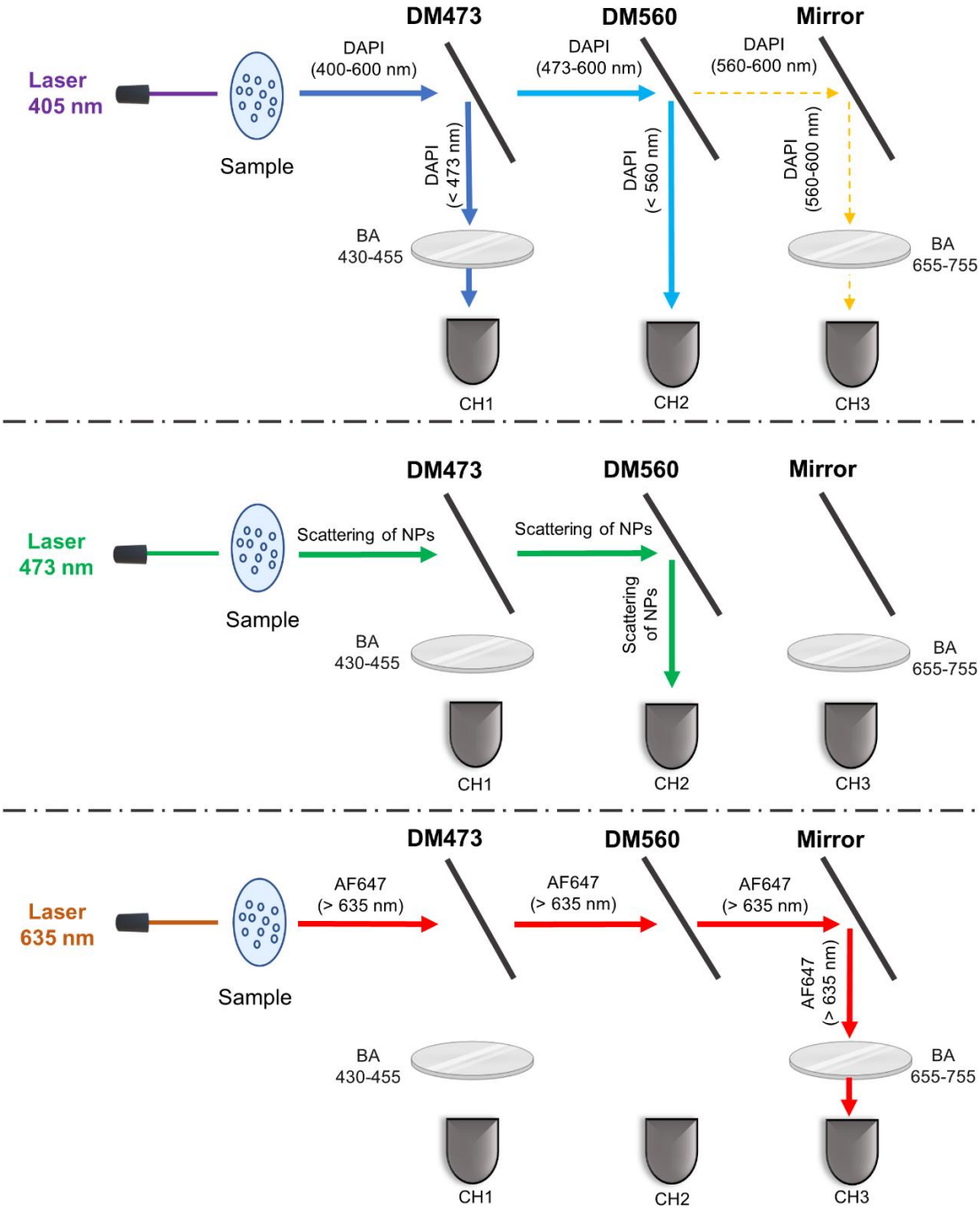

Figure 3.2: Optical setup of confocal laser scanning microscope.

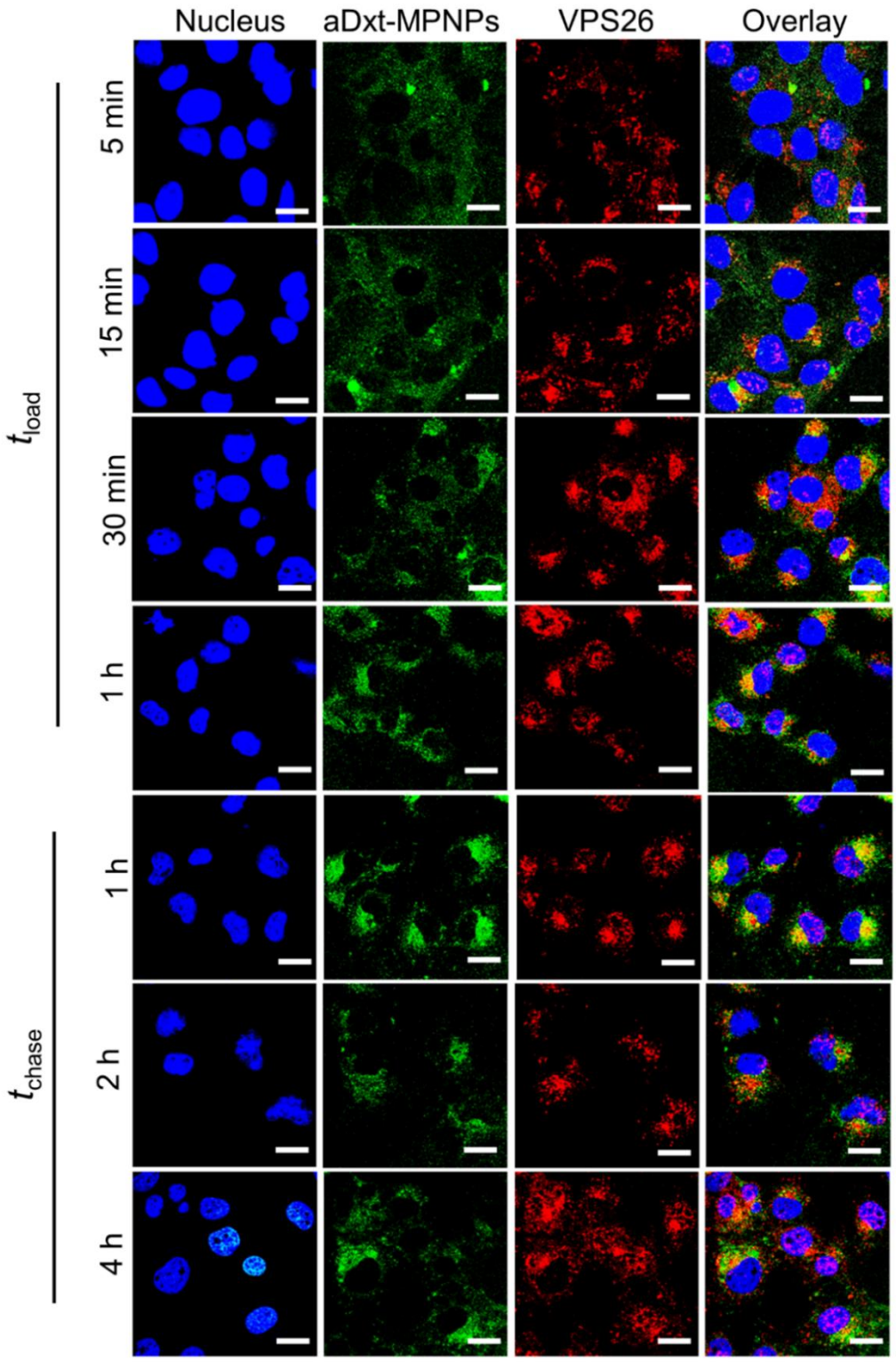

Figure 3.3: CLSM images showing the colocalization of aDxt-MPNPs with VPS26 over time. (Nucleus: blue, aDxt-MPNPs: green, EE: red). Scale bar is 20 µm.

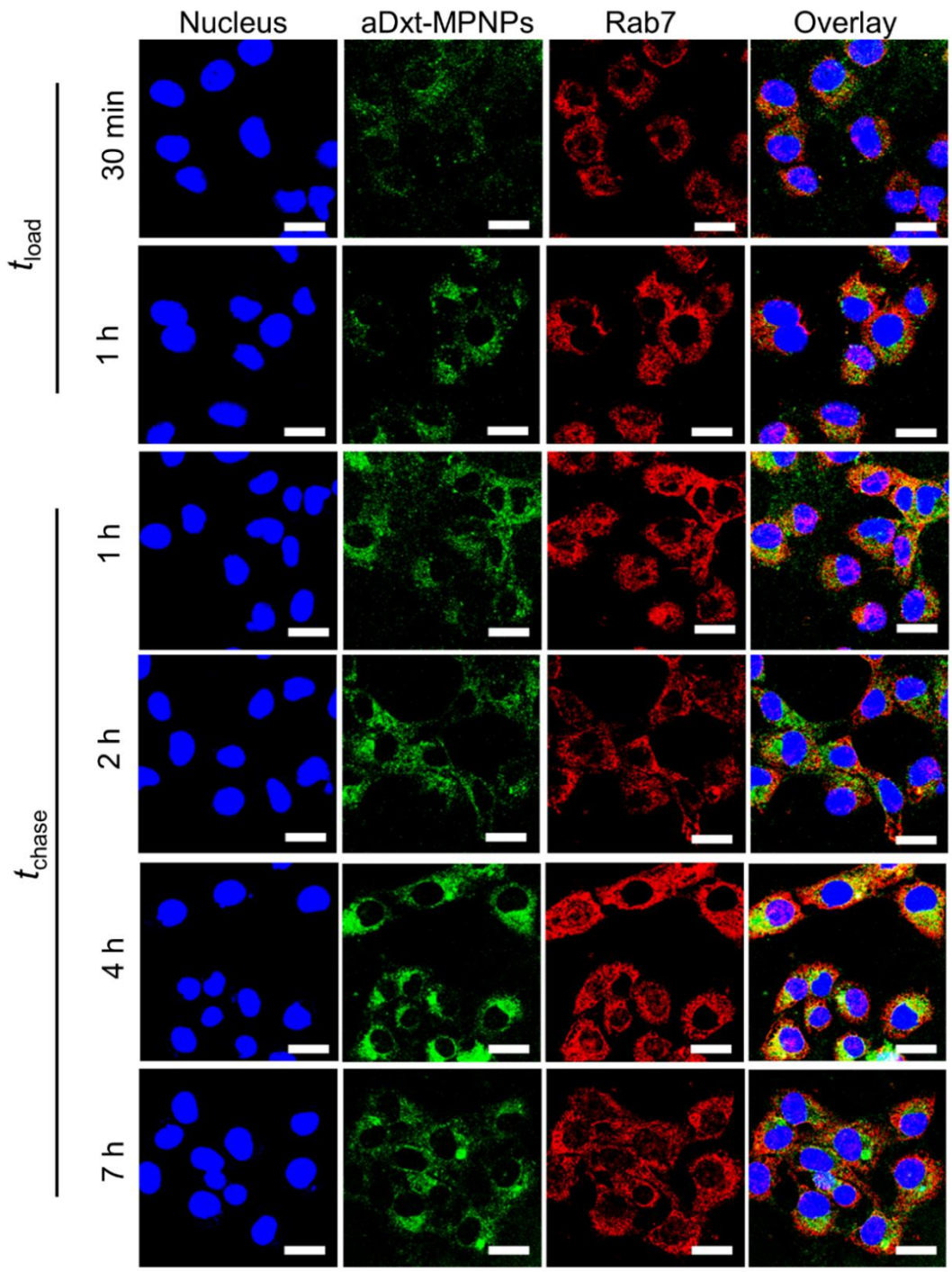

Figure 3.4: CLSM images showing the colocalization of aDxt-MPNPs with Rab7 over time. (Nucleus: blue, aDxt-MPNPs: green, LE: red). Scale bar is 20 µm.

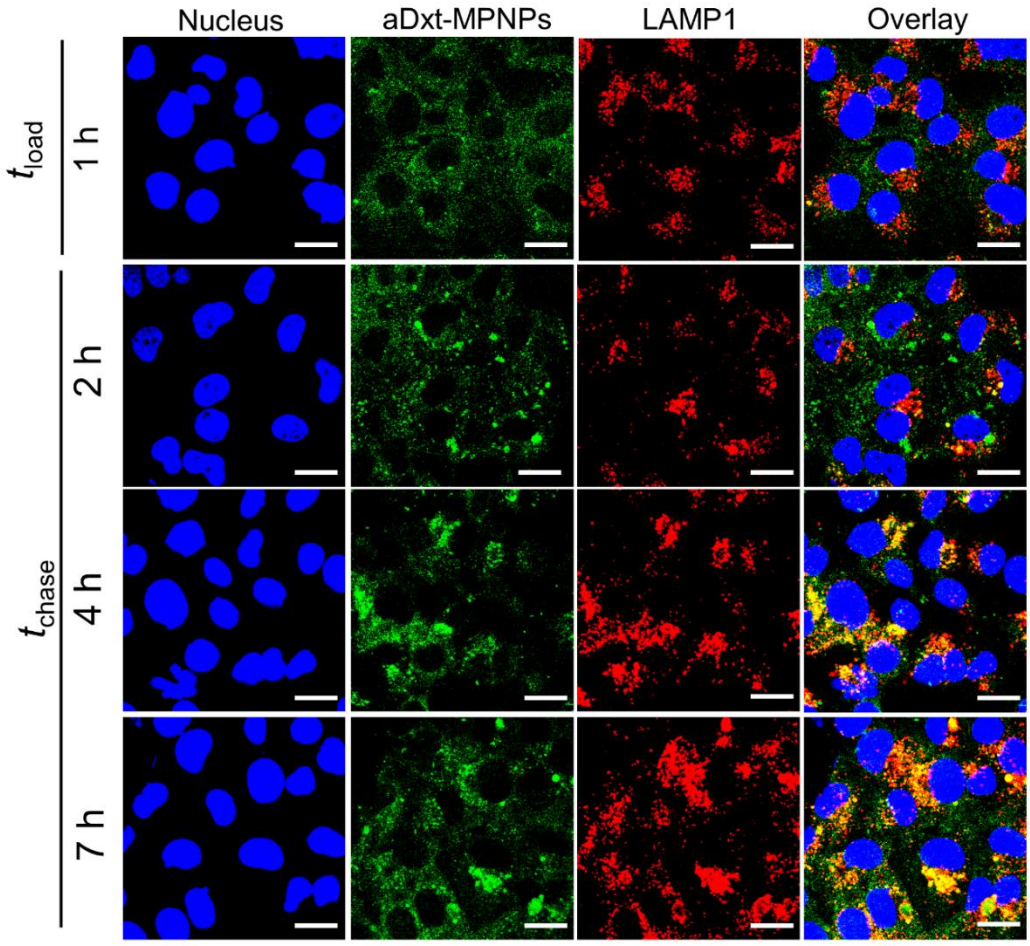

Figure 3.5: CLSM images showing colocalization of aDxt-MPNPs with LAMP1 (Nucleus: blue, aDxt-MPNPs: green, L: red). After t_{chase} = 4 h and 7 h, the colocalization of aDxt-MPNPs with LAMP-1 is clearly observed. Scale bar is 20 μm.

Figures 3.3, 3.4 and 3.5 show the time evolution colocalization of aDxt-MPNPs with EE, LE and L, respectively. From CLSM images, the intracellular trafficking of aDxt-MPNPs in COS-1 cells was roughly estimated. Given that the total incubation time $t = t_{load} + t_{chase}$, it takes t = 2 h, 5 h and 8h for aDxt-MPNPs to reach EE, LE and L, respectively. To quantify the degree of colocalization of aDxt-MPNPs with each organelle, those color images were segmented using ImageJ color clustering plugin with k means algorithm.[11] Following this, the threshold Manders' coefficient (R_t) represented the percentage of

organelles overlapped with aDxt-MPNPs was calculated using ImageJ with Coloc 2 plugin.

3.3.2. The transport kinetics of MPNPs in COS-1

Figure 3.3 shows the time-dependent colocalization of aDxt-MPNPs with VPS26. During loading of aDxt-MPNPs ($t_{load} \leq 1$ h), the accumulation of aDxt-MPNPs in EE lead to the increase of R_t (Figure 3.6A). The colocalization of aDxt-MPNPs with VPS26 was clearly visualized after 1 h of chasing ($t = 2$ h) (Figure 3.3), and R_t reached a maximum as shown in Figure 3.5B. When $t > 2$ h, R_t decreased suggesting that the aDxt-MPNPs were transported to the next destination. Figure 3.4 shows the time-lapse imaging of aDxt-MPNPs in LE. During loading ($t \leq 1$ h), the colocalization of aDxt-MPNPs with Rab7 was not significant ($R_t \approx 0.1$) as shown in Figure 3.6B. At $t = 5$ h, R_t reached a maximum, then it started to decrease when t > 5 h (Figure 3.6B). Figure 3.5B shows the time-variation colocalization of aDxt-MPNPs with LAMP1. When $t \leq 3$ h ($t_{chase} \leq 2$ h), the colocalization of aDxt-MPNPs with LAMP1 was not significant indicating that aDxt-MPNPs were mainly distributed in endosomal compartments as previously reported. [12] When $t = 5$ h ($t_{chase} = 4$ h), the colocalization of aDxt-MPNPs with LAMP1 became clear as shown in Figure 3.5B. The R_t value reached the plateau and became saturated when $t \geq 5$ h (Figure 3.6C). The further accumulation of aDxt-MPNPs could not be detected via the R_t value presumably due to the limited spatial resolution of CLSM imaging. Nevertheless, the decrease in R_t for the case of LE (Figure 3.6B) together with the saturation of R_t for the case of L when $t \geq 5$ h, which clearly confirmed that aDxt-MPNPs were transported from LE to L during $t \geq 5$ h and L is the final destination.

Of course, as many realize, the R_t value could be affected by random coincidences between green (aDxt-MPNPs) and red (organelles) pixels. To confirm the degree of influence of random coincidences on the R_t value, we calculated the R_t values between the reconstructed images for aDxt-MPNPs which were generated by randomly shuffling all pixels and the original images for organelle markers as shown in Figure 3.6A-C. The result clearly revealed the following two facts: first, the R_t values had no time variation and, second, the average R_t values were always less than 0.1 for all types of organelles which is negligibly small compared to the actual R_t values.

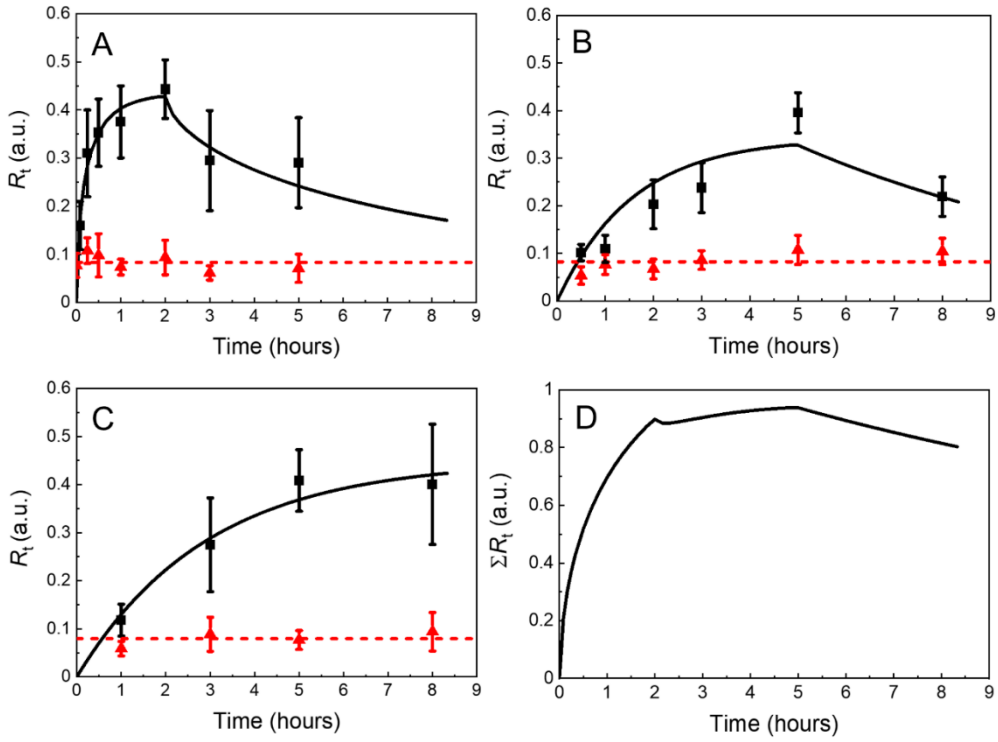

Figure 3.6: Threshold Mander's coefficient (R_t) for aDxt-MPNPs and different organelle marker proteins over time: (A) VPS26 (EE marker), (B) Rab7 (LE marker), and (C) LAMP1 (L marker). Red triangles represent the R_t values calculated between the reconstructed images for aDxt-MPNPs which were generated by randomly shuffling all pixels and the original images for organelle markers, and the red dashed lines are the average values of them. (D) Time variation of $\sum R_t$.

To confirm that aDxt-MPNPs mainly follows the endo-lysosomal pathway, and that endosomal escape did not take place, the time evolutions of R_t were fitted using a stretched-exponential function (Equations 1 and 2) for each dataset in Figure 3.6A-C.

$$R_t = A\left[1 - e^{-(t/\tau_1)^{\alpha}}\right] \quad (t \le t^*) \tag{1}$$

$$R_t = Be^{-[(t-t^*)/\tau_2]^{\beta}} \quad (t > t^*) \tag{2}$$

where A and B are constants, τ_1 and τ_2 are the characteristic time constants for the accumulation and decumulation, respectively, α and β are the stretching exponents, t^* is the time when the accumulation reached a maximum and the decumulation process became dominant.

Table 3.2: Fitting parameters of colocalization data using stretched-exponential functions

	Accumulation			Relaxation			
	A	α	τ_1 (min)	B	β	τ_2 (min)	t^*
EE	0.49	0.40	20	0.43	0.75	468	120
LE	0.34	0.76	71	0.33	0.64	442	300
L	0.45	0.63	110				

As seen in Figure 3.6A-C, the fitted curves using Equations (1) and (2) agree reasonably well with experimental data. The value of each parameter is shown in Table 3.2. The values of τ_1 for EE, LE and L were determined to be 20, 71 and 110 min, respectively. Remember that τ_1 is a time constant implies the speed with which nanoparticles are transported to a specific organelle; this is strongly dependent on cell type, nanoparticle properties, incubation conditions, etc. It should be emphasized that while the intracellular trafficking of nanoparticles could be monitored by various microscopy techniques, it is

quite challenging to develop a general kinetic model describing the transport process because of the complexity of the nanoparticle-cell interactions. For comparison, τ_1 for EE, LE and L were also determined in similar fashion for the case of DNA-decorated gold nanoparticles in HeLa cells (based on Figure 2i in Ref. 12). As a result, the values of τ_1 for EE, LE and L were derived to be 27, 33 and 250 min, respectively. Even though the absolute values of τ_1 differ from those of our case because the transport kinetics depend on various conditions as mentioned above, the universal behavior was confirmed regardless of type of organelle by plotting R_t/A vs t/τ_1 as shown in Figure 3.7. As shown in the inset of Figure 3.7D, scale invariance was observed [$R_t/A \propto (t/\tau_1)^{0.5}$] indicating that the physical law governing the transport processes is invariant.

Assuming the numbers of EE, LE and L are approximately the same in a cell and remain unchanged during incubation,[13] the relative amount of aDxt-MPNPs in the endo-lysosomal pathway was roughly estimated by taking sum of the R_t values for EE, LE and L. The sum of R_t ($\sum R_t$) increased during loading ($t \leq 1$ h) and maintained virtually constant at above 0.8 (Figure 3.6D), suggesting that the aDxt-MPNPs mainly followed the endo-lysosomal pathway, and the endosomal escape was almost entirely absent. To definitively confirm that aDxt-MPNPs were delivered to lysosomes without endosomal escape, the aDxt-MPNPs treated COS-1 cells after t = 8 h was examined by transmission electron microscopy (TEM) and energy-dispersive X-ray spectroscopy (EDS) elemental mapping (Figure 3.8). As a result, it was clearly revealed that the aDxt-MPNPs were mostly distributed in lysosome-like structures (Figure 3.8A). Although some vesicles that contain aDxt-MPNPs might be LE due to the difficulty with discriminating LE from L in a TEM image in general, most of vesicles that contain aDxt-MPNPs are certainly L (Figure 3.8A). Meanwhile, aDxt-MPNPs were observed neither in EE nor in autophagosomes being

consistent with the result of the time-dependent colocalization analysis by CLSM. In addition, TEM-EDS elemental mapping analysis clearly revealed that aDxt-MPNPs maintained their structure even in L without being decomposed (Figure 3.8B-E).

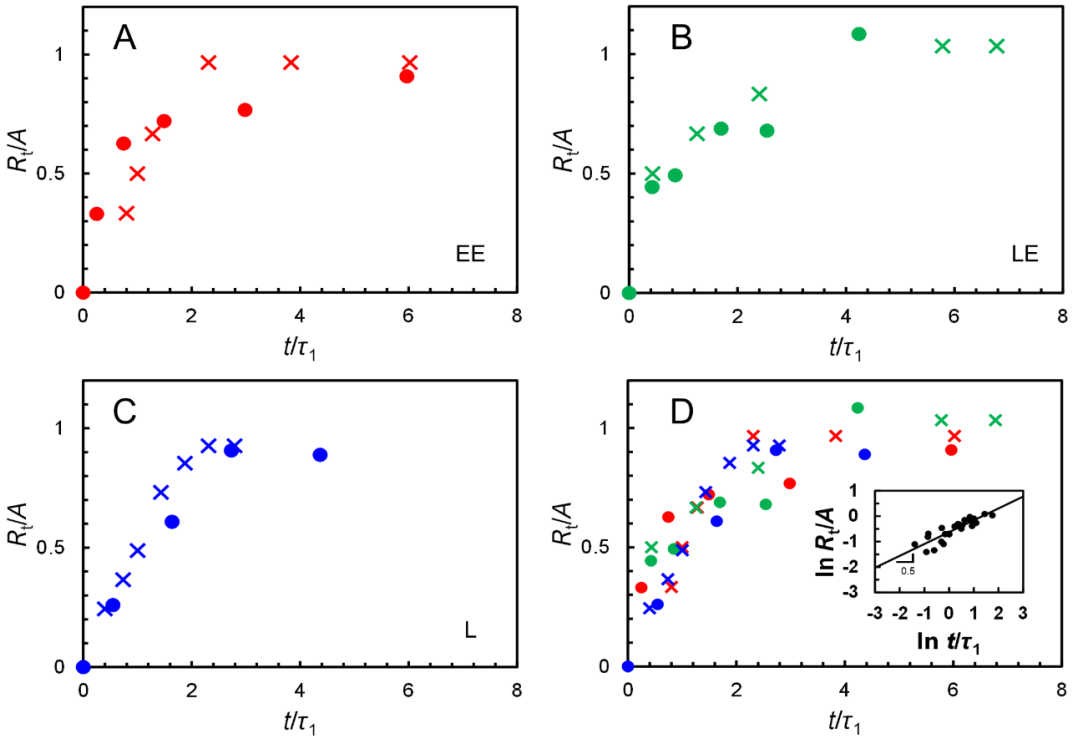

Figure 3.7: The plot of R_t/A vs t/τ_1 using our experimental results (circle) and data from Figure 2i in Ref. 12 (cross) indicates the accumulation trend of nanoparticles in (A) EE, (B) LE, (C) L, and (D) The combination of plots (a-c) and the double logarithmic graph (inset) shows the universal behavior of particle uptake through the endolysosomal pathway regardless of particle system and cell type.

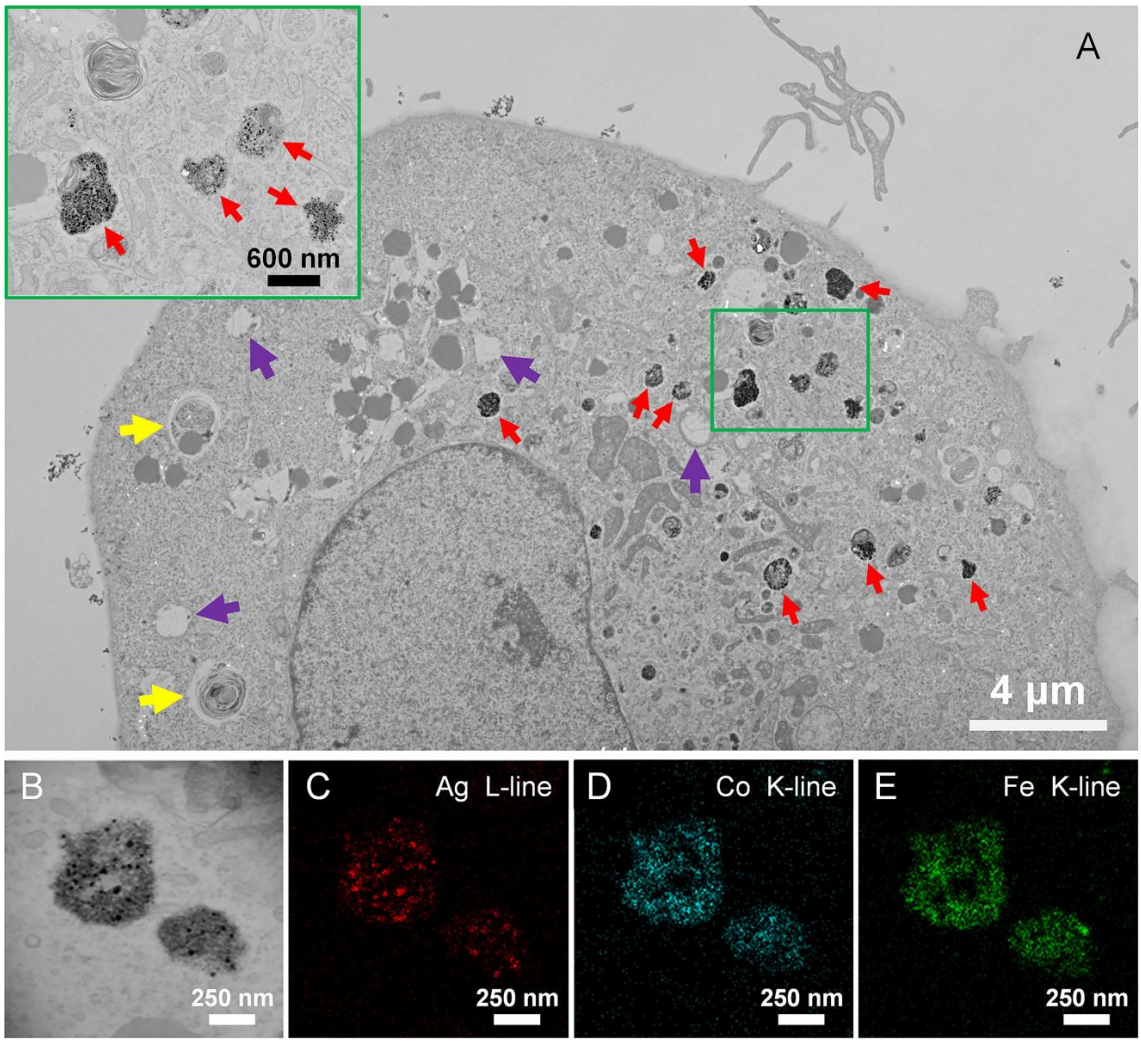

Figure 3.8: (A) TEM images of COS-1 cells treated with aDxt-MPNPs after 8 h incubation and the inset indicated the magnified region in green rectangle. aDxt-MPNPs were observed in lysosome-like structure (red arrows). Meanwhile, no particles were observed in early endosome (purple arrows) and autophagosome (yellow arrows). (B) A TEM image and (C-E) elemental mapping images of aDxt-MPNPs inside a lysosome-like structure: (C) Ag L-line, (D) Co K-line and (E) Fe K-line.

3.4. Conclusion

In order to obtain lysosome fraction with high purity, understanding the intracellular trafficking and intracellular fate of aDxt-MPNPs in COS-1 cells is a prerequisite. In this study, by using plasmonic scattering signal, aDxt-MPNPs could serve as an intrinsic and non-bleachable probe to investigate their intracellular transport using CLSM. Notably, by employing the colocalization analysis *via* R_t, the intracellular transport of aDxt-MPNPs along the endo-lysosomal pathway could be precisely traced. In addition, we extracted the time constants for the transport kinetics of aDxt-MPNPs. Interestingly, it was found that there exists a universal behavior of intracellular transport of nanoparticles regardless of types of nanoparticles and cells. This information is useful for optimizing t_{chase}. On the other hand, it has been also well known that each cell types have a distinct intracellular transport kinetics.[14] Especially, the disease-related cells may strongly alter the transport kinetics of the endolysosomal pathway.[15] To ensure magnetic nanoparticles reach lysosomes, t_{chase} is often extended to 24 or 48 h;[16, 17] however, for a considerably extended t_{chase}, the long-term accumulation of non-degradable nanoparticles into lysosomes may induce cellular stress,[18-21] which could influence the protein composition of lysosomes. Therefore, understanding of the transport kinetics is essential to optimize experimental parameters for adapting this protocol to various cell types to avoid undesired effect of nanoparticles on cellular activity.

References

1. Blanco, E.; Shen, H.; Ferrari, M., Principles of nanoparticle design for overcoming biological barriers to drug delivery. *Nat Biotechnol* **2015,** *33* (9), 941-51.

2. Yameen, B.; Choi, W. I.; Vilos, C.; Swami, A.; Shi, J.; Farokhzad, O. C., Insight into nanoparticle cellular uptake and intracellular targeting. *Journal of Controlled Release* **2014,** *190*, 485-499.

3. Foroozandeh, P.; Aziz, A. A., Insight into Cellular Uptake and Intracellular Trafficking of Nanoparticles. *Nanoscale Res Lett* **2018,** *13* (1), 339.

4. Wilson, S. M.; Bacic, A., Preparation of plant cells for transmission electron microscopy to optimize immunogold labeling of carbohydrate and protein epitopes. *Nat Protoc* **2012,** *7* (9), 1716-27.

5. Snipstad, S.; Hak, S.; Baghirov, H.; Sulheim, E.; Morch, Y.; Lelu, S.; von Haartman, E.; Back, M.; Nilsson, K. P. R.; Klymchenko, A. S.; de Lange Davies, C.; Aslund, A. K. O., Labeling nanoparticles: Dye leakage and altered cellular uptake. *Cytometry A* **2017,** *91* (8), 760-766.

6. Thomsen, T.; Ayoub, A. B.; Psaltis, D.; Klok, H. A., Fluorescence-Based and Fluorescent Label-Free Characterization of Polymer Nanoparticle Decorated T Cells. *Biomacromolecules* **2021,** *22* (1), 190-200.

7. Milosevic, A. M.; Rodriguez-Lorenzo, L.; Balog, S.; Monnier, C. A.; Petri-Fink, A.; Rothen-Rutishauser, B., Assessing the Stability of Fluorescently Encoded Nanoparticles in Lysosomes by Using Complementary Methods. *Angew Chem Int Ed Engl* **2017,** *56* (43), 13382-13386.

8. Donahue, N. D.; Acar, H.; Wilhelm, S., Concepts of nanoparticle cellular uptake, intracellular trafficking, and kinetics in nanomedicine. *Adv Drug Deliv Rev* **2019,** *143*, 68-96.

9. Oh, N.; Park, J. H., Endocytosis and exocytosis of nanoparticles in mammalian cells. *Int J Nanomedicine* **2014,** *9 Suppl 1*, 51-63.

10. Mosquera, J.; Garcia, I.; Liz-Marzan, L. M., Cellular Uptake of Nanoparticles versus Small Molecules: A Matter of Size. *Acc Chem Res* **2018,** *51* (9), 2305-2313.

11. Arthur, D.; Vassilvitskii, S., k-means++: the advantages of careful seeding. In *Proceedings of the eighteenth annual ACM-SIAM symposium on Discrete algorithms*, Society for Industrial and Applied Mathematics: New Orleans, Louisiana, 2007; pp 1027–1035.

12. Liu, M.; Li, Q.; Liang, L.; Li, J.; Wang, K.; Li, J.; Lv, M.; Chen, N.; Song, H.; Lee, J.; Shi, J.; Wang, L.; Lal, R.; Fan, C., Real-time visualization of clustering and intracellular transport of gold nanoparticles by correlative imaging. *Nat Commun* **2017,** *8*, 15646.

13. Toth, A. E.; Nielsen, S. S. E.; Tomaka, W.; Abbott, N. J.; Nielsen, M. S., The endo-lysosomal system of bEnd.3 and hCMEC/D3 brain endothelial cells. *Fluids Barriers CNS* **2019,** *16* (1), 14.

14. S, S. M.; Brown, A. I.; Koslover, E. F., Getting around the cell: physical transport in the intracellular world. *Phys Biol* **2020,** *17* (6), 061003.

15. Lloyd-Evans, E.; Morgan, A. J.; He, X.; Smith, D. A.; Elliot-Smith, E.; Sillence, D. J.; Churchill, G. C.; Schuchman, E. H.; Galione, A.; Platt, F. M., Niemann-Pick disease type C1 is a sphingosine storage disease that causes deregulation of lysosomal calcium. *Nat Med* **2008,** *14* (11), 1247-55.

16. Walker, M. W.; Lloyd-Evans, E., A rapid method for the preparation of ultrapure, functional lysosomes using functionalized superparamagnetic iron oxide nanoparticles. *Methods Cell Biol* **2015,** *126*, 21-43.

17. Akter, F.; Ponnaiyan, S.; Kögler-Mohrbacher, B.; Bleibaum, F.; Damme, M.; Renard, B. Y.; Winter, D., Multi cell line analysis of lysosomal proteomes reveals unique features and novel lysosomal proteins. **2020**, 2020.12.21.423747.

18. Ma, X.; Wu, Y.; Jin, S.; Tian, Y.; Zhang, X.; Zhao, Y.; Yu, L.; Liang, X. J., Gold nanoparticles induce autophagosome accumulation through size-dependent nanoparticle uptake and lysosome impairment. *Acs Nano* **2011,** *5* (11), 8629-39.

19. Schutz, I.; Lopez-Hernandez, T.; Gao, Q.; Puchkov, D.; Jabs, S.; Nordmeyer, D.; Schmudde, M.; Ruhl, E.; Graf, C. M.; Haucke, V., Lysosomal Dysfunction Caused by Cellular Accumulation of Silica Nanoparticles. *J Biol Chem* **2016,** *291* (27), 14170-14184.

20. Zhang, X.; Zhang, H.; Liang, X.; Zhang, J.; Tao, W.; Zhu, X.; Chang, D.; Zeng, X.; Liu, G.; Mei, L., Iron Oxide Nanoparticles Induce Autophagosome Accumulation through Multiple Mechanisms: Lysosome Impairment, Mitochondrial Damage, and ER Stress. *Mol Pharm* **2016,** *13* (7), 2578-87.

21. Huang, Q.; Zhang, J.; Zhang, Y.; Timashev, P.; Ma, X.; Liang, X. J., Adaptive changes induced by noble-metal nanostructures in vitro and in vivo. *Theranostics* **2020,** *10* (13), 5649-5670.

Chapter 4: Magnetic Isolation of lysosomes

4.1. Introduction

After human genome project was finished in 2003, proteomics has gained great attention for the deeper insight cellular process which has not been depicted by genomes.[1] A challenge in proteomic research is understand the locality and functional activity of protein in given eukaryotic cell. Among subcellular compartments, lysosomes have been extensively investigated by proteomics is lysosomes, owing to their important roles in cellular functions.[2, 3] Due to the low abundant of lysosomal proteins in a eukaryotic cell,[4, 5] rapid and efficient isolation of intact lysosomes is essential to obtain a reliable proteomic dataset to reveal their functions and metabolites. Of note, magnetic separation has become a popular choice to isolate different intracellular organelles including lysosomes from the complex cell lysate. The primary advantages of magnetic separation are quick and swift, which could preserve the integrity of lysosomes during the separation process. Furthermore, it is also known to be high-throughput, low-cost, and less energy-intensive. To present, two magnetic separation methods has been established for magnetically isolating lysosomes from various cell types including LSDs cells are immunoprecipitation and intravascular magnetization. The former approach has been extensively used to purify proteins and organelle like mitochondria. However, its application for isolating lysosome is limited due to the lack of lysosomal membrane proteins with cytosolic-facing epitopes. The modification of lysosomal membranes is required to obtain the efficient isolation process. Although the isolated fraction has high purity, the subsequent proteomics analysis could be influenced due to the modified

lysosomal membrane.[6] The second approach is the intravascular magnetization of lysosomes by delivering magnetic nanoparticles to lysosomal lumens, which was investigated in chapter 3. The advantage of this technique is that the lysosomal membranes and magnetic nanoparticles do not require special modifications using antigens and antibodies, while the lysosomes still can be isolated with high yield and purity.

Generally, the magnetic nanoparticles would have much small magnetic moment compared to their bulk, which may have adverse effect on the separation process. To address this concern, Miltenyi et al. developed high gradient magnetic column for magnetic separation,[7] which greatly extends the application of magnetic separation to magnetic nanoparticles. Today, Miltenyi columns are often regarded as the gold standard in magnetic separation, which have been extensively used for magnetic cell separation system (MACS). Nevertheless, they also can be adapted to use with other magnetic separation processes of proteins and subcellular compartment.

In this chapter, we presented the protocol of magnetic isolation of lysosomes using MACS separator (Miltenyi Biotec) after accumulation of MPNPs into lysosomal lumen shown in chapter 3. Following this, the purity of the obtained lysosomal fraction was determined using Western blot. Also, a comparison in term of yield and purity of the established isolation method with density gradient centrifugation technique was made. Also, we demonstrated that the elapsed time from homogenization to complete isolation of lysosomes (t_{delay}) and temperature could potentially influence the protein composition of isolated lysosome fractions by sodium dodecyl sulfate-polyacrylamide gel electrophoresis (SDS-PAGE) and amino acid analysis using high-performance liquid chromatography (HPLC). Finally, we confirmed that the established protocol could be

easily adapted with other cell-lines.

4.2. Experiments

4.2.1. Chemicals

- PBS buffer solution and DMEM were prepared as in chapter 2&3.
- Protase inhibitor solution (PIS): Prepare 20 mL of PBS in a 50 mL tube. Add 20 µL of 0.1 M phenylmethylsulfonyl fluoride and 100 µL of protease inhibitor cocktail to the tube. The dilution factor is about ×1000 and ×200 for phenylmethylsulfonyl fluoride and protease inhibitor cocktail, respectively. Disperse solution homogeneously using a vortex. Then, keep the solution in an ice box.

Note: This solution should be prepared at the time of use. Long-term storage is not recommended. The composition of the inhibitor cocktail is: 0.1 mg/mL leupeptin hemisulfate monohydrate; 0.14 mg/mL pepstatin A; 14 mg/mL N-p-tosyl-L-phenylalanine chloromethyl ketone; 15 mg/mL N_{α}-p-tosyl-L-arginine methyl ester hydrochloride; 0.4 mg/mL aprotinin; 32 mg/mL benzamidine dissolved in DMSO. The inhibitor cocktail can be prepared in advance and stored in small tube at -20°C.

4.2.2. Accumulation of aDxt-MPNPs to lysosomes, homogenization, and magnetic isolation of lysosomes

- Seed 2 × 10^6 COS-1 cells/dish for two 10 cm dishes and incubate in DMEM (+10% FBS) for 24 h.
- Check the health and confluency of cells under a bright-field microscope (Keyence, model: BZ-X810) in advance.

Note: The health of COS-1 cells was checked by confirming their adhering status on a cell dish using bright-field microscopy. In addition, the possibility of contamination was also checked at the same time. The confluency of cells was estimated to be less than 80%

in this particular experiment. However, it would change depending on the cell type. The desired confluency of cells would be ranging from 70% to 80%. If cells are well adhered on the dish without being contaminated and with around 70-80% confluency, one can go to the next step.

- For cell starvation, add 5 mL of pre-warmed DMEM without FBS to each cell dishes and incubate for 30 min at 37ºC under 5% CO_2.
- About 10 min before finishing the starvation process, add MPNPs to DMEM (+10% FBS) to prepare a 10 mL of dispersion of MPNPs with the concentration of 100 µg/mL.
- Immediately after starvation, replace DMEM without FBS with 5 mL of MPNPs dispersion in DMEM (+10% FBS) (prepared in step 4) to each cell dishes and incubate for 8 h at 37ºC under 5% CO_2.

Note that: In this study, we chose the t_{load} = 8 h for loading. t_{load} strongly affects the isolation yield of lysosomes. This parameter could be prolonged depending on the cytotoxicity of MPNPs to the cells.

- Discard the aDxt-MPNPs containing medium, wash with pre-warmed PBS one time.
- Add 5 mL of DMEM (+10% FBS) and incubate further for t_{chase} = 7 h. The optimal t_{chase} has been already determined in the pulse-chase experiment section. Depending on the cell type, this parameter may vary.
- Place necessary equipment including the magnetic column, MidiMACS separator, 2.5 mL syringe with 23G-needle (Terumo syringe with needle 2.5 mL 23G blue), and 5 mL tubes into the cold room where the temperature is maintained at 4 °C at least 30 minutes before the pulse-chase experiment to equilibrate the temperature.
- Discard the medium and wash the cells with PBS.
- Add 1.5 mL of cold-PBS to each culture dishes and place them on ice.
- Scrape off the cells and transfer the cells from both culture dishes to a 15 mL centrifuge tube. Centrifuge at 190 × g using Kubota 5910 with ST-720 swinging

bucker rotor for 4 min at 4°C.

Note: In this step, the amount of particle uptake could be qualitatively evaluated via the color of the cell pellet (Figure 4.1). The darker the color, the higher number of particles internalized. If the cell color is still white, it means a very low uptake efficiency. The isolation of lysosomes may fail.

- Discard the supernatant and add 1 mL of ice-cold PIS to re-suspend the cell pellet. Then, transfer to a 5 mL tube and keep in an icebox.

Note: After this step, the experiments are continued in a low-temperature room where the temperature is maintained at 4°C.

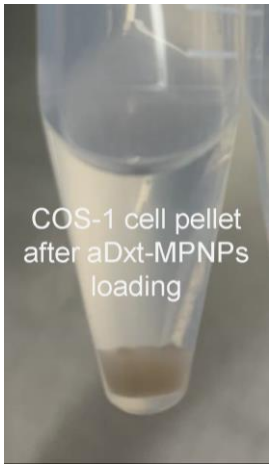

Figure 4.1: A photograph of aDxt-MPNPs loaded COS-1 cells with t_{load} = 8 h and t_{chase} = 7 h.

- Use a 2.5 mL syringe with a 23G-needle and pass cell suspension repeatedly (15 passages) through the syringe to homogenize the cells.

Note: The optimal number of passages must be determined experimentally (Figure 4.2). The low homogenization efficiency could obviously affect to the yield of lysosome isolation. In contrast, homogenization efficiency enhanced by increasing number of passages may also lead to lysosomes broken. Therefore, in this study, a small portion of unbroken cells or large cell fragments is left over.

- Place an MS Column in a MidiMACS separator.

Note: Another type of MACS® Column such as LS Column could be also used in this experiment.

- Equilibrate the MS Column by adding 1 mL of PIS. Discard the flow-through.

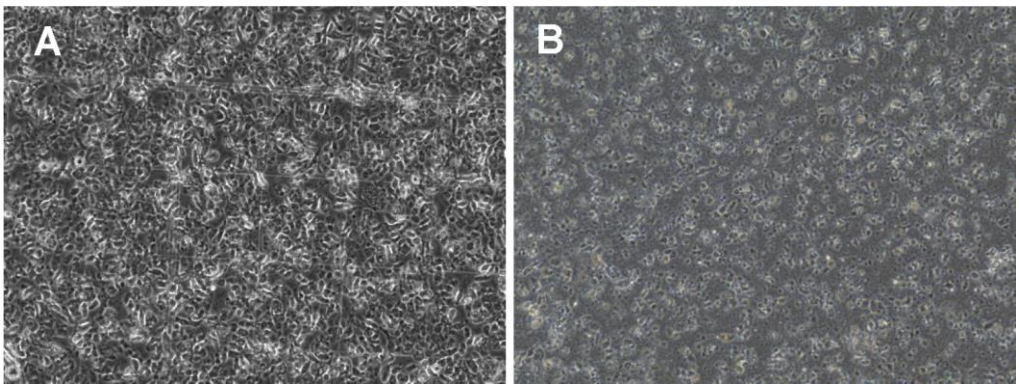

Figure 4.2: The bright-field image of COS-1 cells under phase contrast mode: (A) before and (B) after homogenization using a syringe with a 23G-needle (15 passages). Before homogenization, cells can clearly be seen as a high density of dark areas encircled by bright halos. After homogenization, the number of cells is reduced, the cell mixture becomes a slurry due to the breaking of the cell membranes. Consequently, the number of bright halos decreases significantly. A small portion of either unbroken cells or large cell fragments in the slurry can still be observed.

- Transfer the cell lysate (prepared in step 13) to the MS Column using the micropipette. And let the cell lysate pass through the column. The magnetic fraction will be trapped inside the column, while the nonmagnetic fraction will pass through the column. (Figure 4.3)
- Discard the flow through. Wash the column using 1 mL of PIS twice to further eliminate unbound materials.
- Remove the MS Column from the MidiMACS separator.
- Add 0.5 mL of PIS and insert the plunger to collect the magnetic fraction containing lysosomes in a 1.5 mL microtube. Repeat this step once again.
- Centrifuge the obtained suspension at 5,000 × g using an MDX-310 system for 10

min at 4°C.

Note: This step is to remove the remaining soluble proteins in the isolated fraction.

- Discard the supernatant and redisperse the obtained lysosome pellet in 100 µL of PIS.

Note: If the isolated lysosome fraction is subjected to proteome analysis, re-suspend the pellet in 50 mM triethylammonium bicarbonate.

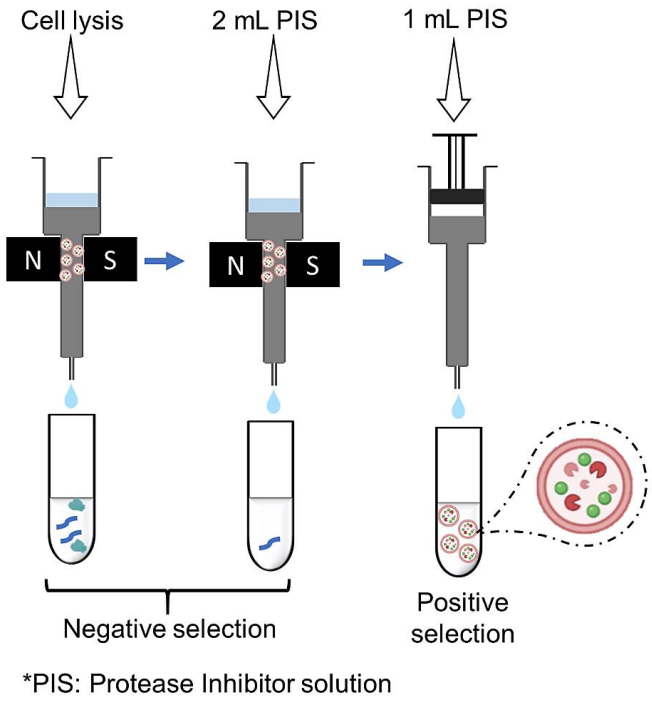

Figure 4.3: Illustration of magnetic isolation procedure of lysosomes.

4.2.3. SDS-PAGE and Western blotting

The whole cell lysis, negative selection (NS) and positive selection (PS) fractions (40 µL of each sample), were separated by sodium dodecyl sulfate-polyacrylamide gel electrophoresis (SDS-PAGE).

- Prepare separation gel 12% and 8% as follow:

	8% Acrylamide gel	12% Acrylamide gel
H_2O	9.7 mL	4.4 mL
Acrylamide/bis (30%)	5.3 mL	4.6 mL
Tris-HCl (1.5M, pH 8.8)	5.0 mL	2.5 mL
SDS, 10%	200 µL	100 µL
N,N,N′,N′tetramethylethylene-diamine	16 µL	16 µL
Ammonium persulfate	1 spatula*	1 spatula*

**Spatula (AS one, Micro Spatula 150mm, 1-9404-01)*

Note: 8% gel was used to obtain the Western blot of LAMP2, GAPDH, GM130, while the 12% gel was used for TOM20, LC3, Rab7.

- Inject gel to cassette, leave ~5 cm above for the comb and stacking gel.
- Layer the top of the gel with isopropanol.
- After gel is completely polymerized (~ 30 min), remove isopropanol and wash with DI. water.
- Prepare the stacking gel:

H_2O	6.0 mL
Acrylamide/bis (30%)	800 µL
Tris–HCl (0.5 M, pH 6.8)	0.93 mL
SDS, 10%	75 µL
N,N,N′,N′tetramethylethylene-diamine	6 µL
Ammonium persulfate	half of spatula

- Pour stacking gel on the top of the separation gel and insert the combs to make well. The stacking gel will completely be polymerized in about 90 min.
- Clamp gel into apparatus, fill chamber with running buffer, remove comb and then loads samples and protein markers into wells.
- Apply voltage of 200 V for separation by electrophoresis

- After separation, transfer proteins from gels to polyvinylidene difluoride membrane (PVDF, Bio-Rad) in CAPS buffer (10 mM CAPS and 10% of methanol, pH = 11) by a semi-dry method (applied voltage: 15V, transfer time: 40 min).
- Wash PVDF membrane with tris-buffered saline (TBS) containing 0.05% Tween 20 (TBST).
- Blocking with 5% skim milk in TBST for 30 min at room temperature.
- Washing membrane with TBST, cut the membrane to the specific molecular mass region containing the proteins of interest.
- Incubate membranes with the primary antibodies GM130, LAMP2, anti-TfnR, GAPDH, Rab7, LC3, and TOM20 at 4°C overnight.
- In the next day, wash membranes with TBST and incubate membranes with the secondary antibody conjugated to horseradish peroxidase for 1 h at room temperature in in TBST containing 5 wt% skim milk.
- Wash membranes with TBST and visualize protein bands using chemiluminescence using a detector (LAS-3000, Fujifilm).

Note: For SDS-PAGE analysis of quickly- and laggardly-Isolated lysosome fractions, the PS fraction obtained by magnetic separation with t_{delay} = 30 and 120 min at 4°C and 25°C was separated by SDS-PAGE. The protein bands were detected using a silver staining technique and analyzed using ImageJ.

4.2.4. Amino acid analysis of lysosomes

The time interval between the cell lysis and the completion of magnetic separation (t_{delay}) under the standard condition was 30 min as mentioned above. To investigate the potential variation of the protein composition of lysosomes over t_{delay}, the lysosome fraction was isolated with t_{delay} = 30 and 120 min at low temperature (4 °C) and at room temperature

(25 °C). Subsequently, the amino acid composition of the obtained lysosome fractions was analyzed by HPLC.

- Dry the lysosome fractions completely in glass tubes under vacuum.
- Place obtained sample tube in mininert valve tubes with 200 μL of 6 N HCl.
- Remove air and close valve, then hydrolyze at 110 °C for 20 h.
- Next day, dissolve the hydrolysate in 100 μL of 0.01 N HCl and centrifuged at 20,000 × g for 10 min.
- Collect supernatant and add an equal volume of 1 M $NaHCO_3$ (pH = 9.0), and a 2-fold volume of dabsyl chloride (7.7 mM in acetone/acetonitrile, 50:50 v/v).
- Vortex the mixture and place in thermal block for reaction at 70 °C for 12 min. After that, quench reaction using an ice bath.
- Dilute the obtained dabsylated samples 3-fold with 20 mM ammonium acetate (NH_4OAc, pH = 5.5).
- Take 10 μL of diluted samples for HPLC analysis (Ultimate 3000, Thermo Fisher Scientific) with an analytical column (InertSustain C18, 5 μm, 4.6 ID × 250 mm, GL Sciences) at 50 °C.

Note: The conditions for HPLC analysis were as follows: buffer A: 20 mM NH_4OAc/acetonitrile (85:15 v/v), buffer B: acetonitrile, gradient conditions: 20% B (0 min)–40% B (25 min)–60% B (30 min)–90% B (31 min)–90% B (35 min)–10% B (36 min)–10% B (45 min), flow rate: 0.5 mL/min.

- Monitor the elute at 465 nm.

Note: to determine the amino acid retention time, a standard amino acid sample was analyzed under the same conditions.

4.3. Results and Discussions

4.3.1. Magnetic isolation of lysosomes

Specifically, COS-1 cells were incubated with aDxt-MPNPs for t_{load} = 8 h in DMEM (+10% FBS). Subsequently, the chase was conducted for t_{chase} = 7 h to deliver aDxt-MPNPs to lysosomes as the result of intracellular trafficking study. After that, the cells were removed from culture dish using a lifter in ice-cold protease inhibitor solution (PIS) and homogenized using 2.5 mL syringe with 23G needle after 15 passages. The obtained cell lysate was subjected to MS column using MidiMACS separator (Figure 4.3). After unbounded fraction came out, 2 mL of PBS was added for washing. The obtained unbounded materials were denoted as negative selection (NS). Finally, the bounded material (positive selection, PS) was eluted twice using 0.5 mL of PIS solution for each time. Figure 4.4A shows the photograph of NS and PS fraction after centrifugated 5,000 × g for 10 min, the PS fraction showed the color of aDxt-MPNPs, meanwhile the NS fraction was colorless. The total elapsed time between homogenization and the completed magnetic separation of the standard procedure is within 30 min. The lysosome isolation was also performed with the case t_{load} = 1 h. As expected, it was also confirmed that the number of isolated lysosomes in the case of t_{load} = 8 h was higher than that in the case of t_{load} = 1 h as shown in Figure 4.4B. To characterize the purity of isolated lysosome fraction with t_{load} = 8h, the Western blot analysis for various protein markers was performed (Figure 4.4C). LAMP2 (lysosomal marker) was detected in PS. Meanwhile, other markers including GAPDH, TOM20 (mitochondria marker), GM130 (golgi marker), LC3 (autophagosome marker), TfnR (endosomal marker protein) and Rab7 (LE marker) were not clearly observed in PS fraction indicating the purity of isolated lysosomes was high.

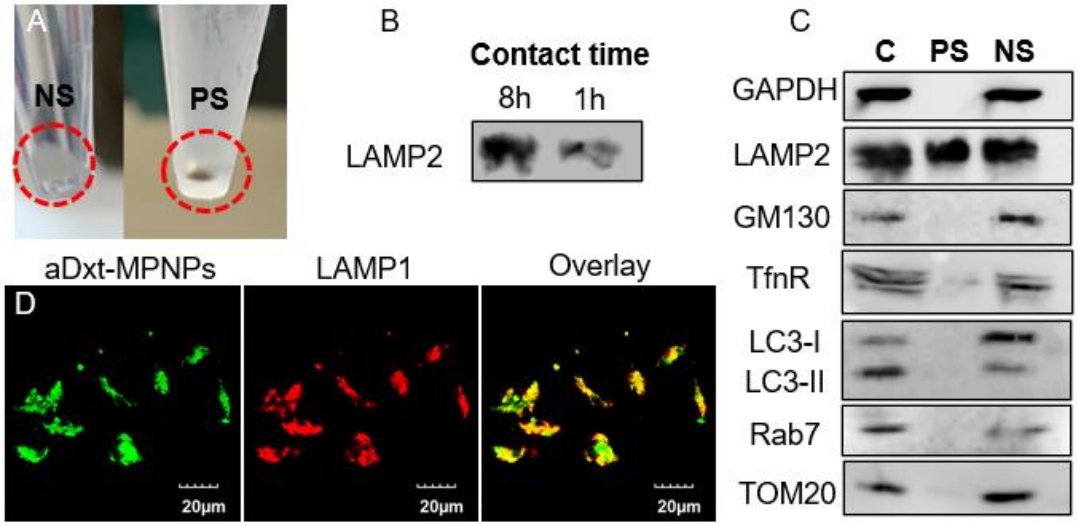

Figure 4.4: (A) Photograph of NS and PS fraction. (B) Western blot of isolated fraction obtained at different t_{load} = 1 h and 8 h. (C) Western blot analysis of the NS, PS fraction and whole cell lysate using different protein markers. (D) CLSM image of the PS fraction (green: aDxt-MPNPs, red: LAMP1).

The isolated lysosome fraction was also characterized by CLSM imaging. Figure 4.4D shows the CLSM image of isolated lysosomes after staining using LAMP1 (green: aDxt-MPNPs, red: LAMP1). By analyzing colocalization of aDxt-MPNPs and lysosome, the R_t value was determined to 0.64 ± 0.03. The overlap of aDxt-MPNPs and LAMP1 implies that aDxt-MPNPs remained in lysosomal lumens. To further confirm the integrity of lysosomes, 3D CLSM image was taken (Figure 4.5).

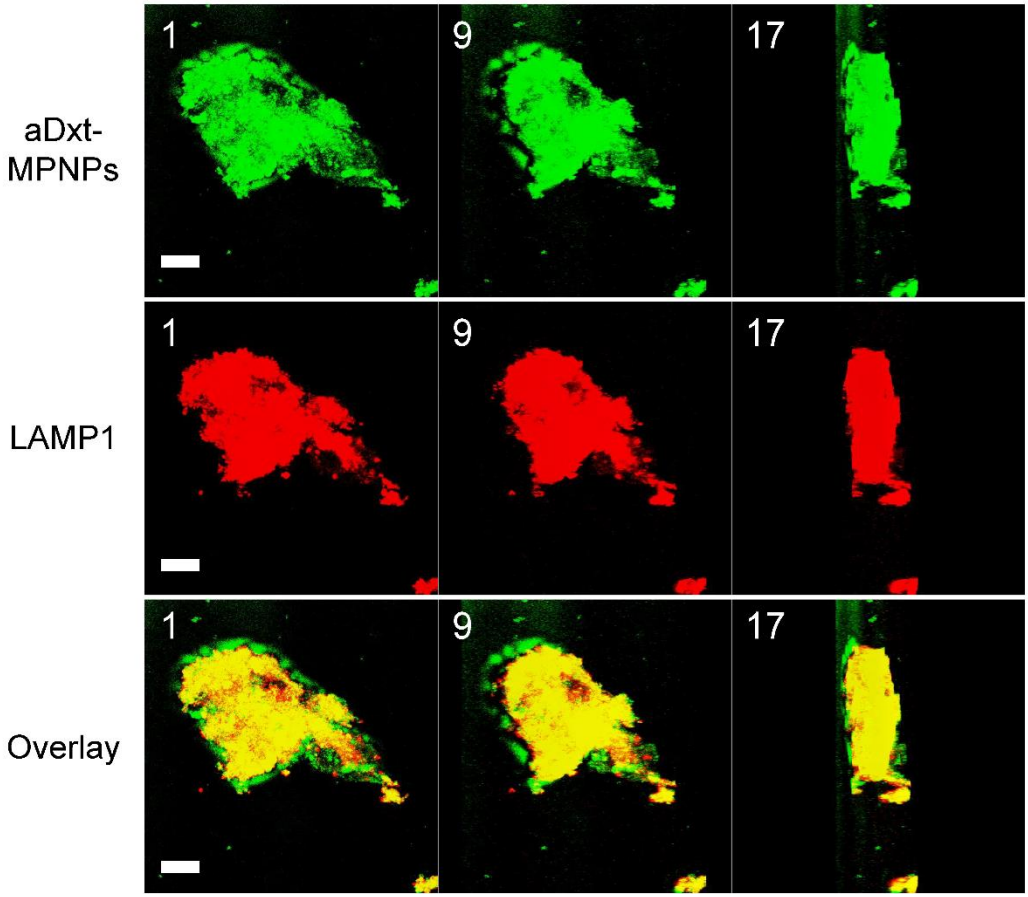

Figure 4.5: Montage of isolated lysosomes rotating about y-axis. The number represent the frames, with the series captured at 3 frames per second. The high colocalization of aDxt-MPNPs and lysosomes (LAMP1) suggested that aDxt-MPNPs were remained in lysosomal lumen. Note: the green color in the overlay images originated from the scattering of the glass substrate. Scale bar, 10 μm.

4.3.2. Amino acid compositions in quickly- and laggardly-isolated lysosomes

In this study, the standard condition of the magnetic separation of lysosomes was conducted at a low temperature room of 4°C with t_{delay} = 30 min. To reveal the potential variation of protein composition of isolated lysosome fraction after cell homogenization, t_{delay} was varied under low (4°C) and room (25°C) temperature conditions.

The SDS-PAGE analysis of lysosome fraction obtained under different condition was

shown Figure 4.6A. By subtracting background and measuring the intensity of some protein bands using ImageJ, the intensities of each band normalized to the intensity of a criterial band were calculated (Figure 4.6B). In consequence, it was found that the intensity of some bands increased while others decreased. Those results indicate the protein composition in lysosomal fraction were changing even at 4°C. It is possible that the denaturation, degradation, and loss of proteins would be the reason for those variation. The denaturation and degradation of protein would not change amino acid content. Therefore, amino acid composition analysis using HPLC was performed to reveal the potential loss of protein according to isolation condition. The HPLC chromatogram of the standard amino acids derivatized by dabsyl chloride was shown in Figure 4.7, which identify 16 amino acids after 45 min.

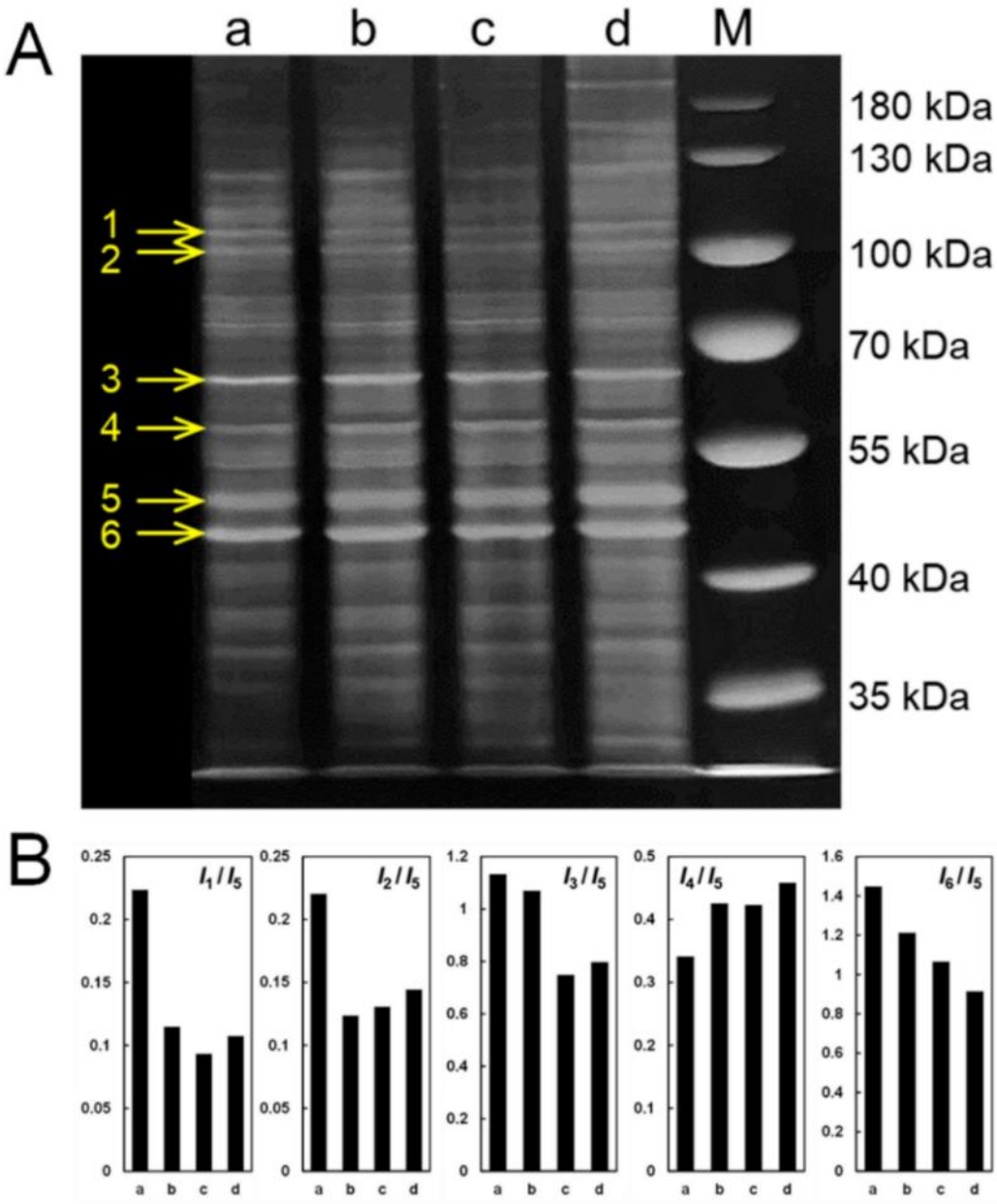

Figure 4.6: (A) The SDS-PAGE analysis of lysosomes fractions obtained under different conditions: (a) at 4°C with t_{delay} = 30 min, (b) at 4°C with t_{delay} = 120 min, (c) at 25°C with t_{delay} = 30 min, (4) at 25°C with t_{delay} = 120 min, and M: the page ruler prestained protein ladder. The 8% gel was used to separate proteins, which is later stained using silver staining technique. (B) The intensity weighted ratio of some region of interest suggests the effect of t_{delay} and temperature on the variation of protein composition in isolated lysosome fractions.

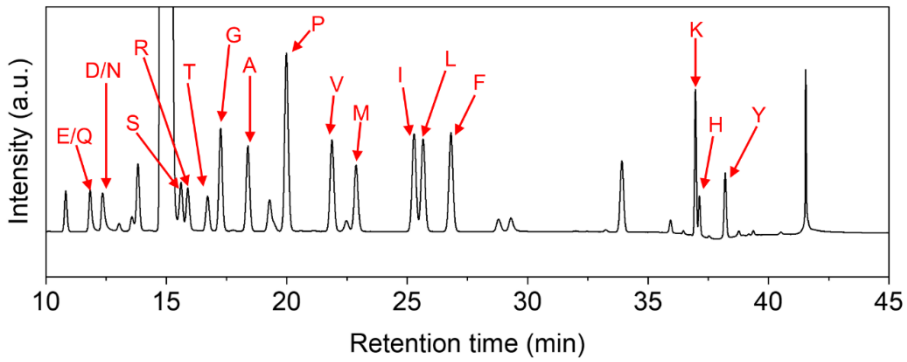

Figure 4.7: The HPLC chromatogram of standard amino acids derivatized by dabsyl chloride. The HPLC condition was conducted as follow: InertSustain C18 column (5µm, 4.6 ID × 250 mm, GL Sciences), Buffer A: 20 mM NH_4OAc/acetonitrile (85:15 v/v), Buffer B: acetonitrile, gradient conditions: 20% B (0 min)–40% B (25 min)–60% B (30 min)–90% B (31 min)–90% B (35 min)–10% B (36 min)–10% B (45 min), Flow rate: 0.5 mL/min. Wavelength of detection at 465 nm. 16 amino acids were separated after 45 min. Amino acid abbreviations: E: Glutamic acid, Q: Glutamine, D: Aspartic acid, N: Asparagine, S: Serine, R: Arginine, T: Threonine, G: Glycine, A: Alanine, P: Proline, V: Valine, M: Methionine, I: Isoleucine, F: Phenylalanine, K: Lysine, H: Histidine, Y: Tyrosine.

The reproducibility of lysosome isolation technique was confirmed through HPLC chromatogram of three independent lysosome isolation experiments (Figure 4.8). Then, the percentage of each amino acids in isolated lysosome fraction obtained from different conditions was calculated based on the total amount of identified amino acids (Fig 4.9A). Figure 4.9B shows the variation of some selected amino acids. It can be seen that the temperature strongly affects amino acid content. At t_{delay} = 30, all selected amino acids showed the significant different ($P < 0.05$) between 4°C and 25°C. Interestingly, at 25°C, the influence of t_{delay} = 120 min become less significant, only the significant change in the composition of valine and histidine was observed. It is presumably because the degradation and/or loss of unstable proteins was almost completed within 30 min at room

temperature. Meanwhile, at 4°C, the effect of t_{delay} could be clearly seen, more amino acids including arginine, threonine, glycine, and tyrosine shows the significant change over t_{delay}.

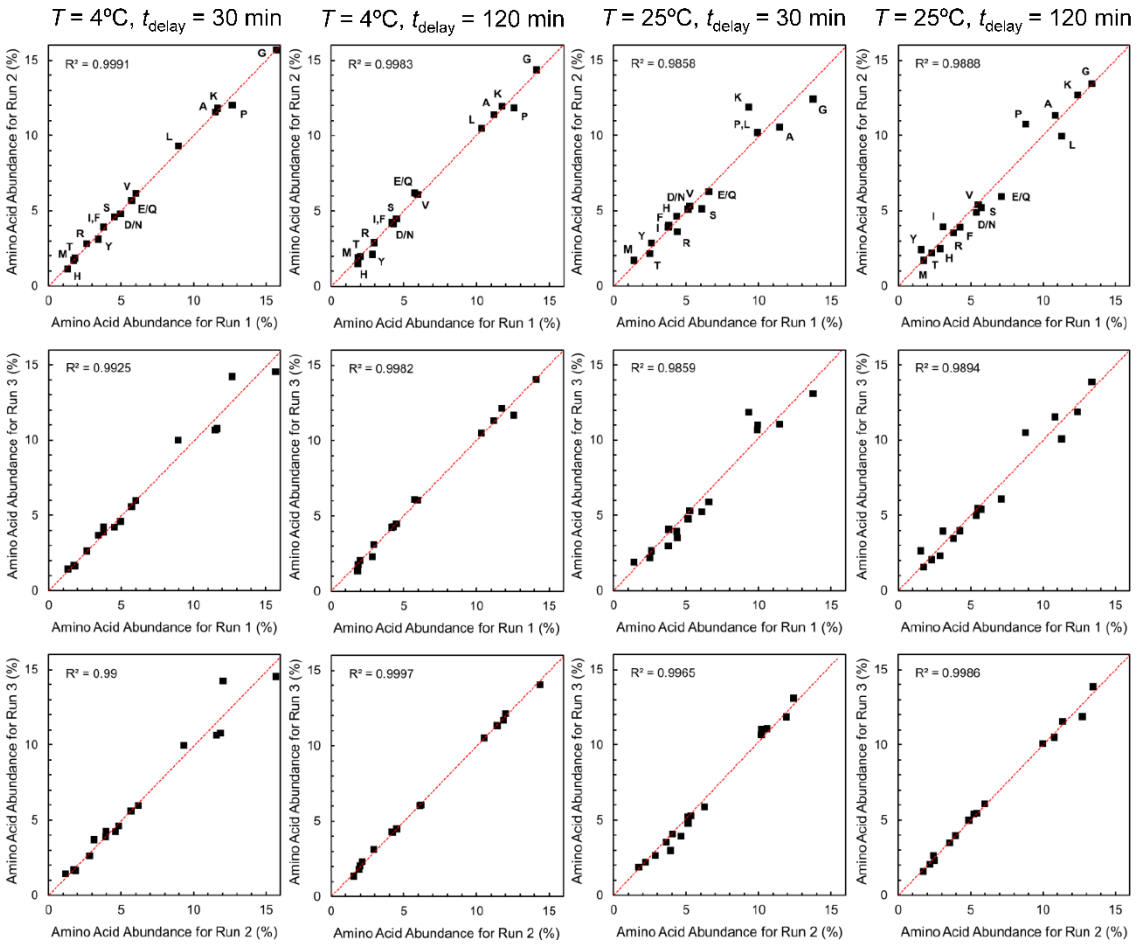

Figure 4.8: Amino acid analysis reproducibility. Pairwise correlation of the relative abundance of each amino acid between (top) Run 1 and Run 2, (middle) Run 1 and Run 3, (bottom) Run 2 and Run 3. The results indicate that the lysosome isolation technique is highly reproducible.

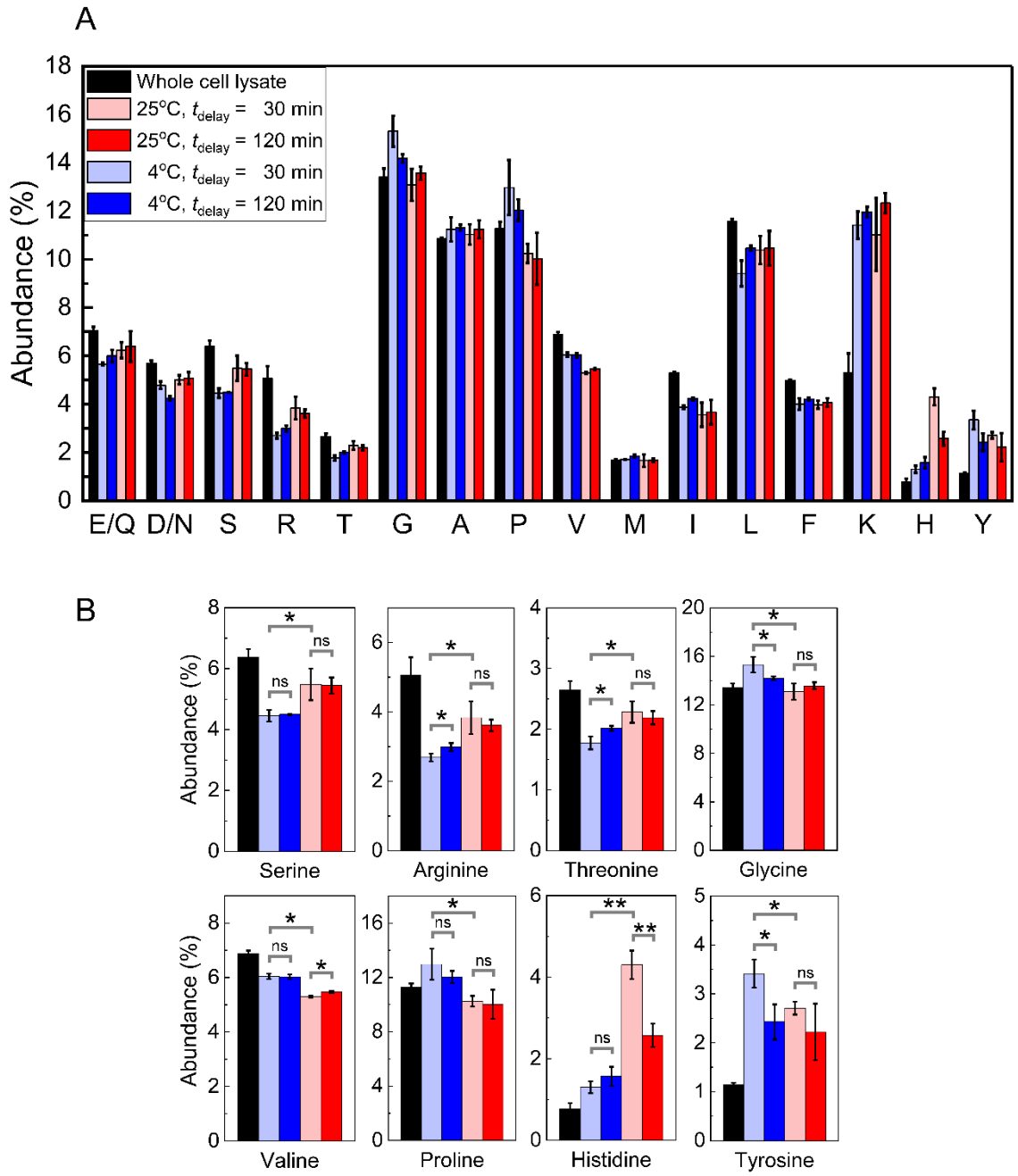

Figure 4.9: (A) The acid amine content of whole cell lysate (black) and the lysosome fractions isolated at different conditions: at 4°C with t_{delay} = 30 min (light blue), at 4°C with t_{delay} = 120 min (blue), at 25°C with t_{delay} = 30 min (pink), and at 25°C with t_{delay} = 120 min (red). (B) the variation of some selected amino acids in lysosome fraction obtained after manipulating t_{delay} at different temperature.

4.3.3. The comparison of the performance of the established isolation technique to the conventional method

To compare magnetic separation with density gradient centrifugation techniques in terms of isolation yield and purity, Lysosomes were isolated from COS-1 cells using Lysosome Isolation Kit (Abcam, ab234047) according to the manufacturer's instructions, which was shown in Figure 4.10A. For isolation of lysosomes, 2×10^7 COS-1 cells were cultured in 10 cm-culture dishes. Cells were homogenized using a syringe with 23G needle (25 passages). The resultant cell lysate was centrifuged at 500 × g for 10 min at 4°C. Then, the supernatant was collected and mixed with Lysosome Gradient solution with ratio of 3:1. In a centrifuge tube, a discontinuous density gradient was prepared by layering five gradient solutions. Then the as-prepared cell lysate was added to the top of the density gradient. The centrifugation was then performed at 145,000 × g for 2 h at 4°C. After that the visible lysosome band was carefully collected (Figure 4.10B). The lysosomal fraction was mixed with 2 volumes of PBS, followed by centrifugation at 18,000 × g for 30 min at 4°C. The pellet containing lysosomes was resuspended in PBS. To compare magnetic separation and density gradient centrifugation techniques in terms of isolation efficiency and purity, the total protein content of lysosomal fraction was quantitated by the Bradford assay using the TaKaRa Bradford Protein Assay Kit (No. T9310A, TaKaRa, Tokyo, Japan) following the manufacturer's instructions. The isolation yield was defined as $M_{protein}/N_{cell}$ where $M_{protein}$ and N_{cell} denote the total protein content in lysosomal fraction and the total number of cells required for lysosome isolation, respectively. The purity was evaluated by Western blot analysis. To make a fair comparison of the purity of lysosomes obtained by magnetic separation and by density gradient centrifugation, $M_{protein}$ of both the lysosomal fraction obtained magnetic

separation and the lysosomal fraction obtained by density gradient centrifugation was adjusted to be the same before performing SDS-PAGE and Western blot analysis. Figure 4.10C and table 4.1 showed that the total amount of proteins in lysosomal fraction obtained using DGC (56 μg) is significantly higher than that of MS (32 μg), but the number of cells used in DGC was five time higher that of MS. However, regarding the isolated yield $M_{protein}/N_{cell}$, MS method is better than DGC with 8.0 and 2.8 μg/million cells, respectively. Figure 4.10D showed the Western blot of cell lysate and isolated fractions of DGC and MS. Obviously, the lysosomes were successfully enriched using DGC with significant reduction of cytosolic protein, GAPDH. However, there existed the contamination from other organelles such as late endosomes (RAB7) and Autophagosome (LC3). In contrast, the MS could provide lysosomes fraction with higher purity. Additionally, while the lysosomes could be isolated using MS within 30 min after cell homogenization, the isolation time DGC technique was 150 min. In short, our current magnetic separation method was found to be superior to the density gradient centrifugation method, which is the most common method for lysosome isolation, in terms of number of cells required, isolation yield, purity, and t_{delay} as shown in table 4.1.

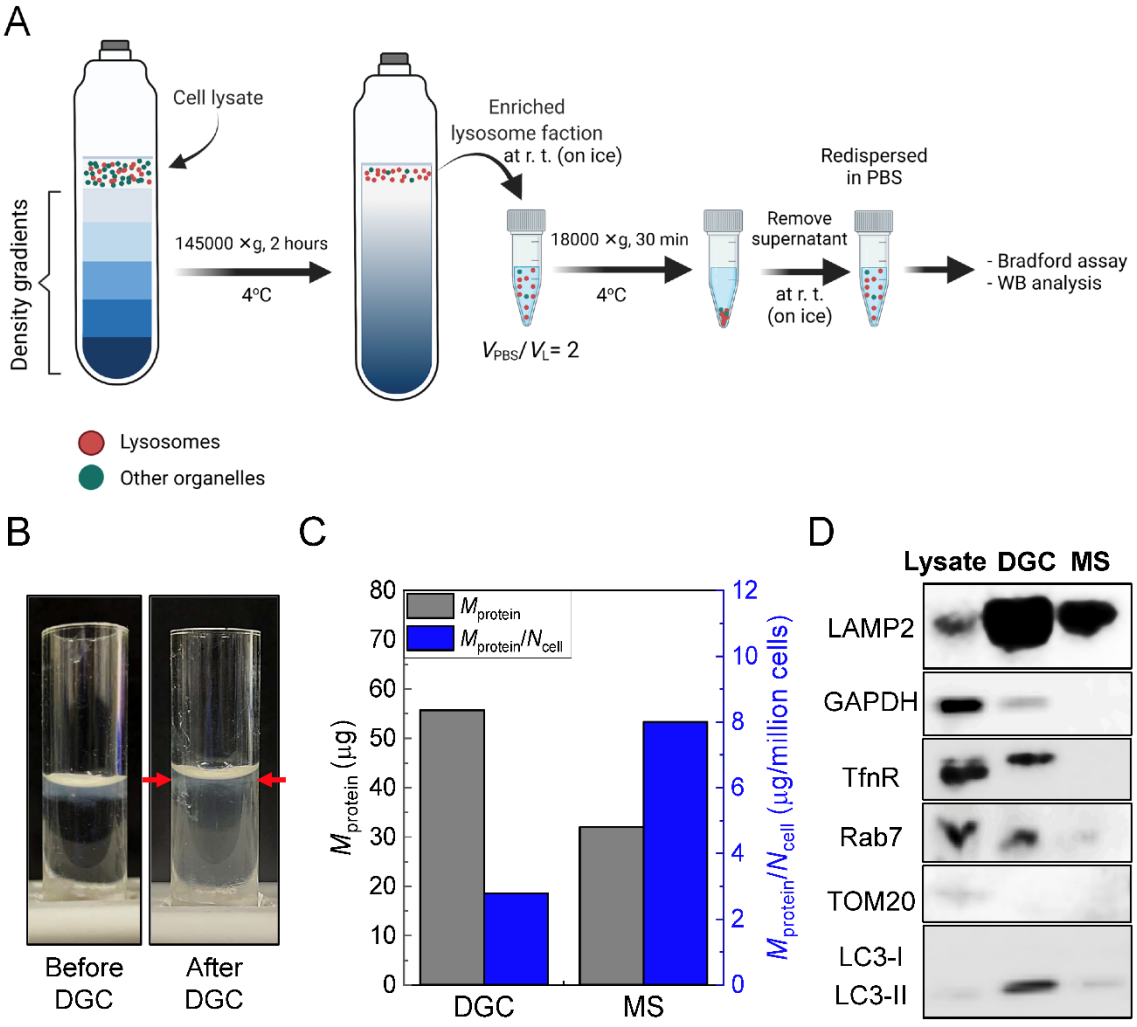

Figure 4.10: Comparison of magnetic separation (MS) and density gradient centrifugation (DGC) techniques in terms of isolation yield and purity. (A) Schematic illustration of DGC. V_{PBS} and V_L represent the volumes of PBS and lysosomal fraction, respectively. (Created with biorender.com) (B) Photograph of a centrifuge tube (left) before and (right) after DGC. The enriched lysosome band was indicated by red arrows. (C) The total protein content in lysosomal fraction [$M_{protein}$ (µg)] and the isolation yield defined as $M_{protein}/N_{cell}$ where N_{cell} (million cells) denotes the total number of cells required for lysosome isolation. (D) Western blot analysis of the lysosomal fraction obtained by MS and DGC.

Table 4.1: Comparison of magnetic separation (MS) and density gradient centrifugation (DGC) techniques in terms of number of cells required for isolation of lysosomes (N_{cell}), total protein content of lysosomal fraction ($M_{protein}$), isolation yield ($M_{protein}/N_{cell}$), purity, and t_{delay}.

Method	N_{cell} **(million cells)**	$M_{protein}$ **(μg)**	$M_{protein}/N_{cell}$ **(μg/million cells)**	**Purity**	t_{delay} **(min)**
MS	4	32	8.0	High	30
DGC	20	56	2.8	Normal	150

4.3.4. The versability of the magnetic isolation technique using aDxt-MPNPs

To show the versatility of our technique, we performed lysosome isolation experiments using HEK293 cells. The time-dependent colocalization of aDxt-MPNPs with LAMP1 is shown in Figure 4.11A. HEK293 cells were loaded with aDxt-MPNPs for t_{load} = 1 h and subsequently chased in fresh culture medium with t_{chase} ranging from 1 to 12 h. When t_{chase} = 2 h (t = 3 h), the colocalization of aDxt-MPNPs with LAMP1 became clear, as shown in Figure 4.11A. The value of τ_1 for L was derived to be 81 min, which is much shorter than that in the case of COS-1 cells (Figure 4.11B). One of the possible reasons for this result is the smaller cell size of HEK293 compared to COS-1. The cell size in diameter was measured by optical microscopy, and the average cell size was found to be 12.9 ± 1.4 μm for the HEK293 cells, which was significantly smaller than the 20.2 ± 2.4 μm for the COS-1 cells. As a result, t_{chase} for lysosome isolation was determined to be 4 h. The cytotoxicity of aDxt-MPNPs on HEK293 cells was assessed by calcein-AM assay, and no significant cytotoxicity was observed even when the t_{load} was prolonged to 24 h as

shown in Figure 4.12. Photographs of HEK293 cells after incubation with aDxt-MPNPs for t = 12 h (t_{load} = 8 h and t_{chase} = 4 h) (just before homogenization) and the PS fraction (just after magnetic separation) are shown in Figure 4.11C. A Western blot analysis revealed that the purity of the isolated lysosomes was high, as shown in Figure 4.11D. These results clearly confirm the versatility of the technique.

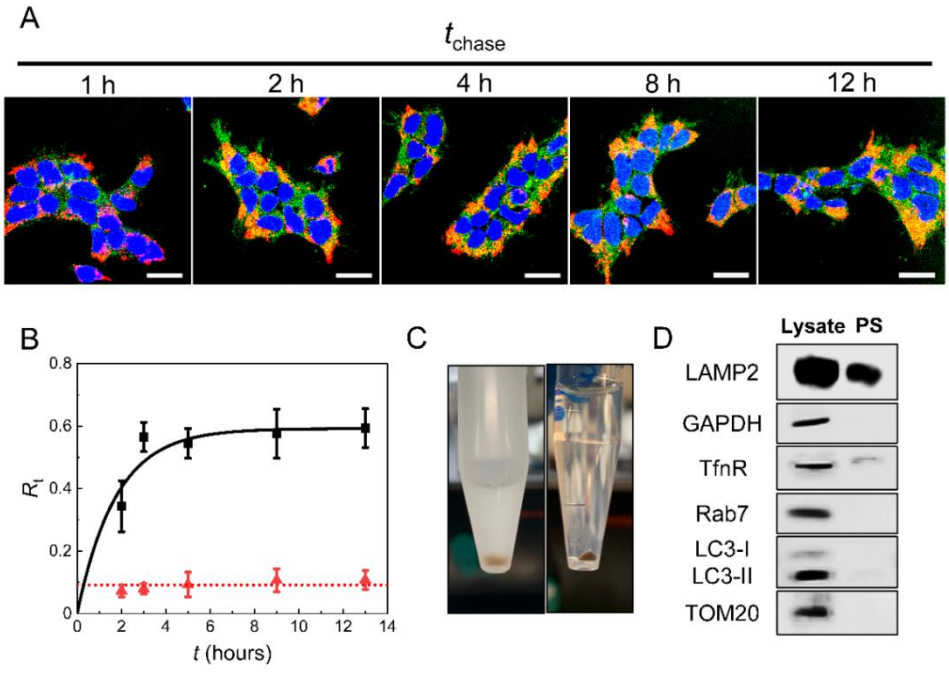

Figure 4.11: Intracellular trafficking of aDxt-MPNPs in HEK293 cells and the result of Western blot analysis for magnetically isolated lysosomes. (A) Confocal laser scanning microscope images showing the colocalization of aDxt-MPNPs with LAMP1 (lysosomal marker protein) over t_{chase} (Nucleus: blue, aDxt-MPNPs: green, Lysosomes: red) (C_{NPs} = 100 µg/mL). Scale bar is 20 µm. (B) Threshold Manders' coefficient (R_t) for aDxt-MPNPs and LAMP1 over time. Red triangles indicate the Rt values calculated between the reconstructed images for aDxt-MPNPs that were generated by randomly shuffling all pixels and the original images for organelle markers; red dashed lines are the average values of the Rt values. (C) Photographs of HEK293 cells after incubation with aDxtMPNPs for t = 12 h (t_{load} = 8 h and t_{chase} = 4 h) (left) and the PS fraction (right). (D) Western blot analysis of the PS fraction and whole cell lysate.

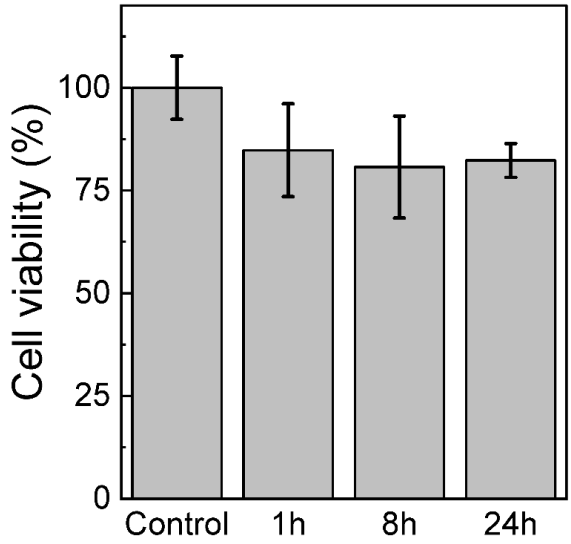

Figure 4.12: The dependence of cell viability on incubation time (t_{load}) for HEK293 cells. Cell viability was measured after incubation in Dulbecco's modified Eagle's medium (DMEM) (+10% FBS) containing aDxt-MPNPs of concentration of 100 μg/mL.

4.4. Conclusion

The approach demonstrated in the present study can be of a great use in studying the functions and the roles of lysosomes in relation to various diseases. First, an important criterion for lysosome isolation is to gently enrich them with high purity for a short time; therefore, the molecules on the membrane or inside lysosomes, such as signaling protein and labile metabolites, can remain unchanged during the enrichment process. In this study, the maximum time required to isolate lysosomes after cell lysis, t_{delay}, was 30 min; this is substantially shorter than that of centrifugation-based techniques, which typically require a minimum separation time of several hours.[8, 9] The isolated lysosome fraction had a high purity, which was confirmed by biochemical analysis. Second, the intact structure of lysosome is crucial for analysis of its composition and function. By employing the

imaging capability of aDxt-MPNPs probe, the integrity of the obtained lysosomes was quickly examined using CLSM imaging. It should be emphasized that the imaging capability of aDxt-MPNPs not only strongly supports the intracellular trafficking study but also provides a shortcut to qualitatively evaluate their integrity in the isolated fraction. Third, the current isolation protocol was demonstrated to be easily adapted with other cell-line and its performance was considerably better than that of density gradient centrifugation technique. Finally, it could be expected that the isolation technique in this study could avoid the loss of protein in lysosomal membrane in comparison with immunoaffinity enrichment of lysosome because the membrane modification are not required.[6] In short, these results demonstrate that the aDxt-MPNPs is a promising multifunctional probe for imaging and rapidly isolating high purified intact lysosomes fraction.

References

1. Aebersold, R.; Mann, M., Mass spectrometry-based proteomics. *Nature* **2003,** *422* (6928), 198-207.

2. Gao, Y.; Chen, Y.; Zhan, S.; Zhang, W.; Xiong, F.; Ge, W., Comprehensive proteome analysis of lysosomes reveals the diverse function of macrophages in immune responses. *Oncotarget* **2017,** *8* (5), 7420-7440.

3. Lim, C.-Y.; Zoncu, R., The lysosome as a command-and-control center for cellular metabolism. *Journal of Cell Biology* **2016,** *214* (6), 653-664.

4. Itzhak, D. N.; Davies, C.; Tyanova, S.; Mishra, A.; Williamson, J.; Antrobus, R.; Cox, J.; Weekes, M. P.; Borner, G. H. H., A Mass Spectrometry-Based Approach for Mapping Protein Subcellular Localization Reveals the Spatial Proteome of Mouse Primary Neurons. *Cell Rep* **2017,** *20* (11), 2706-2718.

5. Itzhak, D. N.; Tyanova, S.; Cox, J.; Borner, G. H., Global, quantitative and dynamic mapping of protein subcellular localization. *Elife* **2016,** *5*.

6. Singh, J.; Kaade, E.; Muntel, J.; Bruderer, R.; Reiter, L.; Thelen, M.; Winter, D., Systematic Comparison of Strategies for the Enrichment of Lysosomes by Data Independent Acquisition. *J Proteome Res* **2020,** *19* (1), 371-381.

7. Miltenyi, S.; Muller, W.; Weichel, W.; Radbruch, A., High gradient magnetic cell separation with MACS. *Cytometry* **1990,** *11* (2), 231-8.

8. Beaumelle, B. D.; Gibson, A.; Hopkins, C. R., Isolation and preliminary characterization of the major membrane boundaries of the endocytic pathway in lymphocytes. *J Cell Biol* **1990,** *111* (5 Pt 1), 1811-23.

9. Aguado, C.; Perez-Jimenez, E.; Lahuerta, M.; Knecht, E., Isolation of Lysosomes from Mammalian Tissues and Cultured Cells. *Methods Mol Biol* **2016,** *1449*, 299-311.

Chapter 5: Summary and Future outlook

5.1. Summary

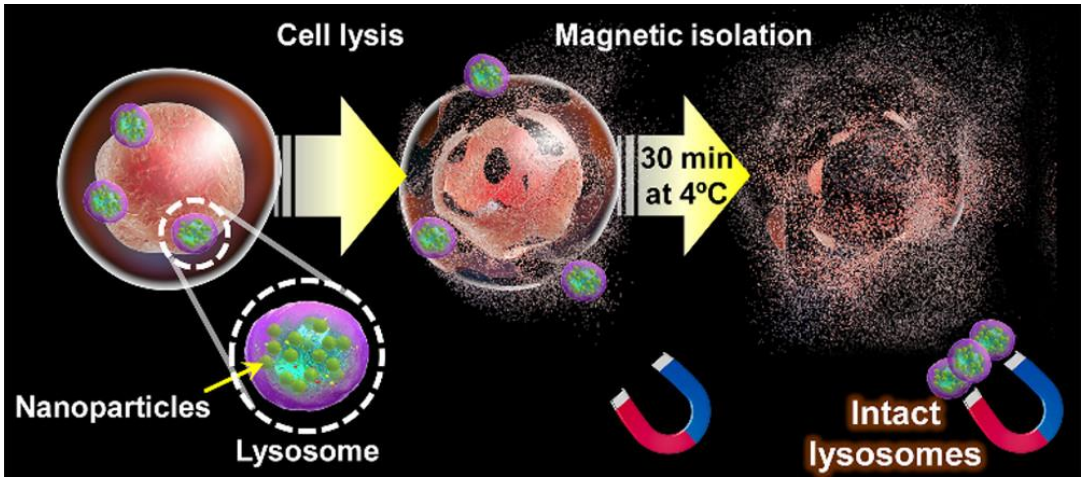

Figure 5.1: The graphical abstract illustrating the main processes of the lysosome isolation using MPNPs.

Lysosome isolation is preresiquite for identifying lysosomal protein composition by mass spectroscopic analysis to reveal lysosome functions and their involvement in some diseases. Magnetic separation is a promising approach to isolating lysosomes from cell lysate with high yield and purity. The aim of this dissertation is to refine the magnetic separation technique by developing an isolation protocol employing multifunctional MPNPs as an alternative for conventional magnetic probes, SPIONs. The achievements of this thesis work are summarized as follows:

In chapter 1, we discussed a brief background of the structure, function, and biogenesis of lysosomes. Since their discovery by Christian de Duve in the 1950s, the role of lysosomes in cellular function has been explored extensively, which led to the change of

the view of lysosomes from a static digestive system to the dynamic regulator of cellular metabolism. As indicated in various studies, lysosomal dysfunctions are found to be linked with the group of metabolic disorders. To present, the global proteomic analysis of lysosomes plays an important role in identify lysosomal functions and the mechanisms of LSDs. Due to the low abundance of lysosomes in cells, the isolation of lysosomes is critical to reduce the complexity of sample to obtain a reliable proteomic dataset. The centrifugation-based methods that have been extensively used to isolate lysosomes often results in low yield and purity. Therefore, developing an alternative method is in great demand. Among the newly developed methods, magnetic separation is swift and quick, which processes excellent features including high yield and purity while efficiently preserving the integrity of lysosomes. Since it is required to magnetize lysosomes before magnetic separation, delivery of magnetic nanoparticles into the lysosomal lumen is one of the attractive approaches. Of note, after internalization, the intracellular trafficking strongly depends on the characteristics of cell-types and physicochemical properties of nanoparticles. The accurate understanding of intracellular trafficking of magnetic nanoparticles is a key step to prevent contamination by other organelles (i.e. endosomes) in the magnetic nanoparticles-based fractionation of lysosomes. Generally, the traditional magnetic probe, SPIONs, requires dye-conjugation to be tracked by fluorescence microscopy. However, it has been suggested that the lysosomal environment could lead to quenching and/or distortion of fluorescence signals of dye, which cause an ensuing effect on the data interpretation. In addition, the surface modification of nanoparticles with dye molecules may influence the nano-bio interactions, which results in the alteration of the cellular uptake and intracellular trafficking of nanoparticles. Herein, to further refine the magnetic nanoparticle-based fractionation, the magnetic-plasmonic

Ag/FeCo/Ag core/shell/shell nanoparticles (MPNPs) are used as multifunctional probes for lysosome isolation. Owing to their plasmonic properties, the intracellular trafficking of MPNPs can be easily investigated using confocal laser scanning microscopy to confirm the accumulation of MPNPs in lysosomes prior to magnetic isolation.

In Chapter 2, we outlined the optimized procedures for preparation of MPNPs using polyol method and hot injection. The TEM size of MPNPs was about 15 nm. To tune hydrophobicity to hydrophilicity, the obtained MPNPs were further encapsulated phospholipid micelles composing of PEG350-DOPE and N-glutaryl DOPE. The encapsulated MPNPs had the average hydrodynamic size of 34 nm and zeta potential of -22 mV. The PEG chains were used enhance colloidal stability, while the carboxylic group of N-glutaryl DOPE was used to further modification. To target lysosomes through the endolysosomal pathway, aDxt molecules were conjugated on the surface of MPNPs using EDC coupling reactions. After aDxt conjugation, the hydrodynamic size of aDxt-MPNPs was about 52.4 nm, while the zeta potential was shifted to positive charge. Importantly, it was showed that aDxt-MPNPs had excellent colloidal stability in the culture medium, DMEM (+10% FBS). Meanwhile, their cytotoxicity was greatly decreased due to the formation of protein corona. The cell viability was approximately 75% for C_{NPs} = 100 μg/mL even after a prolonged t_{load} = 24h. Furthermore, the cellular uptake of aDxt-MPNPs by COS-1 cells was investigated. From ICP-MS analysis, it was estimated that the numbers of aDxt-MPNPs per cell at t_{load} = 1 and 8 h to be 1.1×10^5 and 1.9×10^5, respectively.

Since the aDxt-MPNPs were successfully loaded in cell models, we continued to address an important parameter that was the intracellular trafficking of MPNPs in chapter 3. The result highlighted that aDxt-MPNPs could be monitored using confocal laser

scanning microscope without requiring dye-conjugation owing to their plasmonic property. By using pulse-chase experiments and colocalization study, the time-lapse monitoring of colocalization of with EE, LE and L were determined using Manders' coefficient, R_t. The colocalization results indicated that aDxt-MPNPs arrived early endosomes after t = 2 h, late endosomes after t = 5 h and lysosome after t = 8 h. Furthermore, the time evolutions of R_t were fitted using a stretched-exponential functions. By employing this simple mathematic model, we could derive the characteristic time constants τ_1 and τ_2 for accumulation and decumulation, respectively. τ_1 that represented the speed with which nanoparticles were transported to EE, LE and L, which were derived to be 27, 33, and 250 min, respectively. Importantly, by taking sum of R_t, it was suggested that the aDxt-MPNPs mainly followed the endolysosomal pathway and endosomal escape was almost entirely absent, since the $\sum R_t$ was remained virtually constant after $t \leq 2$ h at above 0.8. Finally, TEM and EDS analysis were used to exam the aDxt-MPNP-treated COS-1 cells after t = 8 h, which confirmed that aDxt-MPNPs were successfully delivered to lysosomes.

After finding appropriate timing to delivery aDxt-MPNPs to lysosomal lumens, chapter 4 showed the results of magnetic isolation of lysosomes. Firstly, the cells were homogenized using 2 ml syringe with 23G needle. Since the efficiency of homogenization could influence the isolation yield, the successful cell homogenization after 15 passages was confirmed using the bright-field microscope. Following this, lysosomes were isolated using MS magnetic column attached to MidiMACS separator. The Western blot confirmed the high purity of the isolated fraction. The integrity of isolated lysosomes was quickly evaluated using CLSM. Importantly, we investigated the effects of temperature and t_{delay} on the potential loss of protein of lysosomes. It was concluded that lysosomes

should be isolated within 30 min after homogenization at 4ºC. Additionally, we compared our established protocol with Lysosome Isolation Kit provided by Abcam, which indicated our magnetic separation method was superior to the density gradient centrifugation method in terms of number of cells required, isolation yield, purity, and t_{delay}. Finally, we applied our protocol to isolated lysosomes from HEK293 cells. Probably due to smaller in size, the time required to delivery aDxt-MPNPs to lysosomes was much shorter than that of COS-1 cells. The lysosomes were also successfully isolated, which confirmed the versatility of the established protocol.

5.2. Future outlook

This thesis work has proposed a robust nanoparticle-based magnetic isolation for intact lysosomes. This method could be important to study the lysosomal proteome dynamics to reveal lysosomal functions in different context or their involvement to LSDs. Additionally, owing to excellent optical properties, MPNPs are expected to be applicable to live-cell imaging to investigate the intracellular transport dynamics of nanoparticles in some cell-lines with LSDs, in which the trafficking defects are existed.

In this study, although MPNPs have been presented as a promising alternative for traditional SPIONs, their possible biological effects should be further investigated. A question is that whether or not the accumulation MPNPs in lysosomal lumen affect the lysosomal activity, which may influence proteomic analysis. Additionally, this study suggested that there exist possible protein composition changes in the isolated fractions during isolation via amino acid compositions, the further investigation should be conducted to determine which proteins such as lysosomal proteins or lysosome-related proteins are degraded.

In chapter 3, it was observed that only a fraction of lysosomes was isolated from cell samples, many lysosomes were still remains in negative selection. Since the property of lysosomes are heterogeneity, therefore, it is not clear that if the obtained fraction may only represent for a specific subpopulation of lysosomes. And if it is true, whether the different type of separation approaches would affect the subpopulation of isolated lysosomes. Probably, the further studies are still needed to further address these questions.

Achievement List

Publication

1. **T. S. Le**, M. Takahashi, S. Maenosono, A robust nanoparticle-based magnetic separation method for intact lysosome, *Bio-protocol* **2022**, 12, e4453.
2. **T. S. Le**, M. Takahashi, N. Isozumi, A. Miyazato, Y. Hiratsuka, K. Matsumura, T. Taguchi, S. Maenosono, Quick and Mild Isolation of Intact Lysosomes using Magnetic- Plasmonic Hybrid Nanoparticles, *ACS Nano* **2022,** 16, 885-896.
3. **T. S. Le.**, S. He, M. Takahashi, Y. Enomoto, Y. Matsumura, S. Maenosono, Enhancing the Sensitivity of Lateral Flow Immunoassay by Magnetic Enrichment Using Multifunctional Nanocomposite Probes, *Langmuir* **2021**, 37, 6566–6577.

Conference presentation

1. **T. S. Le,** M. Takahashi, Y. Hiratsuka, K. Matsumura, T. Taguchi, and S. Maenosono, "Quick and Mild Isolation of Intact Lysosomes using Magnetic-Plasmonic Hybrid Nanoparticles", Materials Research Meeting 2021 (MRM2021), 13-17 December 2021, Pacifico Yokohama, Kanagawa, Japan (Hybrid).
2. **T. S. Le,** M. Takahashi, Y. Hiratsuka, K. Matsumura, T. Taguchi, and S. Maenosono. "Intracellular Trafficking Study and Rapid Purification of Lysosomes Using Magnetic Plasmonic Nanoparticles", The 2021 MRS Fall Meeting, 28 November – 3 December 2021, Boston, USA (Hybrid).
3. **T. S. Le,** M. Takahashi, Y. Hiratsuka, K. Matsumura, T. Taguchi, and S. Maenosono, "Magnetic Isolation of Intact Lysosomes using Magnetic-Plasmonic Hybrid Nanoparticles with Understanding of Their Cellular Trafficking", SCEJ 52nd Autumn Meeting, 22-24 September 2021, online.
4. **T. S. Le,** S. He, M. Takahashi, Y. Enomoto, Y. Matsumura, and S. Maenosono, "Enhancing the Sensitivity of Lateral Flow Immunoassay by Magnetic Enrichment Using Nanocomposite Probes", SCEJ 52nd Autumn Meeting, 22-24 September 2021, online.
5. **T. S. Le,** M. Takahashi, Y. Hiratsuka, K. Matsumura, T. Taguchi, and S. Maenosono, "Magnetic Isolation of Intact Lysosomes using Magnetic-Plasmonic Hybrid Nanoparticles with Understanding of Their Cellular Trafficking", The 72nd

Divisional meeting of division of colloid and surface chemistry, 15-17 September 2021, online.

6. **T. S. Le,** S. He, M. Takahashi, Y. Enomoto, Y. Matsumura, and S. Maenosono, "Sensitivity Enhancement of Lateral Flow Immunoassay through Magnetic Enrichment using Multifunctional Nanocomposite Probes", The 72nd Divisional meeting of division of colloid and surface chemistry, 15-17 September 2021, online.
7. **T. S. Le,** S. He, M. Takahashi, Y. Enomoto, Y. Matsumura, and S. Maenosono, "Enhancing the Sensitivity of Lateral Flow Immunoassay by Magnetic Enrichment Using Multifunctional Nanocomposite Probes", INTERFINISH2020, 6-8 September 2021, online.
8. **T. S. Le,** M. Takahashi, Y. Hiratsuka, K. Matsumura, T. Taguchi, and S. Maenosono, "Lysosome-Targeting Magnetic-Plasmonic Hybrid Nanoparticles for the Imaging and Isolation of Intact Lysosomes", The 101st CSJ annual meeting, 19-22 March 2021, online.

Acknowledgement

This thesis would not have been possible without the help, support, and guidance of many people.

Firstly, I would like to express my deep gratitude to my advisor, Prof. Shinya Maenosono for his guidance, incisive comments, constructive criticism, and encouragement during my phD course to train me become an independent researcher. I also feel grateful that he granted me the chance to work with various research topics and gave me the trust in the projects I involved. In addition, his patience and professional instructions helped me a lot in all the time of research and writing of manuscripts as well as this thesis. Furthermore, I really appreciate his understanding and empathy for my personal difficulties during my phD course.

I would like to express my special thanks to Prof. Taguchi Tomohiko from Tohoku University for his insightful comments and concrete suggestions for my phD project. Without his supervision, the completion of my thesis work would not have been possible.

I would like to express my heartfelt appreciation to my second advisor, Prof. Kazuaki Matsumura, who have provided me a lot of support and resources for my biological experiments. Also, he gave me many valuable advice to deal with the problems I faced during performing cell experiments.

I am profoundly grateful to my minor research supervisor, Assoc. Prof. Yuichi Hiratsuka, who not only supervised me to complete an interesting minor research project but also provided me a lot of resources and advice to complete my main theme research. Personally, I really enjoyed the minor research topic with him and his class about artificial muscles.

I would like to thank Assit. Prof. Mari Takahashi for training me the basic of biological experiments since this was a completely new research topic for me. In addition, many thanks to have many interesting conservations and discussion with me in both science and daily life.

I would like to thank Dr. Isozumi Noriyoshi and Dr. Akio Miyazato for the support to measure High-performance liquid chromatography of my lysosome samples. I would like to thank Ms. Keiko Kawamoto of Japan Advanced Institute of Science and Technology (JAIST) for her assistance in cell experiments. I am grateful to Assit. Prof. Shigetaka Nakamura and Prof. Kenzo Fujimoto of JAIST for their support in performing chemiluminescence detection of Western blots.

I also show my heartiest thanks to all members in Maenosono lab for a lot of help and support as well as the fun activities during studying at JAIST, which includes former students, Mr. Kimihiro Numano, Mr. Masahito Hatsukano, Ms. Hesizun, Ms. Dwivedi Pratibha, Mr. Shujie Fei, Mr. Congkang Hu, Mr. Junpeng Liu, and current students, Mr. Daisuke Maemura, Mr. Yuki Kitazaki, Mr. Simon David, Mr. Keiji Kobayashi and Ms. Fukue Kotegawa.

I would like to thank Dr. Tran Viet Thu for recommending me to Maenosono Lab. I would also like to thank Mr. Le Dinh Son in Nishimura lab for many helps and support, as well as all of the Vietnamese students at JAIST for arranging events at some special occasions and sport activities.

I would like to thank the Ministry of Education, Cultures, Sports, Science and Technology of Japan for their phD scholarship.

Last but not least, I deeply thank my family for their incredible support and understanding. Most importantly, thank you to my wife who take care of my family and always stand by me during the hard time of my phD at JAIST. Finally, to my father in heaven who never saw this adventure, this work is dedicated to you.

The Son Le
Japan Advanced Institute of Science and Technology
May 2022